LASER FREQUENCY COMBS FOR PRECISION ASTRONOMICAL SPECTROSCOPY

by

GABRIEL GEORGE YCAS

B.A., Reed College, 2005

A thesis submitted to the

Faculty of the Graduate School of the

University of Colorado in partial fulfillment

of the requirement for the degree of

Doctor of Philosophy

Department of Physics

2013

This thesis entitled:

Laser Frequency Combs for Precision Astronomical Spectroscopy

written by Gabriel George Ycas

has been approved for the Department of Physics

_____

Dr. Scott Diddams

_____

Prof. Alysia Marino

*Date*_____

The final copy of this thesis has been examined by the signatories, and we

Find that both the content and the form meet acceptable presentation standards

Of scholarly work in the above mentioned discipline.

Ycas, Gabriel George (Ph.D., Physics)

Laser Frequency Combs for Precision Astronomical Spectroscopy

Thesis directed by Dr. Scott Diddams

Laser frequency comb sources promise to enable precision astronomical spectroscopy at the 10^{-11} level, enabling observations aimed at locating potentially habitable planets. Frequency combs allow for the simultaneous generation of thousands of individual laser lines, each with optical frequency referenced to the SI second, and are capable of providing a bright, simple, and stable spectrum ideal for the calibration of grating-based astronomical spectrographs. In order for frequency combs and spectrographs to be used in tandem, key technical challenges must be addressed. Most critically, it is necessary to increase the mode-spacing of the frequency comb to more than 20 GHz while simultaneously retaining the stability and broad optical bandwidth of the comb.

This thesis also offers an overview of modern astronomical spectroscopy, along with a thorough discussion of the technical details of mode-locked lasers and frequency comb design. This thesis begins by presenting a frequency comb system with mode-spacing of 25 GHz suitable for the near-infrared between 1500 and 1700 nm. Examples are shown from the successful calibration of the Penn State University Pathfinder astronomical spectrograph located at the Hobby-Eberly telescope using the frequency comb system. In the second half of the thesis, the erbium-fiber frequency comb is shown to generate highly coherent, ultrafast, and bright pulses at 1050 nm. The short duration and high peak power of these pulses enable coherent and continuous extension of the comb to visible wavelengths. Next, an accurate model of a nonlinear fiber optic amplifiers is developed and tested, then applied to optimize the selection of fiber lengths in the design of ultrafast

nonlinear fiber-optic systems. Finally, a broad-bandwidth optical filter cavity for the generation of a 980—1110 nm suitable for calibration of next-generation spectrographs was designed and tested.

ACKNOWLEDGEMENTS

First and foremost, I would like to thank my advisor Scott Diddams for his enthusiasm and unwavering support. I would also like to thank Steve Osterman from CU Boulder's Center for Astrophysics and Space Astronomy for his role in launching the project and his contributions to the practical aspects of conducting the astronomical observations made in this thesis.

I would also like to thank Frank Quinlan, who kindly provided my first lessons on fiber optics and whose careful characterization of the frequency comb system provided a jumping off point for my work. I am grateful to Florian Adler for the construction of the FROG apparatus and to Stephanie Meyer for the construction of the near-IR f—2f interferometer and grating compressor. I would also like to thank Gillian Nave for her very patient assistance in measuring the frequency comb with the NIST Fourier Transform Spectrograph.

In addition to Steve Osterman, a number of undergraduate researchers worked very hard to let us bring the frequency comb to the telescope environment. I would like to thank Eitan Cher and Lionel Wynn for the construction of an acoustic isolation box for the frequency comb as well as Chelsea Donaldson for her efforts in characterizing and mitigating modal noise.

From Penn State University, I would like to thank Suvrath Mahadevan and his astronomical spectroscopy team, especially Chad Bender, Steven Redman, Ryan Terrien, and Brandon Botzer, as well as Larry Ramsey. Their excitement in the use of frequency combs for astronomy, patience explaining the finer points of precision astronomical spectroscopy, and expertise in using the comb as a calibration source were essential.

From my past, I would like to thank Eric Wollman of the Bates College Physics department for providing me with a stimulating and enjoyable three years in Lewiston, Maine. I am also very grateful to Lily Childress for her enthusiastic support and for connecting me with Scott.

Finally, I would like to thank my parents, grandparents, brothers, and my partner Stephanie for their support and inspiration throughout my life.

TABLE OF CONTENTS

TABLE OF TABLES

TABLE OF FIGURES

Chapter 1

INTRODUCTION

The origin of spectroscopy can be traced to Newton, who, in 1664, used prisms to split white light into its component colors and then recombine them. In doing so, Newton provided the term "spectrum" to describe the dispersed colors of the sun. More than 100 years later the German glassmaker and physicist Joseph von Fraunhofer repeated Newton's observations using a sophisticated spectrograph consisting of an entrance slit, a prism, and an achromatic telescope. In these observations, Fraunhofer discovered hundreds of absorption lines in the solar spectrum, and then went on to measure the spectra of celestial bodies, including Mars, Venus, Sirius, and Betelgeuse. In these pioneering observations, Fraunhofer noted that the planets have spectra similar to the Sun, but that significant differences existed between the spectra of the sun and Sirius – for example, both Sirius and the sun possess the D (sodium) and b (iron and magnesium) lines, while other lines are present only in the Sun. Shortly after Fraunhofer's discovery of absorption lines, Gustav Kirchhoff and Robert Bunsen identified emission lines as characteristic of chemical compounds, and Kirchhoff demonstrated that the dark lines in absorption spectra are caused by absorption of continuum light by a cool gas [55].

The next significant step in the development of spectroscopy as an astrophysical tool was the prediction by Christian Doppler in 1842 of a velocity-induced shift in the wavelength of a moving star, and the comment by Hippolyte Fizeau that the same shift should be observable in absorption lines in a moving star. Observing this shift requires not just resolution, but also precision calibration. In 1868, Sir William Huggins sought to observe the velocity-induced shift in stellar absorption lines. Using a telescope, a prism spectroscope, and a discharge lamp, Huggins searched for a Doppler-Fizeau shift in the hydrogen F (Hβ) line in various stars. By simultaneously observing the star and the discharge lamp, Huggins qualitatively reported a radial-velocity shift

in the spectrum of Sirius [38], noting that "the narrow line of hydrogen, though it appeared projected upon the dark line in Sirius, did not coincide with the middle of the line, but crossed it at a distance from the middle." Though it was imprecise, this observation heralded the age of precision astronomical spectroscopy. In the following decades, more refined spectroscopic measurements led to the discovery of "spectroscopic binary" star systems, the speeds of solar flares, and the presence of stationary telluric absorption features in Earth's atmosphere. Following these successes, the cataloging of stellar radial velocities began in earnest, culminating in 1929 with Edwin Hubble's observation that Cepheid variables, a type of standard candle star, not only have velocity away from the Earth, but also have velocities that depend linearly upon their distance [37]. The implication of an inflating Universe was immediately understood, and the field of observational cosmology was born.

In many ways, modern precision astronomical spectroscopy is a direct refinement of these early measurements. In the 20th and 21st centuries, advances have been made in the sensitivity and precision of spectrographs. Increased sensitivity allows for the detection of fainter objects from the earlier Universe, while improvement in measurement precision, both from gains in spectrograph stability and also calibration precision, allow for the detection of ever more subtle spectral shifts. The current generation of observations, which include physical, cosmological, and planet-finding, each push the limits of sensitivity and precision.

Science goals of Precision Astronomical Spectroscopy

Cosmology

Rate of change of inflation of the Universe

Since Hubble's discovery of the expansion of the Universe in the 1920s, cosmology has sought to answer the question of the Universe's ultimate fate. Recent measurements of Type 1a supernovae [74, 65] have answered this question, pointing to a forever expanding universe. This answer has raised a new question,

however. Gravitational attraction tends to deflate the Universe, and continued expansion requires the presence of some form of "dark energy" to exert negative pressure upon "empty" space. The nature of this dark energy remains unexplained, and new experiments to probe the dynamics of the Universe are hoped to better characterize its physical effects. The upcoming CODEX spectrograph, for example, will be installed on the 39-meter European Extremely Large Telescope. Its primary goal is to directly measure the rate of change of the expansion of the Universe. By measuring Lyman-α lines in light from quasi-stellar objects at unprecedented precision (parts in 10^{-10}) [64] over the span of several decades, it is hoped that the rate of change of expansion can be directly measured at levels 100 times more precise than presently achievable.

Variation of Physical Constants

The relativistic correction to the energy splitting of an atomic multiplet depends upon the fine structure constant α. At some redshift *z*, corresponding to a portion of the Universe so far away that the inflation of spacetime has lengthened the wavelength of light by a factor of $(1+z)^{-1}$, the magnitude of the multiplet splitting is given by the expression

$$E_z = E_{z=0} + \left[Q_1 + K_1(\mathbf{LS})\right] Z^2 \left[\left(\frac{\alpha_z}{\alpha_0}\right)^2 - 1\right] + K_2\left(\mathbf{LS}\right)^2 Z^4 \left[\left(\frac{\alpha_z}{\alpha_0}\right)^4 - 1\right], \tag{1.1}$$

where $E_{z=0}$ is the energy splitting in the laboratory, *Z* is the nuclear charge, α_0 is the zero redshift value, α_z is the value of the fine structure constant at some redshift *z,* $\mathbf{L}$ and $\mathbf{S}$ are the electron total orbital angular momentum and total spin [25, 94]. The constant Q_1 describes a relativistic correction for a given change in α, while the constants K_1 and K_2 are the relativistic spin-orbit coefficients.

The fact that the magnitude of the α_z / α_0 -dependent shift depends upon Z^2 allows for a calibrated astronomical measurement. Iron (Z=26) and magnesium (Z=12) are common in the Universe, and by measuring the relative wavelength shift between the sensitive Fe II and the insensitive Mg II lines, a long

lever-arm is created allowing for sensitive detection of fine-structure constant variations. Using this scheme, a fractional change $\Delta\alpha / \alpha = 10^{-5}$ can be detected by measuring a change in the frequency interval between Fe and Mg transitions of 0.03 cm^{-1}, fractionally 10^{-6}. While initial measurements achieved a null result [94], a more recent survey has discovered a dipole variation in α with magnitude $\Delta\alpha / \alpha \approx 10^{-5}$ [93]. While the statistical confidence in this value is very high (4.2σ), it was obtained from only 12 observational targets and it is a goal of next-generation spectrographs to follow-up on the extraordinary indication of a dipole moment in one of the physical constants.

The search for exosolar plants

The Doppler radial-velocity technique is a scheme for using spectroscopic techniques to detect extrasolar planets. In the simple example of a stellar system with a star and single planet, the two bodies orbit around their common center of mass. The presence of the planet thus induces a periodic motion in the star, which causes the starlight to be periodically Doppler shifted and is a clear signal of the presence of the unseen planet. The discovery of the first extrasolar planet occurred in 1995 [54] with a Doppler velocity precision of 15 m s^{-1}, heralding the exoplanet era. In the time since, 927 extrasolar planets have been located. Of these planets, 531 were detected by the radial-velocity technique. With spectroscopic precision at the cm s^{-1} (fractionally 1 in 10^{10}) level, it will be possible to detect habitable Earth-like planets.

Laser Frequency Combs

From Huggins' first measurement of the Doppler shift, it has been clear that such measurements are limited by the accuracy to which a spectrograph can be calibrated. As modern observational goals require short-term calibration precision and stability over timescales of decades, it has become clear that a new type of

calibration standard is required. Laser frequency combs are in many ways perfectly suited to meet these demands [63, 83].

A laser frequency comb is most easily described not by how it works, but by what it produces. The first distinguishing feature of a laser frequency comb is its output, which is not a single "laser line" but thousands or millions of laser lines that span tens or hundreds of nanometers of optical bandwidth. The second feature of a laser frequency comb is that the spacing between each of the thousands of "comb modes" is precisely the same. As a result, the frequency of any one of the modes comprising the laser frequency comb is described by the simple equation

$$f_n = n \times f_{\mathrm{rep}} + f_{\mathrm{CEO}}, \tag{1.2}$$

where f_{rep} is the spacing between the comb modes, n is the index of the comb mode, and f_{CEO} is a constant, experimentally measured frequency. The power of the frequency comb comes from fact that the comb's two degrees of freedom, f_{rep} and f_{CEO}, are in the radio domain, while the individual comb modes are optical frequencies. These two frequencies can be measured and even controlled, and as a consequence the laser frequency comb provides a direct link between two radio frequencies and the optical frequencies of thousands of laser lines.

Historically, the development of laser frequency combs was simultaneously long in the making and astonishingly rapid. Two key technologies are required for the generation of frequency combs: mode-locked lasers, which provide the comb modes, and novel nonlinear fibers, which permit detection of the offset frequency f_{CEO}. Mode-locked lasers have been developed actively since the 1960s [80], and in the early 1990s mode-locked lasers were developed that are capable of producing the sub-100 femtosecond pulses needed for generating coherent frequency combs [81, 85]. These lasers were developed for applications in communications, where short optical pulses were important, and the time-bandwidth product was quickly reached.

In the late 1990s, a breakthrough moment occurred when J. Ranka, working at Bell Labs, presented a visible white-light supercontinuum from a "photonic crystal fiber" (PCF) at the 1999 CLEO conference [72, 71]. The Hall and Cundiff groups at JILA, seeing tremendous advantages in frequency metrology in a stabilized mode-locked laser "frequency comb," set off in a race to create a self-referenced laser frequency comb. Only months after the unveiling of the PCF, a mode-locked Ti:sapphire laser was fully frequency stabilized [39].

While frequency combs have the required precision and absolute accuracy for astrophysical spectrogram calibration, mode-locked lasers produce combs which are "too dense," with modes so closely spaced that many modes lie within each spectrograph resolution bin. Because the resolution of astrophysical spectrographs is determined by the absorption features that they resolve, the resolution must be treated as fixed – only by increasing the comb mode-spacing can frequency combs be made to into suitable calibrators. The spacing of the modes of a laser frequency comb is inversely proportional to the amount of time taken for a pulse to circulate the optical cavity. The degree to which the physical size of a mode-locked laser cavity can be shrunk is thus a fundamental constraint on the maximum possible mode-spacing. While bulk-optic lasers with mode-spacings of up to 10 GHz have been demonstrated in research laboratories [5], the maximum mode-spacing that has been achieved for a highly-stable mode-locked fiber laser suitable for use in the setting of an astronomical observational campaign is 490 MHz [50], while the highest repetition rate commercially available mode-locked fiber laser has a repetition rate of 250 MHz [97]. Because the native mode-spacing of laser frequency combs must be treated as fixed, attention has turned to development of Fabry-Perot filter cavities [79, 83, 11] to passively increase the mode-spacing of standard mode-locked erbium-fiber [67, 100], ytterbium-fiber [98, 99], and titanium sapphire laser frequency combs [48, 8].

Thesis Outline

This thesis describes efforts to develop and deploy a laser frequency comb calibrator based upon an erbium-doped mode-locked laser. The calibrator described here is specifically designed for assisting in planet-finding observations, and the second chapter provides a more detailed introduction to both the Doppler radial-velocity technique and also to the calibration schemes used in modern astronomical spectroscopy.

The third chapter describes the details of the erbium fiber comb, providing both a description of the mode-locking physics and also the practical details of frequency stabilizing the frequency comb. This chapter also contains a derivation of Fabry-Perot cavity resonances, the relationship between the resonance spacing and dispersion, and details about the physical construction of Fabry-Perot cavities for filtering the laser frequency comb.

In the fourth chapter, the measurement techniques used throughout the thesis are described, including optical heterodyne measurements and frequency-resolved optical gating. When relevant, the noise limits of these techniques are also presented. Chapter (five) presents the first major result of this thesis, the first-ever use of a 25 GHz erbium laser frequency comb for the calibration of on-sky stellar spectra. In addition to the on-sky results, details of the calibration system, measurements of its performance, and limitations are discussed.

Chapters 6, 7, and 8 comprise the second part of the thesis, and are devoted to the development of a near-infrared (800--1350 nm) frequency comb calibrator. Chapter 6 discusses the results of an initial experiment in using nonlinear optics to continuously extend the 1550 nm erbium laser into the visible, demonstrating for the first time the coherence of a multi-octave spanning erbium fiber-laser frequency comb. This chapter also details a second-generation amplifier constructed using polarization-maintaining fibers. Chapter 7 uses numerical models of fiber optic amplifiers and nonlinear optics to provide a physical explanation of the measurements made in the previous chapter, and will hopefully be of use in the development of future

fiber-optic systems. Chapter 8 is devoted to the development of a broad-band filter cavity, including the detailed characterization of custom-built low-dispersion mirrors. Chapter 9 concludes with a summary of the results obtained during this thesis project, as well as an outlook into the near future of both the CU/NIST calibrator and the future of laser frequency comb calibration for astrophysical spectrographs.

Chapter 2

SPECTROSCOPIC PLANET-FINDING

While cosmological measurements are of great interest to modern cosmology, the work in this thesis concerns the search for potentially habitable planets orbiting nearby stars. This search is an ideal starting point for laser frequency comb-calibrated spectroscopy for several reasons. Firstly, the hardware requirements are vastly more relaxed than cosmological measurements – instead of the $1.4-billion European Extremely Large Telescope (E-ELT), planet-finding can be conducted using much smaller instruments –in our case, the $13-million Hobby-Eberly telescope. Secondly, the precision required for planet-finding is orders of magnitude lower than that needed for cosmological measurements. Whereas useful cosmology can only occur with long-term precision of parts in 10^{11}, it is possible that a habitable planet could be found with precision of a few parts in 10^{8}. The relatively low risk afforded by smaller telescopes and the more relaxed requirements for precision are well suited to the first generation of frequency comb-based calibrators.

The Doppler Radial-Velocity Technique

It is useful to present the basic classical mechanics which describe the effect of a planet on a star [52, 30]. A well-known result of classical mechanics is the solution of the Keplerian two-body problem, which can be reduced to a description of the motion of a point particle under the action of a central force. The solution for the particle's location *r* as a function of the orbital parameter θ is

$$r = \frac{a\left(1-\varepsilon^2\right)}{\left(1+\varepsilon\cos\theta\right)}, \tag{2.1}$$

where ε is the orbital eccentricity and a is the semi-major orbit. The parameter θ is in fact the relative angle of the body with respect to the semi-major axis, and in Cartesian coordinates its position is

$$\mathbf{r} = \begin{pmatrix} r\cos\theta \\ r\sin\theta \end{pmatrix}, \tag{2.2}$$

and a time derivative gives the velocity,

$$\dot{\mathbf{r}} = \begin{pmatrix} \dot{r}\cos\theta - r\,\dot{\theta}\sin\theta \\ \dot{r}\sin\theta + r\,\dot{\theta}\cos\theta \end{pmatrix}. \tag{2.3}$$

We seek a description of the radial velocity $\dot{\mathbf{r}}$ as a function only of θ, and so Eq. (2.1) and its derivative

$$\begin{aligned} \dot{r} &= \frac{a\left(1-\varepsilon^2\right)}{\left(1+\varepsilon\cos\theta\right)^2}\varepsilon\sin\theta\dot{\theta} \\ &= \frac{r^2}{a\left(1-\varepsilon^2\right)}\varepsilon\sin\theta\dot{\theta} \end{aligned} \tag{2.4}$$

can be used along with the conservation of angular momentum l,

$$mr^2 d\theta = l\,dt, \tag{2.5}$$

to simplify Eq. (2.3) to

$$\dot{\mathbf{r}} = \frac{l}{m}\frac{1}{a\left(1-\varepsilon^2\right)}\begin{pmatrix} -\sin\theta \\ \varepsilon+\cos\theta \end{pmatrix}. \tag{2.6}$$

The total angular momentum in the case of an elliptical orbit is

$$l = \sqrt{mak\left(1-\varepsilon^2\right)}. \tag{2.7}$$

Finally, to change from reduced coordinates and find the motion of just one of the bodies, both the angular momentum and position l_1, a_1 are scaled by the factor $m_2 \,/\, \left(m_1 + m_2\right)$ and the Newton's law of universal gravitation is applied for the force k. Substituting into Eq. (2.6) gives the expression for the star's velocity,

(2.8) $$\dot{\mathbf{r}}(\theta) = \sqrt{\frac{G m_2^2}{m_1 + m_2} \frac{1}{a\left(1-\varepsilon^2\right)}} \begin{pmatrix} -\sin\theta \\ \varepsilon + \cos\theta \end{pmatrix}.$$

When projected along the line of sight with angle i between the orbital axis and the Earth, the amplitude of the maximum radial velocity *K* of the star is

(2.9) $$K = \sqrt{\frac{G}{a\left(1-\varepsilon^2\right)}} \frac{m_{\text{planet}} \sin i}{\sqrt{m_{\text{star}} + m_{\text{planet}}}}.$$

Recalling special relativity, the Doppler shift of light by a moving body is

(2.10) $$\lambda = \lambda_0 \frac{1 + \mathbf{k} \cdot \mathbf{v} \,/\, c}{\sqrt{1 + v^2 \,/\, c^2}},$$

where $\mathbf{k}$ is the unit vector between the two bodies, $\mathbf{v}$ is the relative motion between them, and λ_0 is the wavelength of light as measured in the rest frame of the emitting body. For velocities much smaller than the speed of light, the magnitude of the wavelength shift is

(2.11) $$\frac{\delta\lambda}{\lambda} \approx \sqrt{\frac{G}{a\,c^2\left(1-\varepsilon^2\right)}} \frac{m_{\text{planet}}}{\sqrt{m_{\text{star}} + m_{\text{planet}}}} \sin i \cos i.$$

By measuring the wavelength shift over the course of the planet's orbit around the star, the radial velocity semi-amplitude *K*, the orbital eccentricity ε, and the orbital period can be determined. Other measurements (spectroscopy, photometry, astroseismometry, and parallax measurements) can be used to determine the stellar mass, from this the minimum planetary mass $m \sin i$ can be determined. In our own solar system, the fractional wavelength in the Sun's light induced by the Earth is fractionally 3×10^{-10} or 9 cm s^{-1}, while the presence of Jupiter leads to a fractional shift of 4×10^{-8}, or 12 m s^{-1}.

It is worth noting the capacity of Doppler measurements to provide confirmation of, and information about, planets detected using other means. Perhaps most significant are photometric planet searches, such as the NASA/JPL Kepler mission, which detect planets by measuring the dip in stellar intensity as a planet passes

directly in the line of sight between Earth and the host star. When a spacecraft and large detector are used, a huge number of stars can be simultaneously observed; the Kepler spacecraft has detected hundreds of planets and identified thousands more potential detections candidates. . In some cases, especially for small planets, the light curve may be noisy and the presence of a planet may be questionable. Follow-up observations using the radial-velocity technique can be used to not only confirm the presence of the planet, but also to fully characterize it: while the radial-velocity measurement provides the orbital parameters and planetary mass, the photometric observation provides the relative size of the planet relative to the star. By combining these data, the size, mass, and orbital parameters of the planet can be determined.

Calibration of Astrophysical Spectrographs

To measure the Doppler shift induced by an orbiting planet, it is of course necessary to calibrate a spectrograph at a precision at least as high as the size of the shift being sought. Conventional calibrators use elemental or molecular transitions to either impose absorption features upon stellar spectra or to simultaneously illuminate a spectrograph with star and calibration light. The stability of the calibration source, the quality of its features, and the mechanical stability of the spectrograph determine the precision to which a spectrograph can be calibrated. It is important to note here that astrophysical observations are typically not absolute, but merely precise. Because spectrographs measure the dispersed spectrum of light, even minute variations in the direction of propagation of the input beam into the spectrograph lead to large static shifts in wavelength. Provided that these shifts are static – that the spectrograph itself is stable—the fact that the calibration is merely precise over the orbital period of the planet being observed is sufficient. The following section will describe the different types of calibration standards and techniques.

Absorption Cell Techniques

The use of absorption cells as wavelength reference sources for astrophysical measurements was pioneered in 1979 by G. Walker and B. Campell. With a cell containing hydrogen fluoride (HF) inserted into the light path of the Canada France Hawaii Telescope, they monitored 21 stars over 12 years with 15 m s^{-1} accuracy. To achieve sufficient absorption, the HF cells were 90 cm in length, and the reference lines were the ~ 10 lines spanning 15 nm which comprise the R branch of the 3-0 molecular vibration rotation band. Although no planets were found due to the small or simply unlucky choice of targets, the successful use of an absorption cell led to the development of the iodine cell technique by Marcy and Butler in 1992 [53]. Unlike hydrogen fluoride, molecular iodine has a dense forest of absorption features over the 500—630 nm wavelength range which are strong enough that only a 5 cm cell is required [45].

Conceptually, the absorption cell technique is very simple, and is sketched in Figure 1. In order to calibrate the wavelengths of starlight being collected, a cell containing a gas with a known absorption spectrum (eg HF or I_2) is placed between the telescope and spectrometer. The experimentally-known absorption spectrum thus modulates the stellar spectrum, and the imposed structure provides a calibration. Mathematically, the shift of the stellar spectrum λ_s is determined [53] by inverting the expression

$$I_{\rm obs}(\lambda) = \left[I_{\rm s}(\lambda + \Delta\lambda_{\rm s}) T_{\rm cell}(\lambda + \lambda_{\rm cell}) \right] \otimes \mathrm{PSF}, \tag{2.12}$$

where $I_{\rm obs}$ is the stellar spectrum observed with the iodine cell in place, $I_{\rm s}$ is the "template" stellar spectrum observed without the absorption cell in place, $T_{\rm cell}$ is the transmission spectrum of the cell as measured in a laboratory, PSF is the spectrograph's point spread function, and $\otimes$ is the convolution. The parameter $\Delta\lambda_s$ is the shift in wavelength of the stellar spectrum, while $\Delta\lambda_{\rm cell}$ is the shift of the iodine transmission. Because the iodine absorption signal is imposed upon the stellar spectrum, the accurate determination of $\Delta\lambda_{\rm cell}$ accounts

for all instrumental shifts. With the instrumental systematic removed, the $\Delta\lambda_s$ represents the Doppler radial velocity signal. Using this technique, radial velocities with uncertainties below 3 m s^{-1} have been consistently reported, with examples including a radial velocity scatter of 2.9 m s^{-1} for HD109358) [45] and 1.2 m s^{-1} for HD179079 [90]. By measuring a very bright target thousands of times, and by throwing away outlier measurements, a value of 1.9 cm s^{-1} was reported for α Centauri A [12]. In the near-infrared, a gas cell containing ammonia has been used to provide 3 m s^{-1} calibration precision [7].

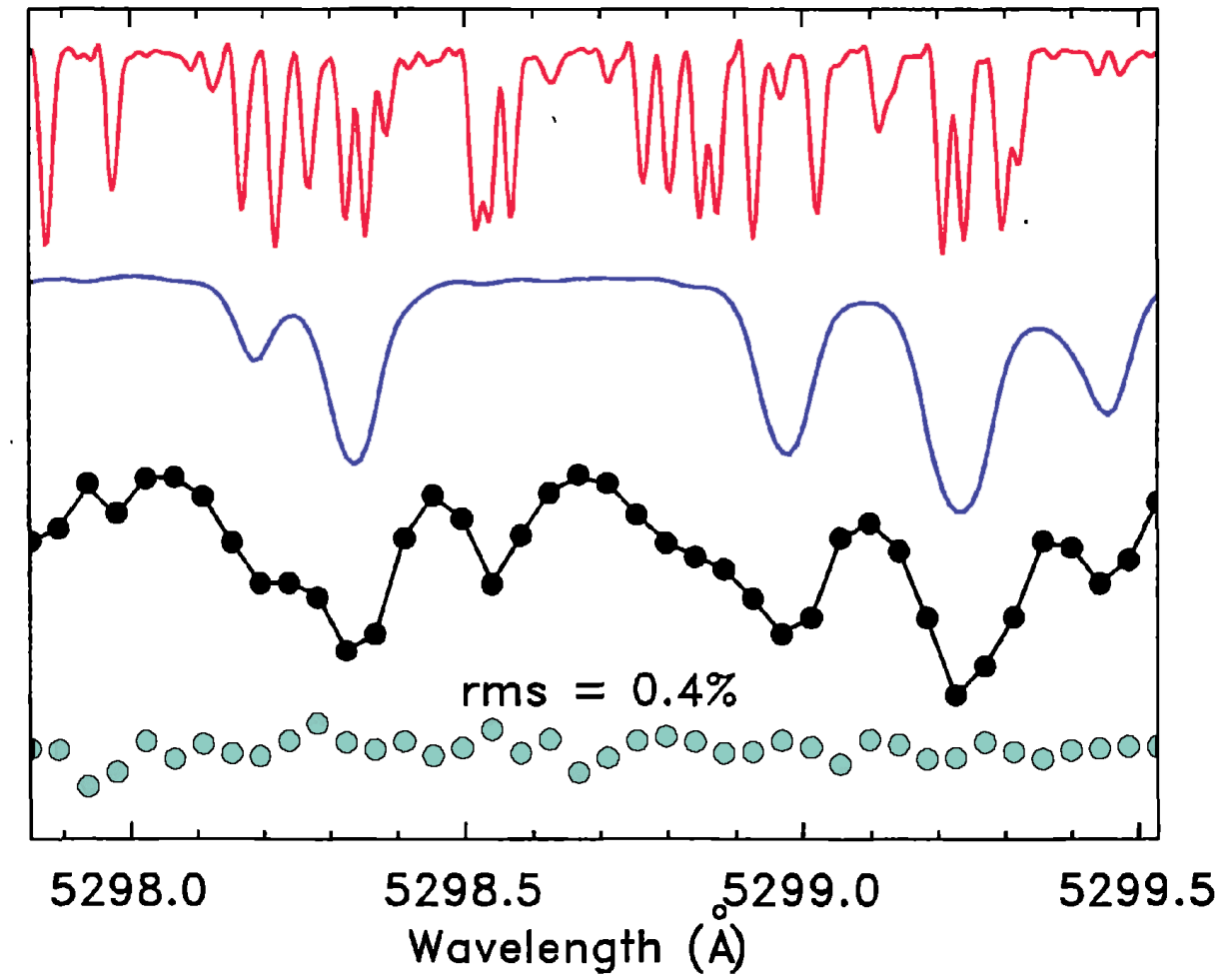

Figure 1 Schematic of the modeling process used to determine wavelength scale using the absorption cell technique. In addition to the measured spectrum (black circles), the high-resolution spectrum of the reference gas (here I_2) (top, red) and template stellar spectrum (second-from top, blue) are used. The spectrometer's point spread function, the wavelength scale, and the total intensity are then fit (13 free parameters) to produce the solid black line. The residuals are teal circles at the bottom. Figure from Ref. [13].

While the absorption cell technique has the key advantage of being compatible with any astrophysical spectrograph in the world, it has a fundamental limitation. Because the spectrograph's point-spread function (PSF) is unknown and described by the sum of 10 Gaussian functions, the number of free parameters in the data extraction is 13: 2 for the wavelength scale, 1 for the Doppler shift, and 10 for the PSF [13]. These extra degrees of freedom "eat up" information which could otherwise be used to more accurately measure the Doppler velocity, decreasing the photon-limited signal-to-noise ratio by a factor of 2 to 2.4 relative to simultaneous emission source calibration [9]. When observing weak objects, this factor of 2 requires either a doubling in the observing time or the use of a much larger telescope, which renders the absorption cell technique unsuitable for the observation of weak objects, especially as part of a survey.

Emission Source Techniques

The alternative to absorption cells is to use an emission source to provide a simultaneous, but not superimposed, wavelength reference. It was this technique that allowed the very first discovery of an extrasolar planet. From 1994 to 1995, M. Mayor and D. Queloz observed 142 stars using the ELODIE spectrograph at the Haute-Provence Observatory, France, with 13 m s^{-1} precision [54]. Orbiting one of these stars, 51 Peg, a Jupiter-mass planet was detected with a 4.23 day orbital period. This discovery not only kicked off the boom in extrasolar planet research, but also validated the simultaneous-source calibration technique.

To make use of an emission lamp, both the stellar light and a calibration beam are sent through the spectrometer together. Typically, the light from each source is delivered to the spectrograph by means of a multimode optical fiber (100-1000 μm in diameter). The fibers are then stacked at the entrance slit of the spectrograph so that the images of the sources are stacked in the detector plane. Because both beams pass

through the spectrograph in precisely the same way, spectral features in the calibration source are used to fix the

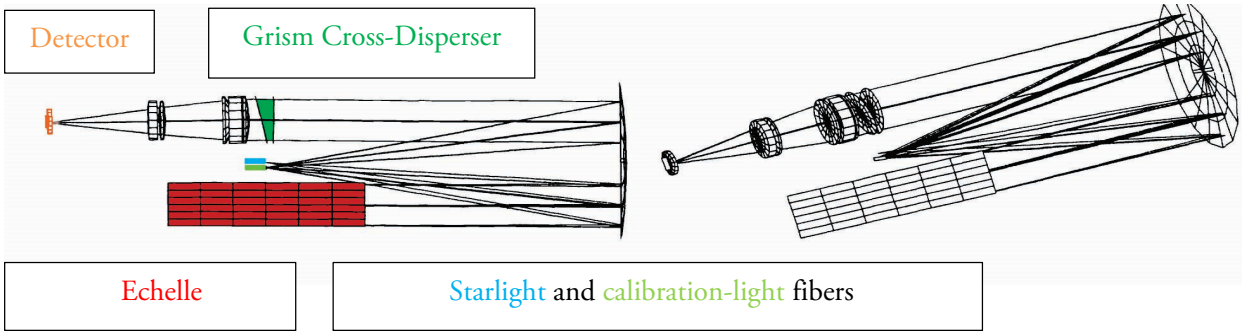

Figure 2 Optical layout and ray-trace of the HARPS spectrograph [8], a second-generation fiber-fed spectrograph for precision astrophysical spectroscopy.

wavelength scale and calibrate the measurement.

Hollow-Cathode Lamp

Hollow-cathode lamps have been used for atomic spectroscopy since the 1920's [75]. These lamps consist of a sealed tube filled with a noble buffer gas, an anode, and a hollow cathode made of a target element. A strong electric field between the anode and cathode ionizes the buffer gas, which is accelerated towards the cathode upon ionization. When the energetic gas atoms impact the cathode, cathode atoms are ejected and excited. As these excited atoms decay into lower energy states, photons are emitted at wavelengths characteristic of each transition. Because this light is generated directly by atomic transitions, it is inherently stable in many cases, particularly for heavy atoms. For astrophysical calibration, heavy atoms with zero nuclear spin, such as thorium and uranium-238, are used to generate rich calibration spectra free of hyperfine splitting.

Thorium argon hollow-cathode lamps were used for the detection of the first extrasolar planets, and have since been shown to provide calibration at the ~ 1 m s^{-1} level [51]. As higher levels of precision are demanded, however, several significant drawbacks of hollow-cathode sources become important. The emission

spectrum of these lamps is very rich in features, and as a result many spectral features are blended, or are not fully resolved. Because the relative intensities of the lines are not completely stable, this presents a major obstacle to calibration. Another complication is the widely varying strength of the spectral features in the lamp's spectrum. Some emission lines are weak, while others are orders of magnitude brighter. Only the overall brightness can be adjusted, and as a result some lines are unusable due to oversaturation while others simultaneously suffer from light-limited signal-to-noise ratios. Finally, hollow-cathode lamps show aging effects. When used as a primary calibration source, the lifetime of a single thorium argon lamp is only 500 hours [68]. During this time, changes in the lamp cause pronounced shifts in the wavelengths of the buffer gas lines and smaller shifts in the cathode lines. While these shifts can be mitigated by use of multiple lamps, this instability prevents the use of lamps as references sources for measurement with sub-m s^{-1} precision.

Fabry-Perot

A partial solution to the shortcoming of hollow-cathode lamp sources has been achieved by filtering white light with passively-stabilized low-finesse Fabry-Perot etalons [95]. This calibration system is based upon a bright white light source, such as a xenon lamp or supercontinuum laser source. Structure is imposed upon the white light interferometrically by means of a Fabry-Perot etalon as shown in Figure 3. The etalon is constructed with low reflectivity mirrors (~ 40 %) which are optically contacted to spacers engineered for an ultralow coefficient of thermal expansion. The etalon assembly is coupled to the light source and spectrograph via multimode optical fiber and housed in a vacuum environment with sub-10 millikelvin stability. This source produces an array of bright spectral peaks with contrast of ~ 10 with very high spectral bandwidth ($\Delta\lambda / \lambda > 0.5$).

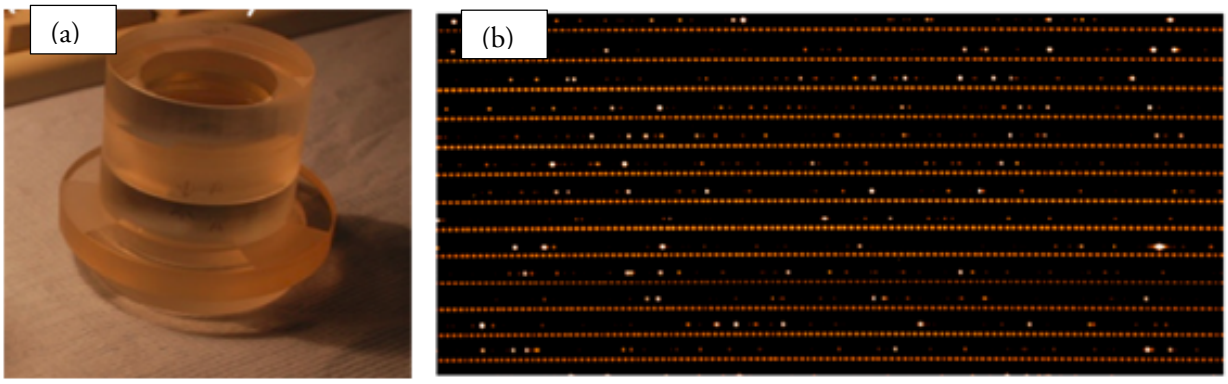

Figure 3 (a) Photograph of passive Fabry-Perot etalon calibrator. Not shown are input and output fibers or coupling optics. Apparatus is housed inside a temperature-stabilized vacuum enclosure. (b) Raw readout of HARPS detector array showing ThAr and passive Fabry-Perot.

Over the short term, this source is capable of very high precision calibration, with stability of below 3×10^{-10} demonstrated in initial trials. A longer-term comparison of the Fabry-Perot calibrator to a thorium argon lamp revealed good precision, with stability of 5 cm s^{-1} $night^{-1}$ but also showed differential drifts of 2 m s^{-1} over a 60 day period [96]. While the uniform, clean spectrum makes this source well-suited to spectrograph calibration, the lack of absolute stability is ultimately inappropriate for use as a calibrator for the ESPRESSO and CODEX experiments. The stability of this system is only passive, provided by the stability of the Fabry-Perot "artifact" and also the stability of the coupling of light into and out of the etalon. Unlike other calibrators, in which long-term stability is referenced to an atomic transition, a Fabry-Perot calibrator can only be *assumed* to be stable over the long term.

Laser Frequency Combs

Laser frequency comb-based calibrators have the potential to provide the bright, uniformly spaced features of a passive Fabry-Perot calibrator with long-term stability exceeding that of hollow-cathode lamps and

absorption cells. By referencing the frequency comb to an atomic frequency standard, it is straight-forward to achieve comb-line fractional accuracy of parts in 10^{13}.

With the stability of the comb mode frequencies guaranteed, the ultimate limits of calibration precision can be considered. In the absence of systematic errors, the limit to the achievable calibration precision of a spectrograph is the shot-noise limited signal-to-noise ratio of the detected frequency comb. This limit is not imposed by the comb itself, as a frequency comb systems the laser's output power-per-mode is sufficient to saturate the spectrometer's detector. Instead, the precision of calibration is determined by the number of comb features which can be used to determine the dispersion of the spectrograph. At low comb-mode densities, the calibration precision will be limited by the uncertainty in each mode, while at high mode densities the comb lines blend into a continuous spectrum. The optimum comb mode density lies between "widely separated" and "blended together". A calculation for optimum shot-noise limited precision has determined that the ideal frequency comb mode spacing is:

$$\Delta f = \frac{1.5 \times 10^6}{R}\ GHz, \tag{2.13}$$

where R is the spectrograph's resolution (λ / $\Delta\lambda$) [57]. For a resolution 50,000 spectrograph, this calculation indicates that the ideal comb-spacing is 30 GHz. It is often the case that a measurement is *not* limited by calibration signal shot-noise, and it is helpful to have a comb mode-spacing up to twice as large—up to 60 GHz--to provide well-separated calibration features.

As will be discussed in the following chapters, there are several key challenges to developing a frequency comb suitable for calibration of an astrophysical spectrograph. The comb must be simultaneously broad-bandwidth, spanning many hundreds of nanometers, and while simultaneously having mode spacing, and therefore pulse repetition rate, of more than 20 GHz. These requirements are difficult to meet, yet the

advantages of a bright and absolutely stable calibrator outweigh the complexity and higher cost of comb-based calibrators, especially for experiments which require sub-m s^{-1} levels of calibration.

Types of Stars and Wavelengths for Spectroscopy

There are multiple types of stars capable of supporting potentially habitable planets. While G-type stars similar to our own Sun are an obvious choice, and have been the subjects of most planet-finding surveys to date, other types of stars also have the potential to support habitable planets. One such type of star is the M-dwarf. Significantly, these stars are extremely common, making up more than 60 % of the stars within 10 pc of the Earth (documented by the RECONS census, http://www.recons.org). They are also relatively stable stars due to their low mass, increasing the likelihood of life developing on a suitable planet. Finally, the physical properties of these stars are well-suited to planet finding, as will now be detailed.

M-type stars are both smaller and cooler than the Sun [3], with masses of 0.075—0.6 times the mass of the Sun and surface temperatures of between 2500 and 3700 K, as compared to the Sun's temperature of 5800 K. Their low masses and temperatures have several important implications for planet finding. Because of

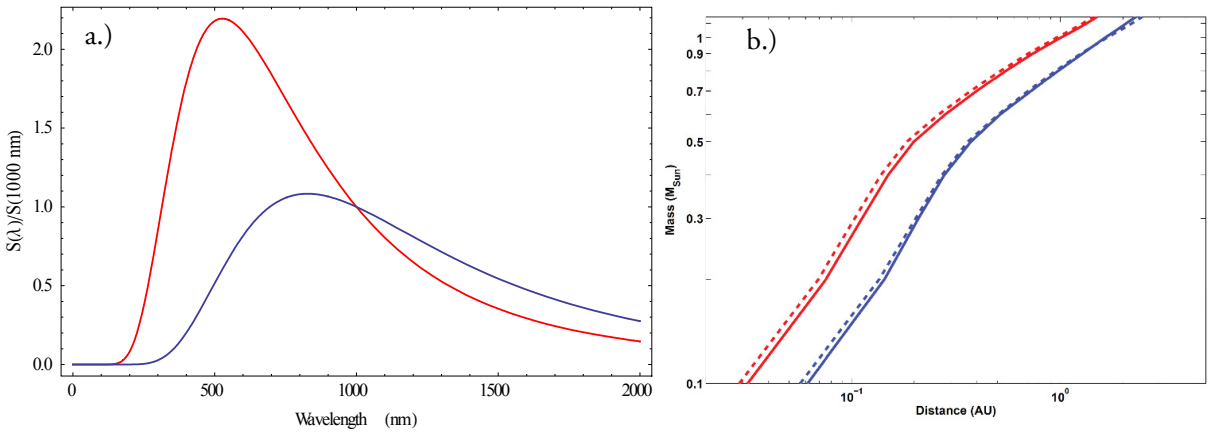

Figure 4 (a) Blackbody spectra in units of relative intensity per nanometer of the Sun [5800 K] (red) and of an M1 dwarf [3500 K] (blue). Unlike the Sun, the cooler star emits the majority of its light in the IR. (b) Inner (red) and outer (blue) edges of liquid-water habitable zones as function of stellar mass. Dashed and solid lines are results from each of two models. This sub-figure from Ref [46].

the relatively low intensity of stellar radiation, the habitable zone -- defined as the range of orbital distances within which a planet could exist with liquid water — is closer to the star than for the Sun, as shown in Figure 4 (b). This increases the effect of an orbiting potentially habitable planet on the star. From Eq. (2.11), we see that, for a fixed planetary mass, the radial velocity signal induced by a planet on a star scales as $\left(r_{\text{semi-major}} m_{\text{star}}\right)^{-1/2}$, and therefore that the smaller orbits and lower stellar masses of M-dwarf stars translate into larger radial velocity signals for potentially habitable planets orbiting them. In practice, this scaling increases the signal by 1 to 2 orders of magnitude with respect to the same planet orbiting a Sun-like star. Another consequence of the lower temperatures of M-dwarf stars is that they are challenging to observe in the visible portion of the spectrum. While the sun is bright from 450—1000 nm, M dwarfs emit most of their light in the near-IR, as can be seen in Figure 4 (a).

The planet finding team at Penn State University has specialized in the search for planets around M dwarf stars using spectroscopy in the near infrared, from 800—1700 nm. Working in collaboration, we at CU and NIST, we have developed frequency comb systems to provide calibration across these wavelengths. This thesis describes the techniques developed for generating a frequency comb with mode spacing of 25—30 GHz across these wavelengths, in addition to the demonstration of the system in an on-sky measurement of stellar radial velocities.

Chapter 3

ERBIUM FIBER TECHNOLOGY

Over the last fifteen years, mode-locked erbium fiber lasers have transitioned from highly experimental laboratory systems to reliable, commercially available devices. The reasons for this are three-fold. Firstly, silica optical fibers have the least loss at a wavelength of approximately 1600 nm, which led the telecommunications industry to select the 1530—1625 nm wavelength band for transcontinental fiber optic communications. The second factor driving the development of mode-locked fiber lasers is the availability of gain fibers doped with the erbium ion, which possesses a metastable state suitable for lasing at 1550 nm and which can be optically pumped with inexpensive solid-state laser diodes. Thirdly, the dispersion of silica glass at 1550 nm is slightly anomalous. Because waveguide dispersion contributes normal dispersion, it is possible to engineer silica fibers with both normal and anomalous dispersion, allowing for all-fiber pulse stretching and compression. These factors lead to capital investments by the telecommunications industry into 1550 nm fibers and erbium fiber-amplifier technologies. As a result, the components required for construction of erbium-doped fiber lasers are readily and inexpensively available.

While there are several designs for mode-locked fiber lasers, such as nonlinear loop mirror "figure-of-8" lasers and linear-cavity lasers mode-locked with semiconductor saturable-absorber mode-lockers (SESAMs), the design of choice for the shortest pulse durations and lowest noise is the polarization-additive pulse mode-locked (P-APM) stretched-pulse laser. In any additive pulse mode-locked laser (APM), pulse shortening is achieved by making use of nonlinear optics to create intensity-dependent gain, or saturable absorption. In the APM scheme, the intracavity optical pulse is split along two arms of an interferometer at some point inside the

laser cavity. The Kerr nonlinearity imposes a differential, intensity-dependent phase shift, which is converted to intensity-dependent loss when the two branches are recombined. Because this scheme uses the Kerr nonlinearity, which operates on time-scales of much less than 10 fs, no limitation on the achievable pulse durations is imposed by the nonlinearity.

In a fiber-laser, P-APM is implemented by using the orthogonal polarization states of light in an optical fiber for the two arms of the interferometer. Using the right (+) and left (-) circular polarization states of light, the coupled-mode equations for the electric field-envelopes A_+ and A_- [$W^{-1/2}$] [1] are

$$\begin{aligned} \frac{dA_+}{dz} &= \frac{i\Delta\beta}{2}A_- + \frac{i\gamma}{3}\left(|A_+|^2 + 2|A_-|^2\right)A_+, \\ \frac{dA_-}{dz} &= \frac{i\Delta\beta}{2}A_+ + \frac{i\gamma}{3}\left(|A_-|^2 + 2|A_+|^2\right)A_-. \end{aligned} \tag{3.1}$$

Here, γ [$W\ m^{-1}$] is the fiber nonlinearity parameter and $\Delta\beta$ [m^{-1}] is the birefringence. It can be shown from this expression that elliptically polarized light, with unequal A_+ and A_-, will evolve by rotation with the degree of rotation dependent upon the instantaneous optical intensity. This effect can be used to create an effective saturable absorber by placing a wave-plate and polarizer after the optical fiber, making use of the intensity-dependent rotation of polarization to achieve intensity-dependent loss. In a fiber laser, the Kerr medium is simply a standard optical fiber, which is both alignment-free and also permits a very high intracavity optical power.

The earliest mode-locked fiber lasers used anomalous dispersion to support an intracavity soliton. In such a soliton laser, an optical pulse with nearly constant temporal duration circulates the laser cavity, supported by the combined effects of nonlinearity and anomalous dispersion. While soliton lasers have some advantages – they need only standard anomalous-dispersion fibers and can operate with low intracavity powers – for ultrafast applications there are significant reasons to use a different design. A key limitation of solitons is the

relationship between peak optical power and pulse duration, caused by the quantization of solitons into multiples of the fundamental soliton energy. While solutions exist for solitons with any integer multiple of the fundamental soliton energy, in a real system with higher-order dispersion only the fundamental soliton is stable. A result of soliton dynamics is that the peak power and pulse duration of the fundamental soliton are related as [1]:

$$P_{\text{peak}} \approx \frac{3.11\left|\beta_2\right|}{\gamma T_{\text{FWHM}}^2}. \tag{3.2}$$

The peak optical power is thus linked to the temporal length of the soliton. This would not be a problem, except that P-APM saturates at high peak powers as the polarization rotation approaches $\pi / 4$. This places a limit upon the peak optical power inside a P-APM mode-locked laser [58],

$$P_0 \leq \frac{0.6\pi}{\gamma_{SA}}, \tag{3.3}$$

where γ_{SA} is the saturable-absorber nonlinearity. With the peak optical power limited, the soliton duration is likewise clamped to some minimum length. For single-mode fiber, $\beta = -21{,}000\,\text{fs}^2\,\text{m}^{-1}$ and $\gamma = 1.1\times 10^{-3}\,\text{W}\,\text{m}^{-1}$, limiting the peak power for even a short 100 fs pulse to approximately 700 pJ inside the laser cavity. For a 250 MHz laser with a 10 % output coupler, these constraints would limit the total laser power to 18 mW.

To avoid the problems inherent with soliton lasers, the stretched-pulse laser was developed, in which the laser cavity is made up of alternating lengths of normal and anomalous dispersion fiber with overall normal dispersion with near-zero magnitude [28, 85]. In this configuration, the pulse is only temporally short for a short time inside the cavity, which reduces the magnitude of nonlinear polarization rotation on each trip and avoids saturation of P-APM. The normal-dispersion cavity also does not support soliton formation, and the

optical bandwidth is thus limited only by the gain spectrum of the laser medium. This type of laser is generally favored for low-noise, fully stabilized laser-frequency combs [87, 97] and is the type used in this work.

Stabilizing the Frequency Comb

While the description of the physics of a mode-locked laser from first principles is very complex, many of the features of the laser can be derived simply from properties of the Fourier transform. A mode-locked laser capable of producing a frequency comb must produce a train of optical pulses. In steady-state, the frequency spectrum of the laser output will be constant, and each pulse will have exactly the same temporal length. These steady-state requirements force the "chirp", or second-order and higher terms of dispersion, to be the same for each pulse. In the time-domain, this requires that the pulse envelope for any pulse leaving the laser be the same as the one before except for a fixed amount of phase, and enforces periodicity upon the electric field

$$\tilde{E}(t - n \times f_{rep}) = \tilde{E}(t - (n-1) \times f_{rep}) \exp\left(-i\Delta\phi\right). \tag{3.4}$$

In a mode-locked laser, the electric field of each pulse has compact support, in the sense that the pulse energy is concentrated into a time much shorter than the interpulse period. It is sensible to describe the pulse train at any time *t* as a sum of infinite copies of the envelope of a single pulse:

$$E(t) = \sum_{n=-\infty}^{\infty} \widetilde{E}_{\text{pulse}}(t - n \times T_{\text{RT}}) \exp(i\Delta\phi\, n) + \text{C.C.}, \tag{3.5}$$

where T_{RT} is the pulse period and $\tilde{E}_{pulse}$ describes the electric field envelope of each individual pulse – commonly a Gaussian or sech function several tens of femtoseconds wide. Such a pulse train is sketched in Figure 5. Even without knowing the exact form of the pulse envelope, the Fourier transform of (3.5) can be calculated,

$$E(\omega) = \widetilde{E}_{\text{pulse}}(\omega) \sum_{n=-\infty}^{\infty} \exp[-in(\omega T_{RT} + \Delta\phi)]\, \delta\left(\omega T_{RT} - 2\pi n - \Delta\phi\right) + \text{C.C.} \tag{3.6}$$

The two terms in Eq. (3.6) describe the important aspects of the frequency comb. The multiplicative term $\tilde{E}_{pulse}(\omega)$ is the Fourier transform of the pulse-envelope, and determines the spectral envelope of the laser output. The summation, which includes a Kronecker delta, shows that the spectrum is not continuous but is the sum of discrete lines – the frequency comb. The non-zero frequency components are regularly spaced, with frequencies

$$f_n = n \times f_{rep} + \frac{1}{2\pi}\Delta\phi\, f_{rep}, \tag{3.7}$$

where the repetition frequency f_{rep} is $1 / T_{RT}$.

From this expression the relationship between the comb-modes and the physical laser properties are apparent. The spacing between the frequency modes is $f_{rep},$ and it can be controlled by simply changing the laser cavity length. In a stretched-pulse mode-locked Er:fiber laser with a free-space section such as the one used in this thesis, this is achieved by incorporating a delay line inside the laser cavity, tuned by use of a piezoelectric transducer.

The carrier-envelope offset frequency depends upon both the repetition frequency and the cavity dispersion, which imparts phase with each round-trip:

$$f_{CEO} = \frac{1}{2\pi}\Delta\phi\, f_{rep}. \tag{3.8}$$

Control of the offset frequency can be accomplished by altering the cavity dispersion, for example by use of an

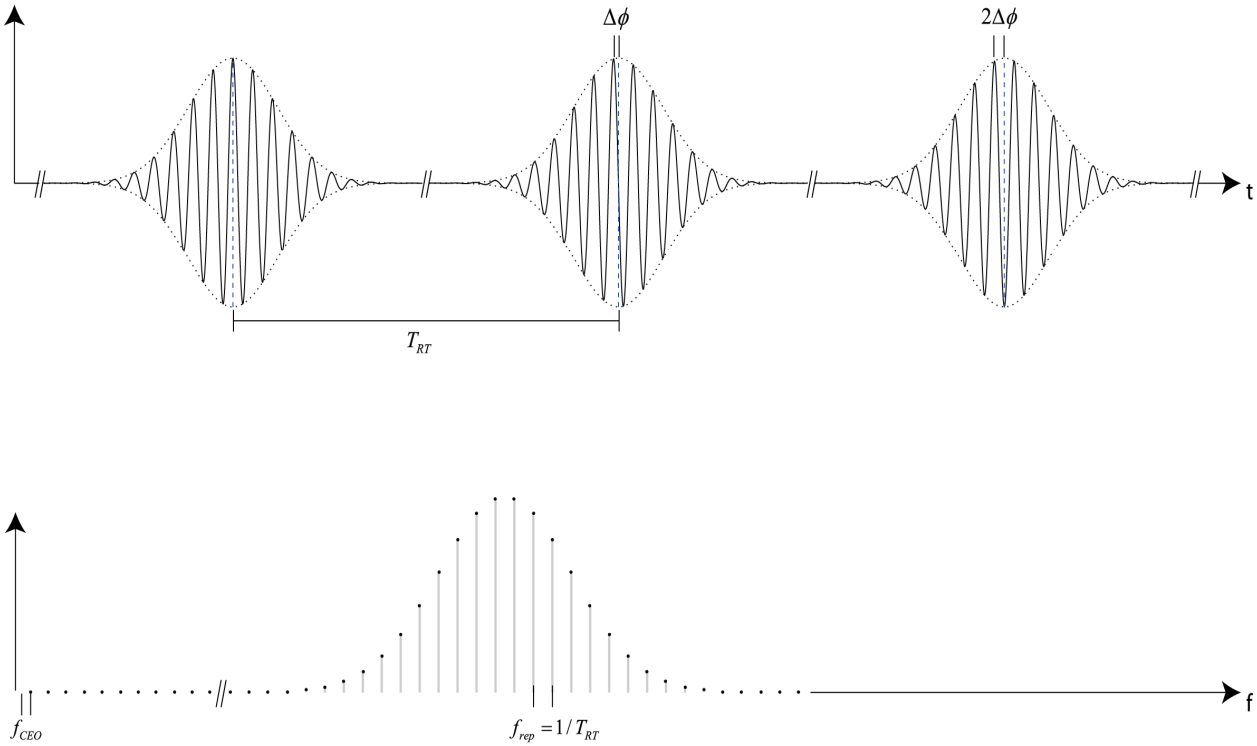

Figure 5 Relationship between time and frequency domains in a laser frequency comb. The top shows the electric field of the pulse train, where the carrier-envelope phase advance Δφ can be seen. The bottom shows the frequency-domain representation of the same pulse train, where the optical frequencies are discrete and the carrier-envelope offset frequency f_{CEO} appears as an overall offset when the comb is extrapolated to 0 Hz.

intracavity wedged prism. On faster timescales, a common mechanism for altering the rate of phase accumulation in a fiber laser makes use of self-phase modulation [59]. By changing the intensity of the pump laser, the pulse energy inside the cavity can be altered on timescales of ~10 kHz, limited by the lifetime of the metastable lasing state. While in general many more linear and nonlinear optical effects are at work, e.g. third-order dispersion, self-steepening, and gain saturation, in "good states" of a laser f_{CEO} exhibits a linear

dependence upon the laser pump current, permitting a servo loop to be established for controlling this degree of freedom.

Fabry-Perot Cavities

The laser frequency combs produced by mode-locked fiber lasers are too densely spaced to be of use for astrophysical spectroscopy. A simple technique for increasing the mode-spacing of laser frequency combs uses a resonant optical filter to selectively transmit a subset of the comb modes [79, 83]. Such a filter can be created using a Fabry-Perot cavity constructed with two low-loss mirrors. These cavities are used in each laser frequency comb apparatus described in this thesis, and it is valuable to formally discuss resonator theory.

To analyze a Fabry-Perot cavity [92], consider two parallel mirrors with reflectivity R_1 and R_2 a distance d apart. Now suppose that a laser beam traveling from left to right is incident upon the cavity. We will call this left-right direction the "+" direction, and the side of the cavity upon which light is incident the "left" side. At the first mirror, the electric field E_L^+ (traveling in the + direction and on the left side of the cavity) is split into a reflected beam E_L^- and a forward-traveling intracavity beam E_{cav}^+. The reflected beam is lost, while the intracavity beam travels a distance d before striking the second cavity mirror, acquiring a phase shift of $\omega n d / c$, where n is the index of refraction. At the second mirror the intracavity field is split into a reflected intracavity field E_{cav}^- and a transmitted field E_R^+. At each reflection, the electric field acquires a phase shift $\phi_m(\omega)$ from the mirror.

Consider the effect of one round-trip through the cavity upon the intracavity field $E_{\text{cav},n}^+$. Beginning with the beam just before reflection from the second cavity mirror, the electric field experiences loss and phase shifts described by

$$E^{+}_{\mathrm{cav},n+1} = E^{+}_{\mathrm{cav},n} \times \underbrace{\exp\left(i\frac{\omega n d}{c}\right)}_{\text{Free-Space}} \times \underbrace{\sqrt{R_1}\exp\left(i\,\phi_{\mathrm{m1}}\right)}_{\text{Reflection by M1}} \times \underbrace{\exp\left(i\frac{\omega n d}{c}\right)}_{\text{Free-Space}} \times \underbrace{\sqrt{R_2}\exp\left(i\,\phi_{\mathrm{m2}}\right)}_{\text{Reflection by M2}},$$

(3.9)

$$= E^{+}_{\mathrm{cav},n} \times \sqrt{R_1 R_2}\exp\left(i\left[\frac{2\omega n d}{c} + \phi_{m1} + \phi_{m2}\right]\right).$$

Note that the reflectivities R_1, R_2 and phase-shifts ϕ_1, ϕ_2 of mirrors m_1 and m_2 are wavelength-dependent, although that dependence is not shown for clarity. The other parameters are the index of refraction n (also wavelength-dependent) and the optical angular frequency ω [rad s^{-1}]. For the short optical cavities considered here, it will later be shown that the dispersion of air can be neglected. Summing the contributions from every possible number of round trips yields the complete intracavity field,

(3.10) $$E^{+}_{cav,m2} = E^{+}_{L}\sqrt{1-R_1}\exp\left(i\frac{\omega n d}{c}\right)\sum_{k=0}^{\infty}\left(\sqrt{R_1 R_2}\exp\left(i\left[\frac{2\omega n d}{c} + \phi_{m1} + \phi_{m2}\right]\right)\right)^{k}.$$

This geometric sum converges to

(3.11) $$E^{+}_{cav,m2} = E^{+}_{L}\sqrt{1-R_1}\exp\left(i\frac{\omega n d}{c}\right)\frac{1}{1-\sqrt{R_1 R_2}\exp\left(i\left[\frac{2\omega n d}{c} + \phi_{m1} + \phi_{m2}\right]\right)}.$$

The fraction of the intracavity field transmitted by the right mirror m_2 is $\sqrt{1-R_2}$, and so the rightward-traveling electric field after the cavity is

(3.12) $$E^{+}_{R} = E^{+}_{L}\exp\left(i\frac{c d}{\omega n}\right)\frac{\sqrt{1-R_1}\sqrt{1-R_2}}{1-\sqrt{R_1 R_2}\exp\left(i\left[\frac{2\omega n d}{c} + \phi_{m1} + \phi_{m2}\right]\right)}.$$

When using the Fabry-Perot cavity as an optical filter, the ratio of the transmitted beam to the incident beam is:

(3.13) $$\frac{I_{\mathrm{out}}}{I_{\mathrm{in}}} = \frac{(1-R_1)(1-R_2)}{1+R_1 R_2 - 2\sqrt{R_1 R_2}\cos\left(\frac{2\omega n d}{c} + \phi_1 + \phi_2\right)}.$$

Using $\cos 2\theta = \cos^2\theta - \sin^2\theta$ and adding and subtracting $2\sqrt{R_1 R_2}$ from the denominator, this simplifies to

$$\frac{I_{\text{out}}}{I_{\text{in}}} = \frac{\left(1-R_1\right)\left(1-R_2\right)}{\left(1-\sqrt{R_1R_2}\right)^2 + 4\sqrt{R_1R_2}\sin^2\left(\frac{1}{2}\left[\frac{2\omega nd}{c}+\phi_1+\phi_2\right]\right)}. \tag{3.14}$$

It can also be important to know the effect of the optical cavity upon the optical phase, which can be determined by considering the ratio of the imaginary to real parts of the complex part of Eq. (3.12), which can be written

$$\frac{1-\sqrt{R_1R_2}\exp\left(-i\left[\frac{2\omega nd}{c}+\phi_1+\phi_2\right]\right)}{\left|1-\sqrt{R_1R_2}\exp\left(i\left[\frac{2\omega nd}{c}+\phi_1+\phi_2\right]\right)\right|^2}. \tag{3.15}$$

In this form, the denominator is purely real, so the phase information is contained in the numerator and the phase shift is

$$\phi = \arctan\left(\frac{\sqrt{R_1R_2}\sin\left(\frac{2\omega nd}{c}+\phi_1+\phi_2\right)}{1-\sqrt{R_1R_2}\cos\left(\frac{2\omega nd}{c}+\phi_1+\phi_2\right)}\right). \tag{3.16}$$

When the cavity mirrors are non-dispersive, ϕ_1, ϕ_2 can be assumed to be zero. By inspecting Eq. (3.14) it is clear that a transmission maximum will occur at all frequencies where

$$m \times \pi = \frac{2\pi fnd}{c}. \tag{3.17}$$

The spacing between resonances is termed the free spectral range, and is given by

$$\text{FSR}=\frac{c}{2nd}. \tag{3.18}$$

Real mirrors are, however, dispersive – the phase shift of light depends upon the optical frequency. This can be qualitatively understood as a frequency-dependent penetration depth of light into the mirror. One approach to accounting for the effect of dispersion upon cavity resonances is to numerically evaluate Eq. (3.14) with experimentally determined values for $R_1(f), R_2(f)$, $\phi_1(f)$, and $\phi_2(f)$. This approach will be used later,

when the action of a Fabry-Perot cavity upon a laser frequency comb is calculated and compared to measurements.

A less exact but conceptually useful approach is to expand $\phi(f)$ as a power series. In this thesis, all cavities are constructed using identical mirrors, and hereafter calculations proceed with $\phi_1(f) = \phi_2(f)$. The first few terms of the expansion are:

$$\phi_1(\omega) = \beta_0 + \beta_1(\omega - \omega_0) + \frac{1}{2}\beta_2(\omega - \omega_0)^2 + \ldots \tag{3.19}$$

Using this expression for $\phi_1(f),$ the resonance condition for Eq. (3.15) is now

$$m \times \pi = \frac{2\pi f n d}{c} + \beta_0 + \beta_1(\omega - \omega_0) + \frac{1}{2}\beta_2(\omega - \omega_0)^2 + \ldots. \tag{3.20}$$

which, after grouping terms, yields an expression for the resonance frequencies f_m

$$f_m = -\frac{c}{2\pi n d}\beta_0 + \frac{c\left(m - \overbrace{\frac{\beta_0}{\pi}}^{\text{offset frequency}}\right)}{2\left(nd + \underbrace{c\beta_1}_{\text{Length shift}}\right)} - \underbrace{\frac{1}{\left(nd + c\beta_1\right)}\frac{c}{2\pi}\frac{1}{2!}\beta_2(\omega - \omega_0)^2}_{\text{Effect of Group-Delay Dispersion}} + \ldots. \tag{3.21}$$

From this expression, the effects of the frequency-independent phase shift β_0 and the linear dispersion (or group delay) β_1 are clear. The new term in the numerator of the first expression shows that both zero and first-order dispersion give rise to an offset frequency, while the term $2c\beta_1$ in the denominator shows that a linear phase ramp effectively changes the cavity length (an expected consequence of the Fourier shift theorem.) The second term gives the effect of second and higher-order dispersion upon the location of the resonances. Unlike the first term, these are frequency-dependent, causing variations in the cavity mode spacing with frequency. It is these terms which are used when calculating the maximum permissible dispersion for broad-bandwidth mirrors.

Effect of Mirror Dispersion

The ultimate limit to the useful optical bandwidth of a Fabry-Perot filter cavity is the dispersive walk-off of the cavity modes. This can be seen in Figure 6, where Eq. (3.21) is evaluated with non-zero β_2, and is due to the fact that while the laser frequency comb modes are each exactly spaced by f_{rep}, the filter-cavity modes are only approximately spaced by the cavity free-spectral range $c / 2d$. In real mirrors, especially low-loss dielectric mirrors utilizing modified quarter-wave stack designs, the phase shift imparted onto light reflecting off of the mirror is dependent upon the wavelength of the light, see Figure 7. While all orders of dispersion contribute to this effect, in this case only the lowest order group-delay dispersion (GDD) is significant.

For the purposes of mirror design, it is useful to know approximately how much GDD can be tolerated before the comb and cavity modes no longer line up. A useful criterion is the point at which the frequency walk-off reaches the cavity half-width at half-maximum (HWHM). In the case of a cavity constructed using two identical mirrors and starting with (3.14), the HWHM is seen to be:

$$\begin{aligned} \delta f_{\mathrm{HWHM}} &= \frac{1}{\pi} FSR \arcsin\left(\frac{(R-1)}{2\sqrt{R}}\right), \\ &\approx \frac{1}{2\pi} FSR \frac{R-1}{\sqrt{R}}, \end{aligned} \tag{3.22}$$

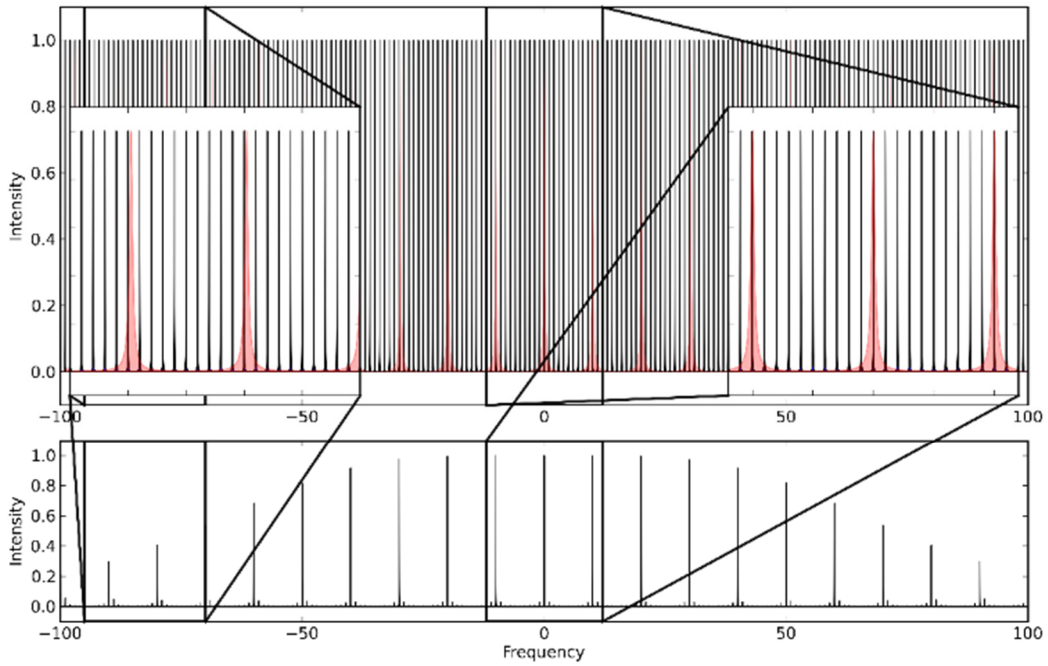

Figure 6 Toy model of cavity including group-delay dispersion. Top: modes of a laser frequency comb (black) and Fabry-Perot cavity (red) with cavity FSR = 10 frep. At center (0) comb and cavity modes are aligned, while at high offsets (±100) group-delay dispersion causes walk off. Bottom: filtered comb, the product of the comb intensity and cavity modes.Walk-off of comb modes leads to both attenuation and asymmetric side-mode levels.

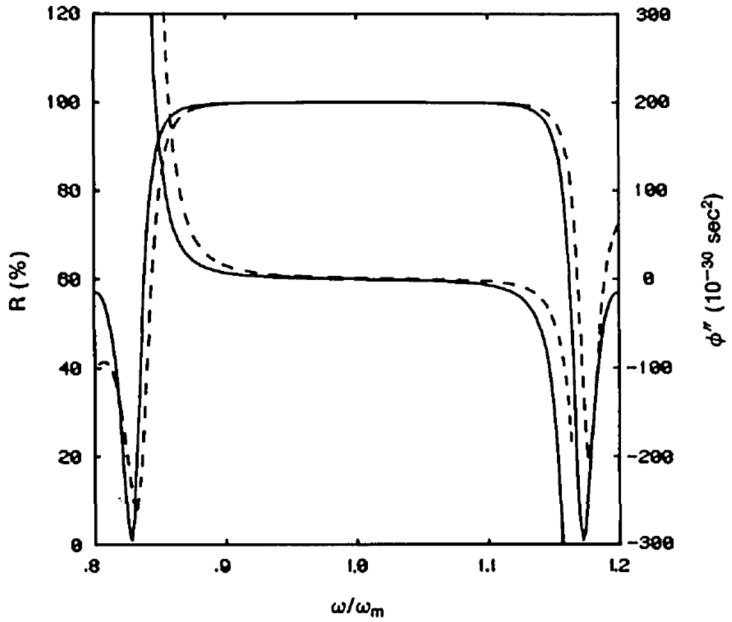

Figure 7 Calculation of reflectivity and group-delay dispersion of quarter-wave Bragg mirror with 19 alternating layers of high and low index (n_H=2.28 and n_L=1.45) materials. The dispersion begins increasing almost immediately, while the reflectivity is essentially flat. For broad-band filtering of frequency combs, the GDD should be less than 5 fs^2. Figure from Ref. [21].

where the approximation is very good, as filter-cavity mirrors are highly reflective (R>0.9). To find the maximum allowable phase shift from higher order dispersion (β_2 and higher terms of the power series expansion of the phase shift), the HWHM is equated with the second part of the left-hand side of Eq. (3.21). It can immediately be seen that the maximum allowable phase is

$$\phi_{\text{HWHM}} = \frac{1}{2}\frac{R-1}{\sqrt{R}}, \tag{3.23}$$

where the identification of $FSR = c\,/\,2\left(nd + c\beta_1\right)$ has been made. While it is possible to derive an expression for the corresponding mean GDD, in practice the dispersion of a mirror coating is not constant but varies with frequency, and it is most useful to compare the integrated GDD with the allowable phase given by Eq. (3.23).

Cavity Design

Choice of Cavity Mirror Curvature

The discussion above describes resonance of an optical beam propagating along the optic axis. While that captures most of the cavity properties, in a real 3-dimensional cavity additional complexities must be considered. Because light can propagate in the transverse direction in addition to the axial, each longitudinal mode supports a family of transverse modes [78]. These modes are have frequencies:

$$f_{qij} = \left[q + \left(i + j + 1\right)\frac{\cos^{-1}\sqrt{g_1 g_2}}{\pi}\right] \times \frac{c}{2L}, \tag{3.24}$$

$$g_1 \equiv 1 - \frac{L}{R_1} \quad \text{and} \quad g_2 \equiv 1 - \frac{L}{R_2}, \tag{3.25}$$

where *q* is the longitudinal mode index, *i, j* are the transverse mode indices, *L* is the cavity length, and R_1, R_2 are the radii of curvature of the mirrors. When used as a filter, an optical cavity is designed so that the fundamental *i,j*=0 modes are resonant with the frequency comb. To effectively filter, no other comb modes

should be resonant with the cavity, and coupling to higher-transverse modes must therefore be suppressed. Suppression is achieved in two ways: by spatial filtering and by choice of the g_1, g_2 parameters. Spatially, the higher-order transverse modes (HOM) are described by orthogonal Hermite-Gaussian functions with dimensions proportional to $\sqrt{i}, \sqrt{j}$. By coupling into and out of the cavity with a single-mode optical fiber, the overlap between cavity's HOM and guided fiber mode is minimized and the coupling of light through the higher order modes suppressed [67].

Coupling via the higher order transverse modes can also be suppressed by designing the cavity such that all HOM are separated in frequency from the comb modes [82]. Because the cavity length L is fixed, this is achieved by choosing appropriate mirror curvatures R_1, R_2. For a given L and a selection of mirrors, the HOM frequencies can be tabulated and a choice made which places only a very high-order (and thus very spatially large) resonance in proximity a mode of the frequency comb.

Mode-Matching

For rejection of higher-order modes and efficient transmission of the filtered comb, good mode matching between the fundamental cavity modes and the single-mode fiber is essential. When a broadband cavity is used it is important that all colors of the comb be simultaneously mode-matched—that is, that the system be free from chromatic aberration. The primary sources of chromatic aberration are the lenses used to couple the comb and cavity light, and these can be minimized by use of achromatic doublet lenses. In addition to the chromatic aberration of the lenses, it is necessary to account for the wavelength-dependence of the mode-field of the guided beam in the single-mode fiber. A basic result of fiber optics [92] is that, in the case of a step-index fiber, the numerical aperture (NA) is determined entirely by the refractive indices of the core (n_2) and cladding (n_1) of the fiber:

(3.26) $$NA = \left(n_2^2 - n_1^2\right)^{1/2}.$$

Over the relatively narrow bandwidth of the light coupled into the comb (<200 nm), the refractive indices can be taken to be constant, and the NA is therefore the same for all colors. In free space, the NA determines the angular spread of the beam as

(3.27) $$\theta = \sin^{-1}\left(\frac{1}{n}NA\right),$$

where θ is the half-angle of beam divergence and n is the index of the medium, here air. For a Gaussian beam, the $1/e$ divergence half-angle of a beam passing through a focus is

(3.28) $$\theta_{1/e} = \frac{\lambda}{\pi w_0},$$

where w_0 is the beam waist at the focus - in this case, at the fiber end facet.

To mode-match the guided mode in the optical fiber to the cavity, two lenses are used-- one acting as a collimator for the fiber and the other focusing into the cavity as shown in Figure 8. At the fiber facet, the beam has infinite radius of curvature and a beam waist

(3.29) $$w_{\text{fiber}} = \frac{\lambda \sin^{-1} NA}{\pi}.$$

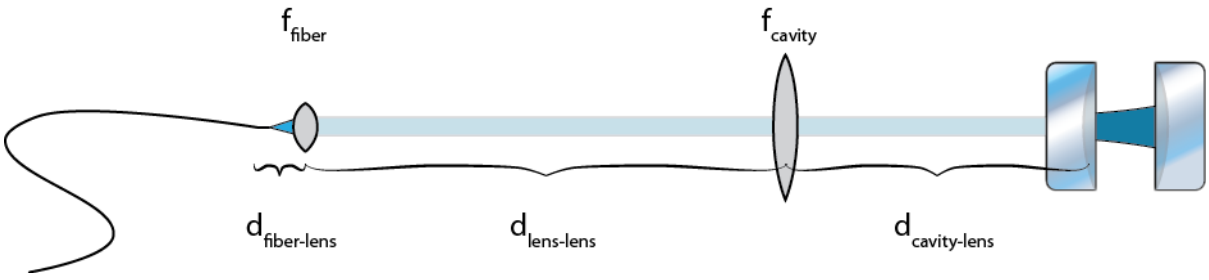

Figure 8 Mode matching optics for coupling light from fiber into TEM00 cavity mode.

Commonly used optical fibers are SMF28e at 1550 nm with NA=0.14 and the polarization-maintaining PANDA 980 and 1550 fibers with NA= 0.09. At the end mirror, the cavity mode has radius of curvature equal to the mirror curvature and a waist determined [78] by:

$$w_1^2 = \frac{L\lambda}{\pi}\sqrt{\frac{g_2}{g_1\left(1-g_1g_2\right)}} \quad \text{and} \quad w_2^2 = \frac{L\lambda}{\pi}\sqrt{\frac{g_1}{g_2\left(1-g_1g_2\right)}}. \tag{3.30}$$

The propagation of the beam from the fiber facet through the two lenses and into the optical cavity can be computed by the ABCD matrix formalism, with the ABCD matrix given by:

$$\begin{pmatrix} 1 & d_{\text{cavity-lens}} \\ 0 & 1 \end{pmatrix}\begin{pmatrix} 1 & 0 \\ -1\,/\,f_{\text{cavity}} & 1 \end{pmatrix}\begin{pmatrix} 1 & d_{\text{lens-lens}} \\ 0 & 1 \end{pmatrix}\begin{pmatrix} 1 & 0 \\ -1\,/\,f_{\text{fiber}} & 1 \end{pmatrix}\begin{pmatrix} 1 & d_{\text{fiber-lens}} \\ 0 & 1 \end{pmatrix}. \tag{3.31}$$

In some cases, it is possible to account for the chromatic aberration of the lenses. Thorlabs, for example, provides the focal length shift for each of its achromatic doublets; these values can be included when Eq. (3.31) is numerically evaluated.

To determine the optimal choices of lenses, a Python script is used to numerically minimize the complex overlap integral between the cavity mode and the propagated fiber mode,

$$\frac{\left|\iint E_{cav}(\mathbf{r})\,\mathrm{E}^*_{fiber}(\mathbf{r})d\mathbf{r}\right|^2}{\iint E_{cav}(\mathbf{r})\,\mathrm{E}^*_{cav}(\mathbf{r})d\mathbf{r}\iint E_{fiber}(\mathbf{r})\,\mathrm{E}^*_{fiber}(\mathbf{r})d\mathbf{r}} = \frac{1}{w_1w_2}\left(\frac{k^2\left(R_1-R_2\right)^2}{4R_1^2R_2^2}+\frac{\left(w_1^2+w_2^2\right)^2}{w_1^4w_2^4}\right)^{-1/2}, \tag{3.32}$$

where the integration is carried out at the mirror over the plane normal to the beam. This closed-form integral is valid for a axially aligned Gaussian beams with curvature *R,* waist *w*, and complex beam parameter

$$\tilde{q} = \left(\frac{1}{R} - i\frac{\lambda}{\pi w^2}\right)^{-1}, \tag{3.33}$$

for which the complex electric field is

$$E(x,y,z) = \frac{1}{\tilde{q}} \exp\left[-\left(x^2 + y^2\right)\left(\frac{ik}{2R} + \frac{1}{w^2}\right)\right]. \tag{3.34}$$

To optimize, Eq. (3.32) is evaluated at all wavelengths of interest and added in quadrature. The three free parameters, d_{fiber}, $d_{lens\text{-}lens}$, and d_{cavity}, are varied by a global optimization routine until an ideal configuration is found. This can be repeated for various choices of collimating and focusing lenses, although it is often possible to find a good solution with any reasonable pair of lenses. An example of such a solution is shown in Figure 9.

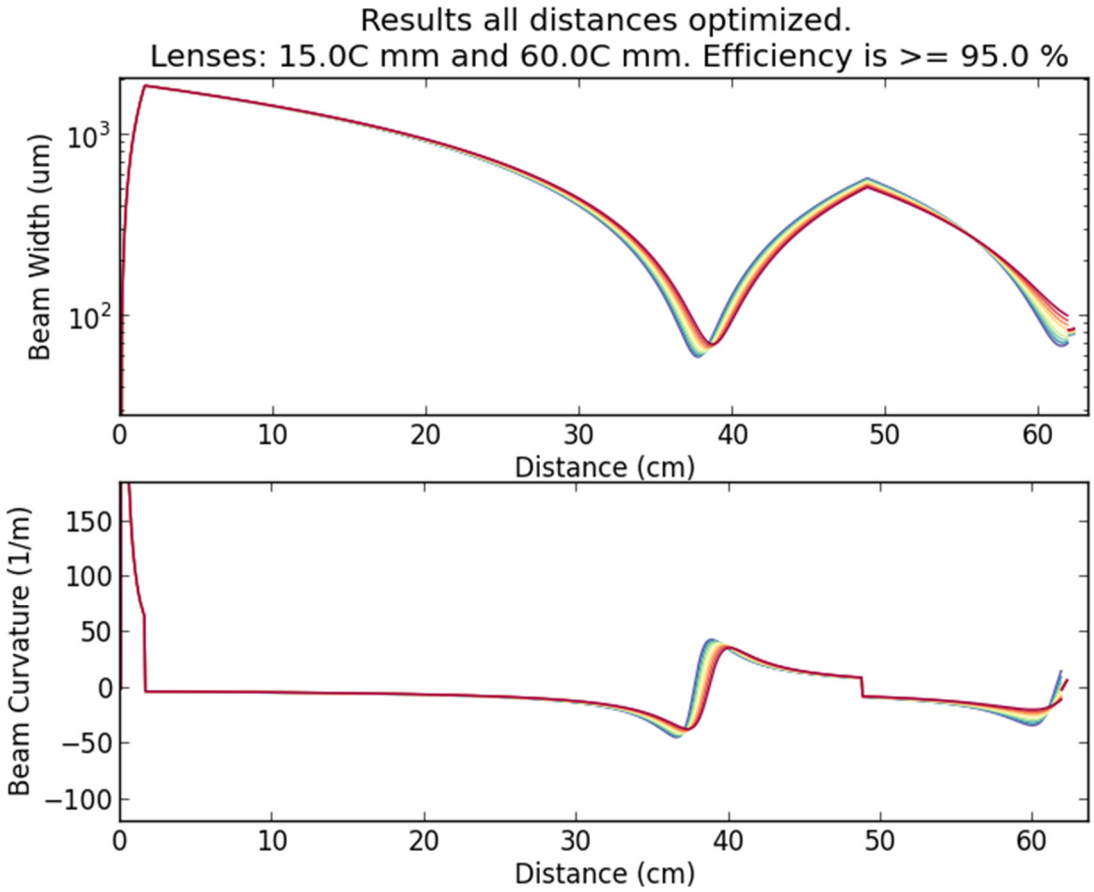

Figure 9 Mode match calculation for broadband 980--1120 nm light using 1.5 cm and 6.0 cm achromatic lenses. From fiber with NA=0.12 into a cavity with FSR=30GHz and mirror radii of curvaure 500 and 100 cm. The solution here has d_{fiber}=1.56 cm, $d_{lens\text{-}lens}$=47.2 cm, and d_{cavity}=13.1 cm. The match is quite good – for the optimal solution shown, the overlap integral is greater than 95 % for all wavelengths.

Locking Scheme

Aligning the resonances of a Fabry-Perot cavity and the frequency comb requires maintaining the cavity length with angstrom-level accuracy. This is accomplished by active control of the filter cavity length; one of the two cavity mirrors is glued to a piezoelectric transducer (PZT) which can be deformed by the application of a high voltage (0-200 V). Length stabilization is achieved by generating an error signal that is proportional to the deviation of the cavity length from resonance and feeding back to the PZT. There are many schemes for generating this error signal, and three were used in this work.

The simplest scheme is the "dither lock", which is a lock-in technique. The cavity length is modulated with small-amplitude and at high-frequency, and the cavity transmission is detected. The demodulating the transmission intensity and selecting the out-of-phase component, a signal is obtained with is positive to one side of the transmission maximum, negative to the other, and zero on resonance. A second technique which can be used is the Pound-Drever-Hall (PDH) technique [22], which takes advantage of the the asymmetric phase shift imparted on frequencies above and below the cavity resonance. Frequency side-bands are placed on a laser, either the frequency comb or a CW laser stabilized to the comb, using an electro-optic phase modulator (EOM.) The laser and sidebands are coupled into the cavity, and the reflected light is monitored. By photodetecting the reflected light and then mixing the signal with the modulation frequency, the mean phase shift of the reflected light is measured. Again, this provides a signal which is odd with respect to the cavity resonance, and can be used for electronic feedback. A third technique is a variation on PDH, in which the asymmetric phase shift imparted upon higher-order modes is used [77]. By slightly misaligning the optical cavity and detecting the reflected beam using a split-detector, an error signal very similar to the PDH signal can be obtained. This scheme, however, is dependent upon the physical alignment of the optical cavity and is not ideal for long-term stability. Instead, the dither and PDH schemes were used. The dither-lock has the advantage of extreme simplicity, while the PDH lock is very robust and especially useful when the cavity is stabilized to a CW laser.

Physical Design of Cavity

Some trial and error was required to find a good design for mechanically mounting the mirrors that comprise the filter cavities. Initially, cavities were constructed by mounting one mirror to a translation stage, which was clamped to the optical table. The second mirror was held in a kinematic mount and similarly attached to the table. While this design was very easy to construct and provided simple length control via the translation state, amplitude table vibrations resulted in large variations in cavity length. To minimize these fluctuations, a design which placed both mirrors in a common fixture was adopted, shown in Figure 10. A metal block forms the cavity foundation, to which one mirror is directly glued. The second mirror is mounted in a 3-axis kinematic mount which is in turn bolted to the cavity foundation, providing both tip-tilt and length adjustment. Course length adjustment is accomplished by an array of ~ 2 mm-spaced mounting locations for the kinematic mount. To minimize cost while allowing simple alignment, the cavity foundation fits into a commercial 5-axis stage designed for aligning optical isolators with an optic axis. This design has been found to be very robust, with almost no drift of the cavity mirrors and good isolation of the cavity from vibrations in the optical table.

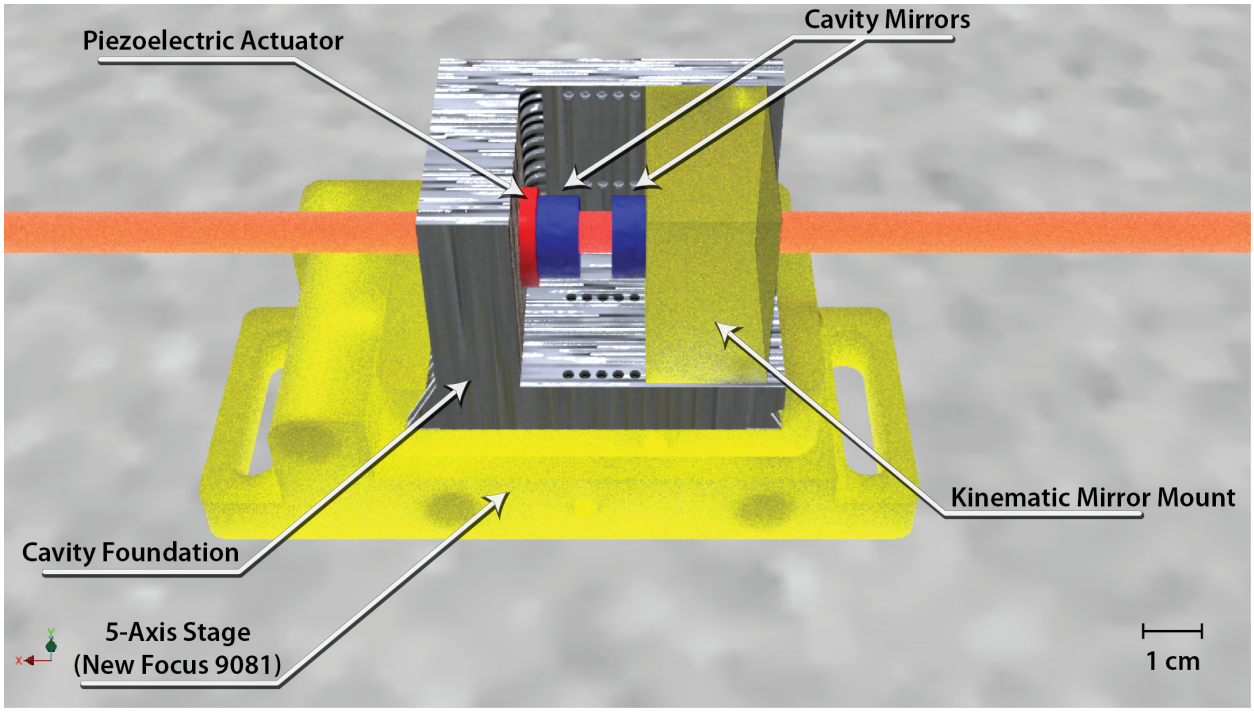

Figure 10 Optomechanical design of Fabry-Perot filter cavity. The cavity foundation is a machined block of stainless steel. A piezoelectric actuator is attached with epoxy to this block, and one of the cavity end mirrors is glued to the actuator. The other end mirror is mounted into a 3-axis kinematic mount which is attached to the foundation with screws. Tip-tilt alignment and coarse adjustment of the cavity length is provided by the kinematic mount, while fast length control is provided by the piezoelectric transducer. The cavity assembly is mounted into a 5-axis stage for alignment of the cavity mode with the input and output beams.

Chapter 4

MEASUREMENT TECHNIQUES

By any measure, the dynamic range of laser frequency combs is enormous. In the time domain, a temporally compressed pulse from a mode-locked laser is concentrated into just a few hundred femtoseconds, while the spacing between pulses is more than a nanosecond – more than ten thousand times longer. The frequency domain is even more extreme. While individual frequency comb modes have linewidths of between one and one million hertz, the total bandwidth of an octave-spanning comb is more than 150 terahertz, implying that measurement of an entire comb while resolving the structure of each comb mode would require simultaneous measurement across eight to fourteen orders of magnitude. This range of length scales is enormous, equivalent to the number of carbon atoms on the surface of a 0.25 carat diamond. In the same way that one would measure the physical size of a diamond with a ruler but characterize structure of the crystal lattice with diffraction or atomic force microscopy, a number of different measurement techniques are combined to understand the properties of a laser frequency comb at different length scales. In this chapter, measurement techniques in both frequency and time domain will be described.

Frequency Domain

Optical Superheterodyne

To characterize a single mode of a laser frequency comb, the comb's optical frequency must be converted into a radio-frequency signal. This conversion is most commonly performed by use of the superheterodyne (hereafter simply referred to as heterodyne) technique. First developed for converting radio signals into audio frequencies, a heterodyne receiver uses a reference signal (local oscillator, or LO) and a square-

law mixer to detect the low frequency beat between the high frequency signal and LO [33]. In the context of laser characterization, the LO is a stable, independent laser, the signal is the unknown laser source, and the mixer is a photodiode. In an optical heterodyne measurement, the signal and LO beams are combined on a photodiode (PD). By using an LO laser that differs in frequency from the signal laser by only MHz to GHz, a radio signal is generated, which can be analyzed with conventional radio-frequency instrumentation such as radio-frequency spectrum analyzers (RFSA) and frequency counters.

To understand the relative amounts of signal and noise in a heterodyne measurement, it is necessary to look at how the beat signal is generated. When signal and LO fields of the same polarization state are incident upon a photodiode, a photocurrent proportional to the square of the electric field is generated:

$$i(\mathrm{t}) = \varepsilon \iint_{\mathrm{PD}} \left| E_{\mathrm{LO}}(\mathbf{r}) \exp(-\mathrm{i}\left(\omega_{\mathrm{LO}} t + \phi_{\mathrm{LO}}(\mathbf{r},t)\right) + E_{\mathrm{sig}}(\mathbf{r}) \exp(-\mathrm{i}\left(\omega_{\mathrm{sig}} t + \phi_{\mathrm{sig}}(\mathbf{r},t)\right) \right|^2 dA, \tag{4.1}$$

where the function $E_{\mathrm{LO}}(\mathbf{r})$ and $E_{\mathrm{sig}}(\mathbf{r})$ are the (scalar) electric fields and ε is the photodetector's conversion efficiency [A $\mathrm{V}^{-1/2}$]. When the two beams are combined in single-mode fiber, as they are for measurements in this thesis, the spatial overlap between the signal and LO fields becomes perfect and the integration over the detector area is trivial. In this case, Eq. (4.1) reduces to

$$i(\mathrm{t}) = \varepsilon A_{\mathrm{eff}} \left(E_{\mathrm{LO}}^2 + E_{\mathrm{sig}}^2 + 2E_{\mathrm{LO}} E_{\mathrm{sig}} \cos\left(\left(\omega_{LO} - \omega_{\mathrm{sig}}\right) t + \left(\phi_{\mathrm{LO}}(t) - \phi_{\mathrm{sig}}(t)\right)\right)\right). \tag{4.2}$$

Here, the first two terms are the DC currents from each of the LO and signal fields, while the third term is an oscillating current at the beat frequency between the two. In a practical measurement, the ε and A_{eff} coefficients are not known, and it is helpful to recast the expression in terms of more readily measureable quantities. Note that alone, each of the LO and signal fields alone will generate a photocurrent

$$i_{\mathrm{LO}} = \varepsilon A_{\mathrm{eff}} \left| E_{\mathrm{LO}} \right|^2 \quad \text{and} \quad i_{\mathrm{sig}} = \varepsilon A_{\mathrm{eff}} \left| E_{\mathrm{sig}} \right|^2. \tag{4.3}$$

These photocurrents can be determined by simply blocking each beam and measuring the photocurrent produced by each of the LO and signal beams alone. With this in mind, Eq. (4.2) can be cast in terms of these photocurrents as

$$i(\mathrm{t}) = i_{\mathrm{LO}} + i_{\mathrm{sig}} + 2\sqrt{i_{\mathrm{LO}} i_{\mathrm{sig}}}\cos\Big(\big(\omega_{LO} - \omega_{\mathrm{sig}}\big)t + \big(\phi_{\mathrm{LO}}(t) - \phi_{\mathrm{sig}}(t)\big)\Big). \tag{4.4}$$

The dominant source of measurement noise in a heterodyne receiver is the shot noise of the photocurrent. Because the photocurrent is quantized by the electronic charge, the photocurrent contains statistical fluctuations [36]. If the photoelectrons are assumed to be independent, white noise is produced with power density

$$\frac{I_{\mathrm{shot}}^2}{B} = 2qI_{\mathrm{DC}}, \tag{4.5}$$

where B [Hz] is the measurement frequency bandwidth and q [C] is the electron charge. For a typical optical heterodyne measurement, the LO power is much greater than the signal, and the DC photocurrent is approximately i_{LO}. In this limit, an expression for the shot-noise limited signal-to-noise ratio for a heterodyne measurement can be formulated:

$$\frac{P_{\mathrm{het}}^{\mathrm{RMS}}}{P_{\mathrm{shot}}} = \frac{i_{\mathrm{sig}}}{2qB}. \tag{4.6}$$

A key advantage of the heterodyne technique is the suppression of other noise sources, such as technical noise on the amplitudes of the signal and LO lasers. Sources of amplitude-modulation noise are relatively slow, becoming negligible at a few MHz, and by tuning the LO laser such that the beat note occurs at a frequencies far from DC, most technical noise can be made negligible. Further, because the signal-to-noise ratio scales only with the signal power, broadband noise on the signal laser far removed from the beat frequency can be “buried” under the shot noise floor by simply increasing the LO power.

Grating Optical Spectrum Analyzer

The most straightforward technique for measuring the spectral envelope of a broad-band light source such as a frequency-comb is the grating monochromator. Using single-mode beams, it is possible to achieve extremely high resolution using simply a photodetector, a diffraction grating, and an optical slit. When a beam of light is incident upon a grating at angle α, diffracted beams form at angles β satisfying the expression

$$m G \lambda = \sin\beta - \sin\alpha, \tag{4.7}$$

where G [m^{-1}] is the grating's ruling density, λ is the optical wavelength, and m is an integer. By careful optical design, a monochromator can be engineered such that, as the grating is tilted, different colors of light pass through a slit placed at some fixed angle relative to the incident optical beam. For measurements of the optical spectrum, we use a commercial monochromator ("optical spectrum analyzer") carefully engineered to achieve up to 0.02 nm (2—16 GHz) resolution from 600—1700 nm with good accuracy and with low stray-light or cross-order contamination.

Time-Domain

While the astronomy applications of the laser frequency comb are inherently frequency-domain, nonlinear optical techniques are driven by the high peak powers associated with ultra-short pulses. When building and characterizing portions of the comb system that make use of nonlinearities, it is therefore necessary to understand the character of the laser in the time-domain. One approach to measuring optical pulses is to use a high-speed photodiode and sampling oscilloscope to measure the optical pulse train; however, while this technique has some usefulness in laser characterization, it is not able to resolve features shorter than several picoseconds due to the few-GHz bandwidth of photodiodes.

To avoid the limitation of electronic response time, various techniques have been developed which use a short optical pulse to measure itself. Two of these schemes are used for this work: background-free second-

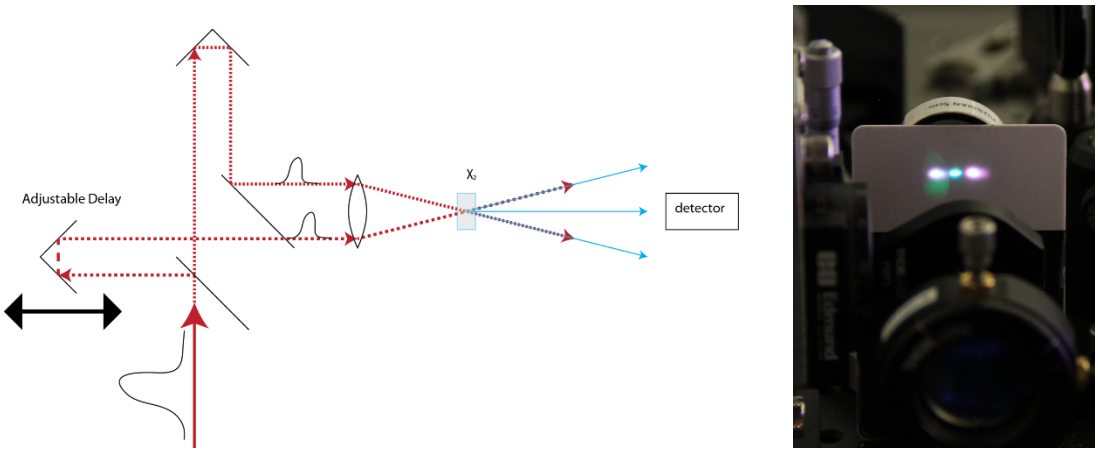

Figure 11 Left: Schematic of autocorrelation and FROG schemes. The optical pulse is split into two copies (dashed lines) which are crossed in a SHG medium (BBO or KTP). In the background-free configuration shown, the beams cross at an angle so that the cross-correlated light has zero momentum in the x and y directions and leaves the crystal in a "straight line." Right: Photograph of autocorrelation at 1030 nm. Purple-colored beams are the infrared 1030 nm fundamental light, while the green beam is their cross-correlation.

harmonic generation autocorrelation (AC) and second-harmonic frequency resolved optical gating (SHG-FROG). These techniques are closely related, with FROG being derived from the autocorrelation, and so we will first discuss AC and then move on to FROG.

The principle of an optical autocorrelator is to split an optical pulse into two copies, introduce a variable delay between the two copies, and then measure the nonlinear interaction between the two copies as a function of the delay. This scheme is shown in Figure 11. Mathematically, consider a single optical pulse with electric field envelope $E_{\text{sig}}(t)$. Two spatially overlapped copies of the pulse delayed by time τ will interact in a χ_2 medium to produce a second-harmonic field [10]

$$E_{\text{SHG}}\left(\omega_1+\omega_2,\mathrm{t};\tau\right)\propto 2\chi_2 E_1\left(\omega_1,t\right)E_1\left(\omega_2,t-\tau\right). \tag{4.8}$$

In an SHG-autocorrelator, the second harmonic field is detected by a point detector, which integrates over ω, and because the scanning of τ is slow with respect to both the optical cycle time and also the inter-pulse period,

the signal is time-averaged with respect to t. The autocorrelation signal is thus a function only of the delay [89],

$$I_{\mathrm{SHG}}(\tau) \propto \chi_2^2 \int_{-2/frep}^{2/frep} \left| E(t)E(t-\tau) \right|^2 dt. \tag{4.9}$$

As the time delay is scanned, second harmonic light with intensity proportional to product field strength is produced. When the pulse shape is known, the width of the autocorrelation can be used to compute the pulse duration. In cases where the pulse shape is not *a priori* known, however, the autocorrelation of a pulse is not sufficient for determination of the pulse shape. This can be understood by an "information loss" argument – the optical pulse's envelope has both intensity and phase as a function of time. The autocorrelation is a real function of time, and so half of the information is immediately lost. Less obvious is the fact that many different pulses have very similar autocorrelations [18]; as a pulse is propagated through gain and nonlinear fibers, the assumption of a simple pulse is no longer valid.

FROG

If a pulse is determined by the electric field's intensity and phase, one would expect that the measurement of a two-dimensional spectrogram should be sufficient to fully characterize the pulse. As it turns out, this is completely true. By replacing the wavelength-integrating detector in the autocorrelator described in (4.9) with a spectrometer, the second-harmonic spectrum can be measured as a function of the delay τ

$$I_{\mathrm{SHG}}(\omega;\tau) \propto \chi_2^2 \int_{-2/frep}^{2/frep} \left| E(t)E(t-\tau)\exp(-i\omega t) \right|^2 dt. \tag{4.10}$$

This produces a two-dimensional spectrogram in frequency and delay, which is, for all practical purposes, uniquely mapped onto a single complex pulse envelope. To determine the envelope function, the spectrogram

is inverted by randomly perturbing an initially random complex field and computing its spectrogram until a good match between the measured and computed spectrograms is obtained. While the basic algorithms for this processes are well documented in the literature, we use commercial software by the now-defunct Femtosoft, LLC for the retrieval.

A key limitation is the ambiguity in the direction of time. Because of the symmetry with respect to the sign of τ in Eq. (4.10), the FROG measurement cannot distinguish between $E(t)$ and $E(-t)$. While there does not at first seem to be of any consequence of this, a problem immediately arises when using FROG to characterize the dispersion or chirp of an optical pulse. Group-delay dispersion and all other even-order terms (quartic, etc) change the pulse shape in a way that is odd in time; a positively chirped pulse is one in which red colors arrive first, while a negatively chirped pulse leads with the blue edge. Because SHG-FROG cannot determine the direction of time, it cannot distinguish positive and negatively-signed chirps. While it is possible to break this ambiguity by introducing satellite pulses, for example by using a microscope slide as an etalon, it is usually possible to unambiguously determine the pulse chirp in a series of measurements by simply knowing the sign of the dispersion of the fiber along which the pulse is traveling.

Each of these techniques is used at various points in the development of the frequency comb-calibrator. Optical heterodyne measurements are key to understanding the behavior of the filter cavities and the effects of nonlinear broadening on the filtered comb. The grating monochromator provides a quick picture of the comb spectrum, and the autocorrelation and FROG measurements provide insight into the time-domain of the comb.

Chapter 5

25 GHZ ERBIUM COMB CALIBRATOR

Introduction

This chapter describes the first-generation laser frequency comb developed at CU and NIST for the calibration of astronomical spectrographs in the H band, 1500—1800 nm. Originally developed for use with the University of Florida FIRST spectrograph, this frequency comb is based upon a mode-locked erbium fiber laser which is filtered to 25 GHz and then nonlinearly broadened to cover the H band. While as of this writing the FIRST spectrograph is still in development, and it is unlikely that the comb described here will ever be put to use as a permanent calibrator, this comb system has yielded significant scientific results. In addition to investigating the fundamental laser optics of filtered frequency combs, we were able to work in collaboration with the spectroscopy team at Penn State University to demonstrate the frequency comb on the test-bed near-infrared Pathfinder spectrograph. This chapter discusses first the development of the comb at NIST, then presents measurements of the comb performed in the laboratory, and finally presents the results of the coupling of the comb to the Pathfinder spectrograph at the McDonald Observatory.

Generation of the 25 GHz Frequency comb

Stabilization of the mode-locked Er:fiber laser

The calibration laser frequency comb (LFC) is generated from the filtered spectrum of a 250 MHz passively mode-locked erbium fiber laser [97], similar to the one built and characterized in Ref. [67]. The frequency of each optical mode is determined by the comb equation,

(5.1) $$f_n = n \times f_{\text{rep}} + f_{\text{ceo}}$$

where f_{rep} is the laser's repetition rate, f_{ceo} is the carrier-envelope offset frequency, and n is an integer on the order of 10^6. To frequency stabilize the mode-locked laser (MLL), the frequencies f_{rep} and f_{ceo} must be detected and locked. The most straightforward detection of f_{ceo} requires an octave-spanning spectrum [39]. Using an Er:fiber amplifier and polarization-maintaining highly nonlinear fiber [32], f_{ceo} is detected and locked to 160 MHz by modulation of the MLL's pump laser diode. The repetition rate, f_{rep}, is directly detected and locked by controlling the laser cavity length. By referencing the synthesizers to which f_{ceo} and f_{rep} are locked to a global positioning system-disciplined rubidium clock, the frequencies of the laser modes are fixed with a fractional uncertainty of 10^{-10}, limited by the accuracy of the clock.

The laser's repetition frequency is detected by simply picking off a small fraction of the laser's pulse train and sending it to a high-speed photodiode. To increase the sensitivity to variations in the laser's repetition

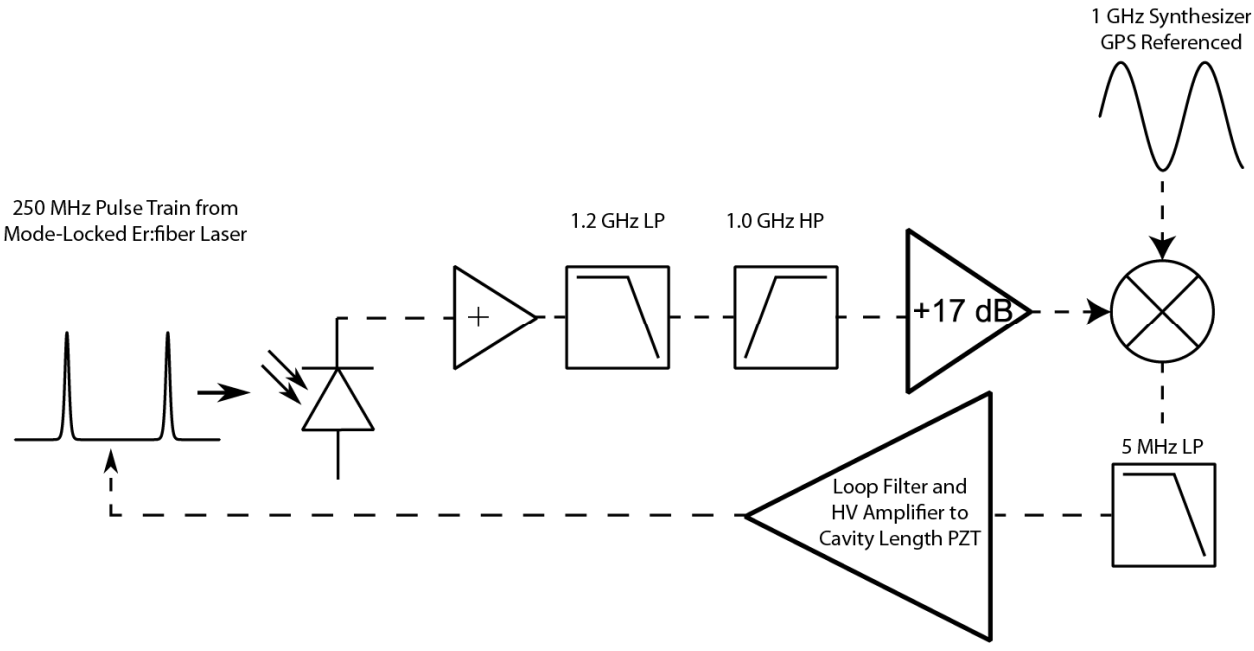

Figure 12 Details of electronics locking f_{rep} to 1 GHz GPS-disciplined oscillator.

rate, the fourth harmonic of the pulse frequency (1 GHz) is used, multiplying frequency variations by 4. To stabilize the frequency to a synthesized reference, basic RF electronics such as amplifiers, filters, and a frequency mixer are used, shown in detail in Figure 12. The difference frequency between the measured and synthesized 1 GHz tones is processed using a PI loop filter, then fed back to the cavity length via a high-voltage amplifier driving an in-cavity piezoelectric transducer (PZT). This servo has a bandwidth of ~10 kHz, limited by the mass of the end mirror actuated by the PZT.

The carrier envelope offset is a common-mode frequency shift of all comb modes, the residual frequency when equation (5.1) is extrapolated to n = 0. Detection of f_{ceo} is accomplished with the f-2f optical heterodyne technique. The frequency comb is amplified and broadened to span from 1000 to 2000 nm. A narrow band of the spectrum around 2000 nm is frequency-doubled in a periodically-poled lithium niobate (PPLN) crystal. The resulting frequency-doubled light and the (non-doubled) portion of the supercontinuum at 1000 nm are optically heterodyned on a photodiode, resulting in a signal at base-band with frequency:

$$f_{\text{beat}} = \left| 2 \times \underbrace{(n \times f_{\text{rep}} + f_{\text{ceo}})}_{\text{f}} - \underbrace{(2 \times m \times f_{\text{rep}} + f_{\text{ceo}})}_{\text{2f}} \right|, \tag{5.2}$$

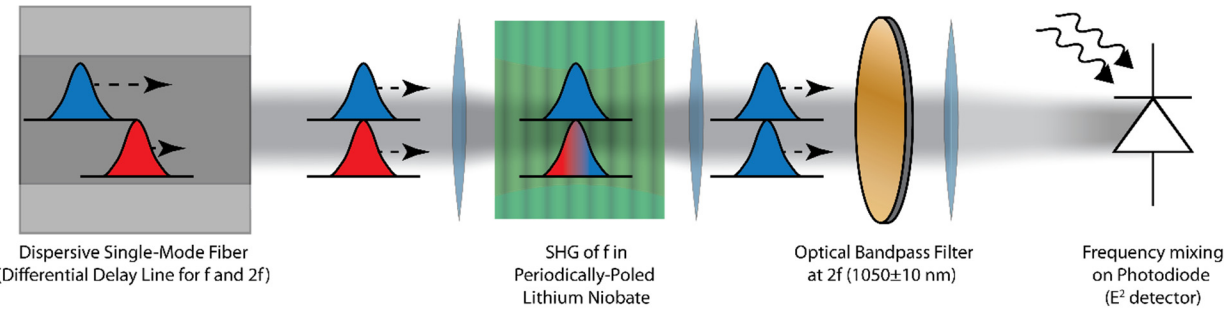

Figure 13 Schematic of co-linear f-2f interferometer. During supercontinuum generation, the bluer light is temporally behind the redder light. A fiber delay line removes the offset, temporally aligning the pulses at f and 2f. The octave-spanning continuum is launched into free-space and focused into a periodically-poled lithium niobate crystal (PPLN) which is designed to phase match the frequency doubling of f to 2f. A bandpass filter then isolates the light at 2f, which is then focused onto a photodiode. The heterodyne beat provides the carrier-envelope offset frequency as discussed in the text.

where *m* and *n* are integers. The first term is the contribution of the frequency-doubled light and the second is the fundamental. When *m* and *n* are exactly equal, the difference frequency f_{beat} is equal to f_{ceo}. It is important to note that, when a real signal is detected, beat frequencies for values of $m = n, n \pm 1, n \pm 2, \ldots$ are present, giving rise to beat notes at f_{CEO}, $f_{rep} - f_{CEO}$, $f_{rep} + f_{CEO}$, ... Typically, one of the two beat notes between 0 Hz and f_{rep} is used for stabilization, and because f_{CEO} can be greater than $f_{rep} / 2$, it is necessary to determine whether the detected peak is f_{CEO} or $f_{rep} - f_{CEO}$.

To stabilize the carrier-envelope offset frequency, the radio-frequency signal from the photodiode is digitally divided by 8 to reduce noise and then phase-locked to a synthesized 17.5 MHz reference frequency. The frequency synthesizers stabilizing f_{rep} and f_{ceo} are themselves referenced to a GPS-disciplined rubidium oscillator with accuracy of parts in 10^{11}, a level capable of supporting cm/s calibration.

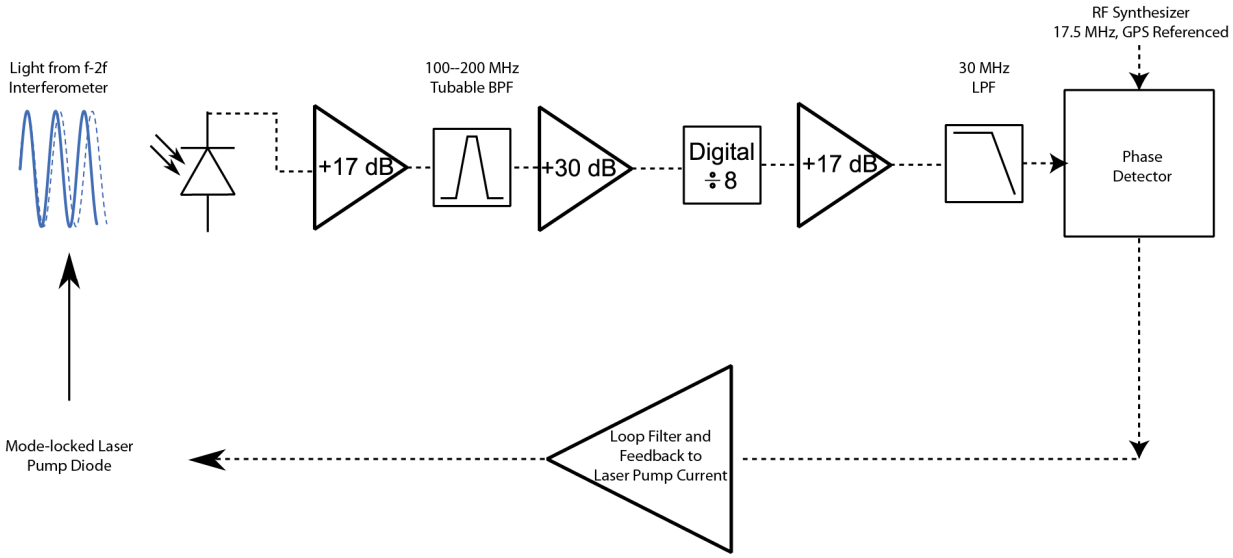

Figure 14 Scheme for locking f_0 to GPS-disciplined RF signal.

Filtering to 25 GHz

For the calibration of the Pathfinder astronomical spectrograph (resolution $\lambda/\Delta\lambda = 50{,}000$), we chose to use a comb mode-spacing of 25 GHz, which provides one comb line every 6.5 resolution elements. This wide mode-spacing allows clear resolution of the comb modes when calibrating the spectrograph, making the calibration both simpler and more precise. The mode-locked laser used in these experiments has a repetition frequency of 250 MHz, and therefore a 100-fold increase in the mode-spacing is required. To generate this spectrum, the Fabry-Perot mode-filtering scheme [79, 44, 16] is employed, discussed in detail in Chapter 3. Two identical filter cavities are constructed, using mirrors with reflectivities of 99.8% and radii of curvature 5 cm and 10 cm, spaced by ~ 0.6 cm for a free-spectral range of 25 GHz and finesse of approximately 2000. Fine, high-speed control of the cavity length is provided by a ring-shaped PZT, to which one mirror in each cavity is glued. The fundamental transverse cavity modes are coupled to standard single-mode fiber (SMF) using

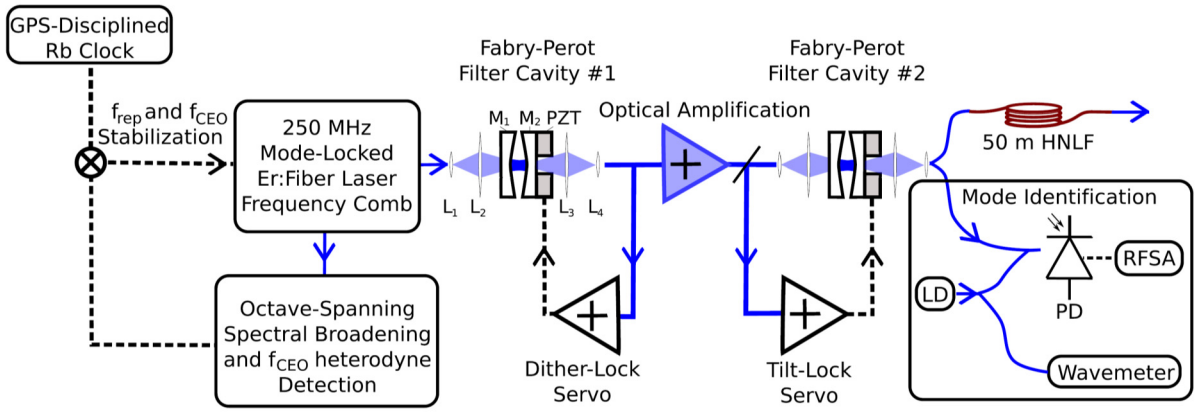

Figure 15 Schematic of the laser frequency comb. The 250 MHz passively mode-locked erbium fiber laser is stabilized by locking the repetition rate f_{rep} and carrier-envelope offset frequency f_{ceo} to a global-positioning system (GPS)-disciplined rubidium clock. Light from the mode-locked laser is sent through the Fabry-Perot cavity (mirrors M_1 and M_2) with mode-matching between the cavity and single-mode fiber provided by lenses L_1–L_4. The transmitted light is amplified to 1.4 W, then sent through a second, identical Fabry-Perot cavity. The pulse is re-compressed and spectral broadening is achieved using 50 m of highly-nonlinear fiber (HNLF). Mode identification is achieved by measuring the beat of a single comb mode with a wavemeter-calibrated CW laser diode (LD) using a photodiode (PD) and radio-frequency spectrum analyzer (RFSA).

pigtailed aspheric collimators and two additional lenses for mode-matching, allowing a fiber-to-fiber coupling efficiency of ~ 20%. Generation of the 25 GHz calibration spectrum proceeds as in Ref. [67] and is illustrated in Figure 15. The two identical filter cavities are used to select a subset of modes with spacing of 25 GHz, and cascaded optical amplifiers placed between the cavities provide the gain required to attain the 300 mW of power required for nonlinear broadening of the LFC. After filtering and amplification, the 25 GHz comb light is compressed to a ~ 300 fs pulse using dispersion compensating fiber and launched into highly nonlinear fiber (HNLF) [62]. A number of different HNLFs were tested, and spectra recorded at different input powers are reported in Figure 16. The best results were achieved by use of 50 m of the "HNLF-2" fiber for generation of the calibration spectrum. Finally, to resolve the ambiguity in the mode-number of the filtered comb modes, a heterodyne measurement between a single mode of the filtered comb and a wavemeter-calibrated continuous-wave (CW) laser is performed.

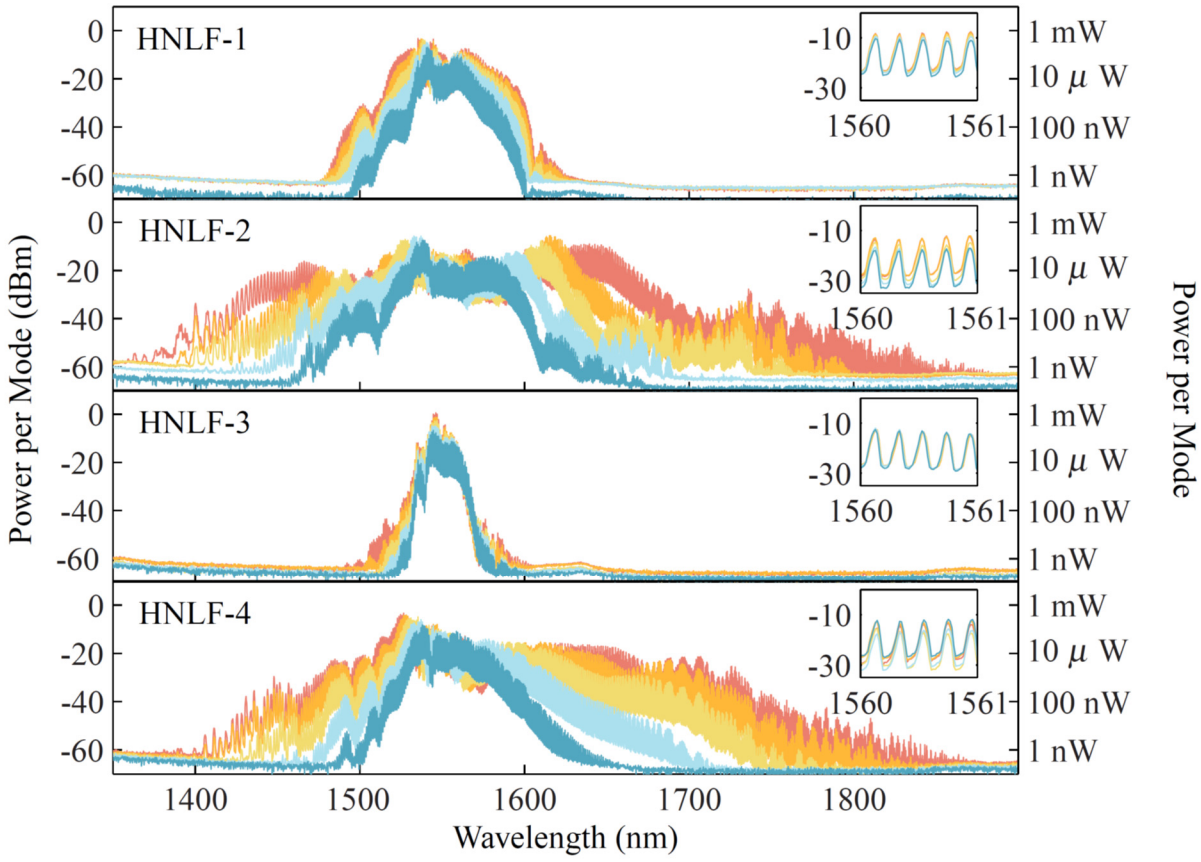

Figure 16 Supercontinuum spectra generated with 25 GHz pulses in a variety of highly nonlinear optical fibers (HNLFs) at different launch powers. Insets: zoom-in between 1560 nm and 1561 nm, showing the resolved 25 GHz-spaced comb modes. The dynamic range of the measurement, and any apparent asymmetry in the lines, is limited by the optical spectrum analyzer used for the measurement. At the input of the fiber, the pulses have a duration of 300 fs, as determined by nonlinear autocorrelation. The energy per pulse is varied from 3 pJ (narrow spectra, foreground) to 8 pJ (broad spectra, background), corresponding to 80 mW–200 mW average power. The lengths and dispersion parameters of the fibers are HNLF-1: 100 m, -0.14 ps/nm/km at 1550 nm, HNLF-2: 50 m, +0.3 ps/nm/km at 1550 nm, HNLF-3: 48 m, +6.7 ps/nm/km at 1550 nm, HNLF-4: 100 m, +2.5 ps/nm/km at 1550 nm.

Characterization of 25 GHz Comb

Optical heterodyne measurement of 25 GHz comb

After nonlinear broadening, the comb spans from 1450 nm to 1700 nm, providing a calibration spectrum with an extremely high signal-to-noise ratio suitable for an astronomical spectrograph covering the H-band. The frequency of each mode of the filtered 25 GHz comb is known with an accuracy of 10^{-10}, limited by the GPS-disciplined rubidium standard. While this corresponds to ~ 3 cm/s uncertainty, the actual achievable precision is in most cases limited by other sources. Here we discuss the most significant sources of uncertainty related to our method of comb generation. In particular, we extend the characterization of the LFC line-shape, absolute frequency accuracy, and side-mode suppression from Ref. [67] with optical heterodyne measurements to assess the uncertainties that arise from spurious and unsuppressed side-modes and technical ambiguities in servo control.

One of the chief sources of uncertainty is a result of the use of nonlinear spectral broadening in conjunction with a Fabry-Perot cavity-filtered laser frequency comb. Each filter cavity suppresses the two nearest-neighbor 250 MHz comb modes on either side of the 25 GHz comb modes by 10^3 per cavity, and while the use of two cavities increases the suppression to 10^6, four-wave mixing processes taking place in the optical amplifiers and nonlinear fibers transfer power back into the suppressed modes. Depending upon the pulse and fiber parameters during the nonlinear broadening process, the parametric gain has the potential to be so large for the suppressed modes to have an amplitude comparable to and even larger than the nominal 25 GHz comb mode [67, 14]. It is also possible that, in the cavity filtering and broadening processes, a spurious 250 MHz comb mode, for example a mode lying on a higher-order transverse mode of the filter cavity [67, 83, 78], could see amplification and lead to a skewing of the apparent line center.

To verify that the comb's optical spectrum is free of spurious modes, a heterodyne measurement continuously covering 1610 nm to 1620 nm was made by tuning a CW laser across the 25 GHz LFC. Because the amplitudes of the side-modes are determined by the action of nonlinear processes, and not by the transfer function of the filter cavities, a measurement of the filter cavity dispersion [48] is not sufficient and heterodyne measurements after nonlinear broadening are required. The results of this measurement, derived from 90 individual radio-frequency spectra, are shown in Figure 18. This measurement demonstrates that no spurious peaks exist between the 25 GHz comb modes above the -55 dB noise floor between 1610 nm and 1620 nm. Because the spurious effects of higher-order transverse modes are expected to occur across the comb, and

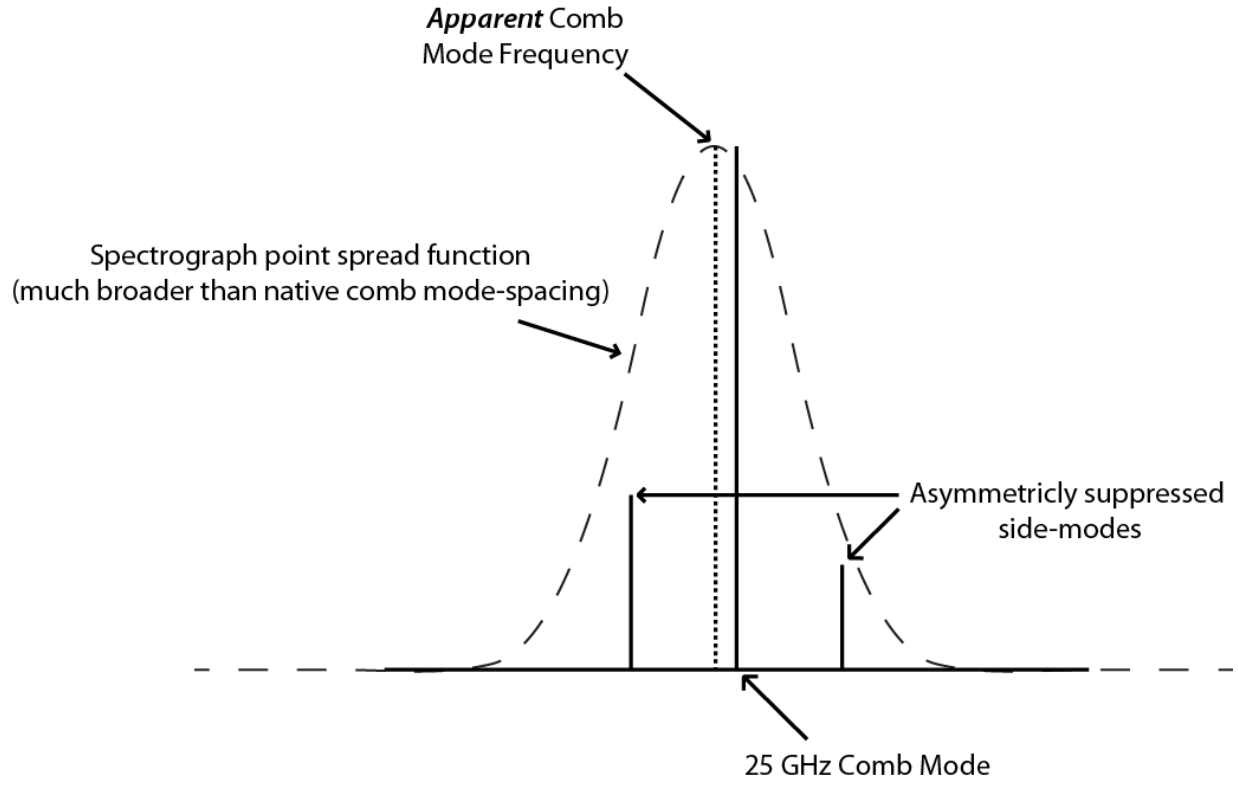

Figure 17 Mechanism for translation of side-mode asymmetry to spectrograph calibration error. Because the spectrograph cannot resolve the individual modes, the presence of asymmetric, incompletely suppressed modes moves the apparent center of the mode.

spurious modes due to four-wave mixing processes are expected to most strongly present far from the center of the filtered LFC, this measurement assures us that the spurious modes observed by the Pathfinder spectrograph are negligible or well-understood.

While there are no large spurious modes in the 25 GHz spectrum, incompletely suppressed side-modes are present in the spectrum [11, 83, 67, 14, 48]. The Pathfinder spectrograph's point spread function has a full-width at half maximum of ~ 3 GHz, and as a result the apparent line center is the weighted average of the main comb mode and the nearest-neighbor side modes,

$$f_{\text{apparent}} = \frac{\sum_{-N}^{N} A_i \left(f_{\text{ceo}} + i \times f_{\text{rep}} \right)}{\sum_{-N}^{N} A_i} \tag{5.3}$$

where A_i are the relative powers of the comb modes, f_0 is the optical frequency of the central mode, and N is 50; the fractional shift of the line center is $(f_{ceo} - f_{apparent})/f_0$. For side-mode levels measured, only the central mode and two nearest-neighbor $\pm f_{\text{rep}}$ modes significantly affect the apparent line center. To measure the size of this shift in the calibration spectrum, heterodyne measurements with a CW laser were made at 10 nm intervals, from 1400 nm to 1620 nm, recording the relative side-mode amplitudes at each point. The results of this measurement, shown in Figure 19, demonstrate that, near 1540 nm, the side-mode suppression is highest at > 50 dB, and that moving to both higher and lower wavelengths sees a significant decrease in suppression. Nonetheless, in the spectral bands of interest, the apparent spectral shift is less than 10^{-10} fractionally.

One final source of uncertainty arises from the technical issue of locking the filter cavities to transmit a particular set of 250 MHz modes. Because of cavity dispersion, only a few such sets are efficiently transmitted, but there is freedom to choose among these sets of modes. By measuring the side-mode suppression of each set of transmitted modes (see Figure 20) it is confirmed that equal side-mode suppression, and thus accuracy, is obtained regardless of which set of transmitted modes is chosen.

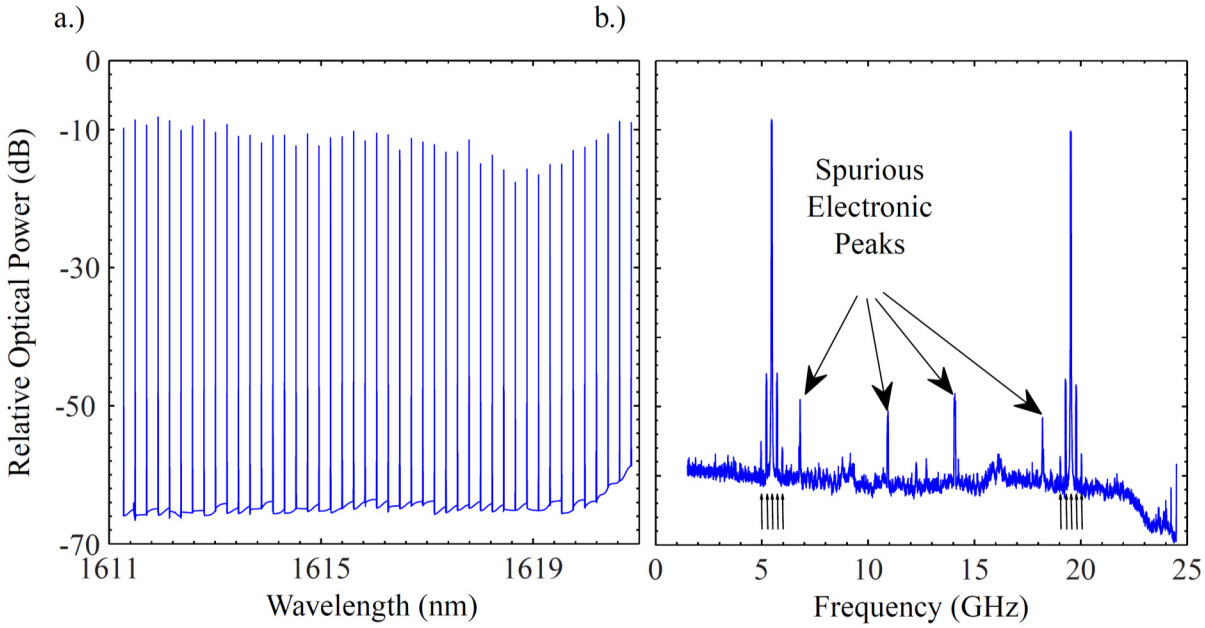

Figure 18 a.) Optical spectrum obtained by analyzing 45 individual heterodyne measurements of the calibration spectrum with a tunable CW laser. The resolution-bandwidth of the RFSA was 300 kHz, and for each measurement "max-hold" averaging for several tens of sweeps was employed. Within the 50 dB - 55 dB dynamic range of this measurement, no spurious optical modes between comb teeth were detected other than nearest-neighbor modes offset by 250 MHz and 500 MHz. The noise floor indicated is an estimate, defined by the mode of the detected RF power from each measurement from 1-25 GHz. b.) Radio-frequency spectrum from heterodyne of LFC with CW laser tuned near 1621 nm. Peaks determined to be in the optical spectrum are marked from below by arrows.

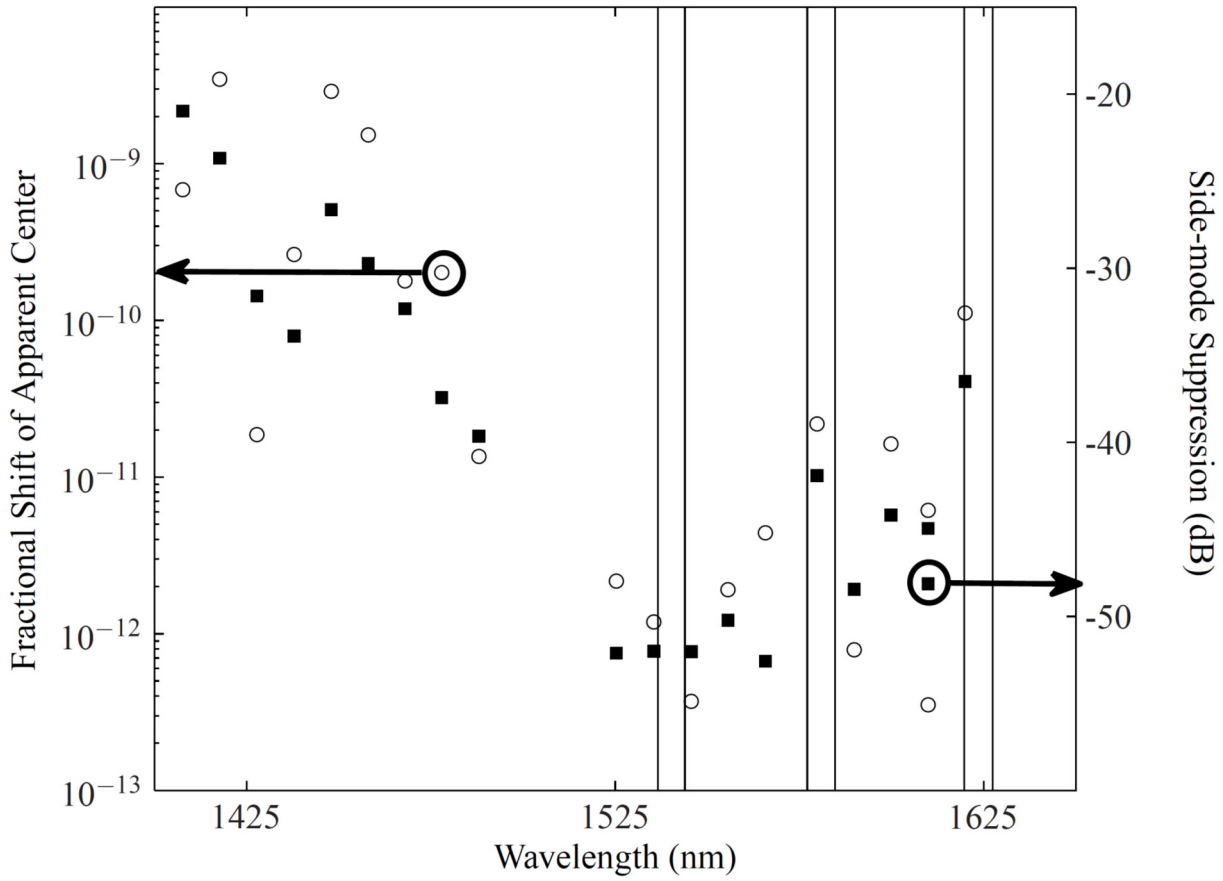

Figure 19 Measured apparent shifts (circles) of 25 GHz comb mode centers and side-mode suppression (squares), derived from optical heterodyne measurements. Data were taken by measuring the heterodyne beat of a tunable CW laser with single modes of broadened comb from 1400 nm to 1625 nm and apparent shifts were calculated by using the weighted average of the comb mode and nearest-neighbor side-modes. Enclosed in rectangles are the three wavelength regions observed by the Pathfinder spectrograph. Data were taken with CW laser tuned to both the high- and low-frequency sides of each mode, and the side mode amplitudes from the two measurements were averaged. Note that the line-center shift, which depends upon not only the degree of side-mode suppression but also on asymmetry, mirrors the side-mode suppression.

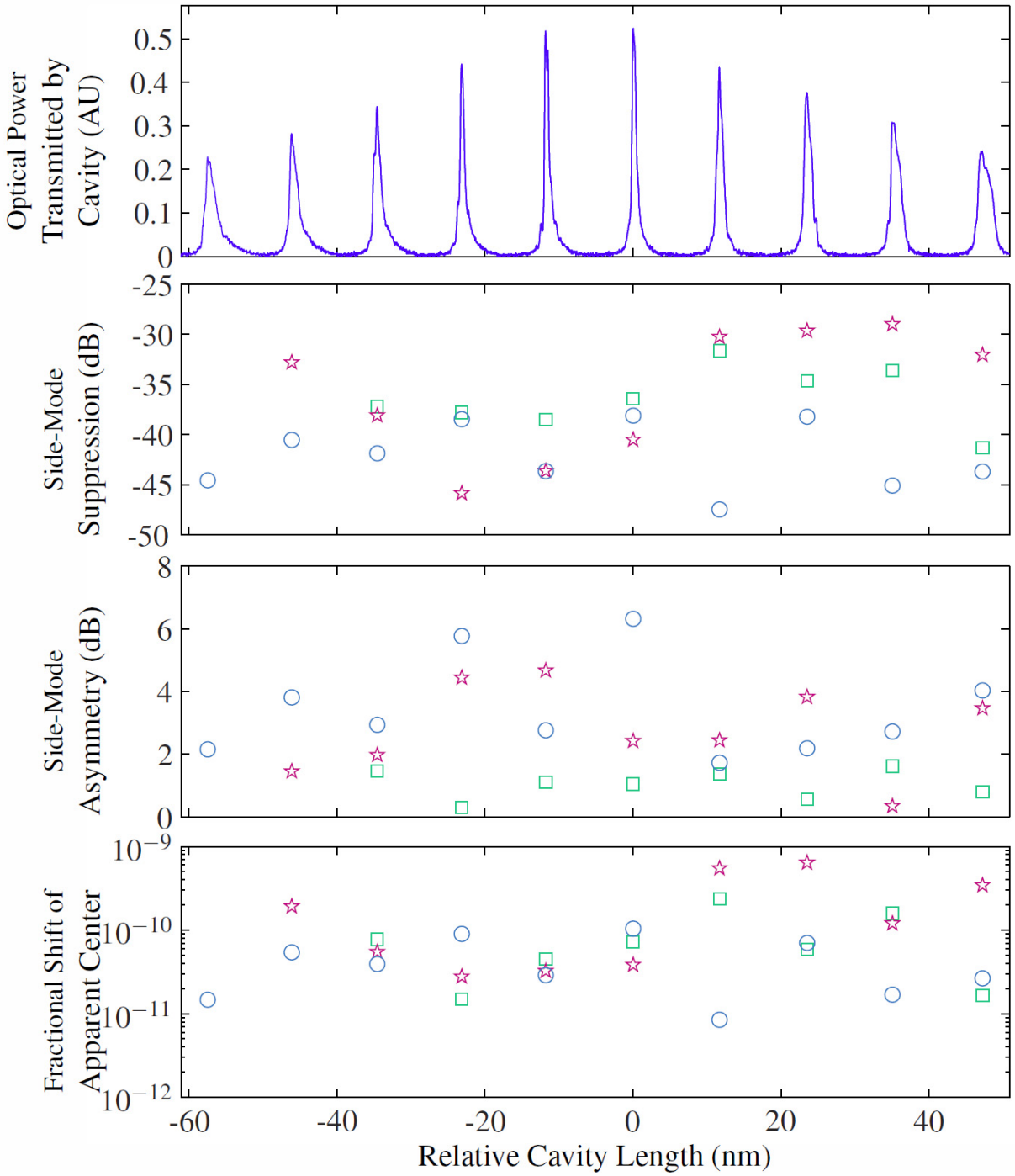

Figure 20 Measured effect of the lock point of the first filter cavity on the supercontinuum after the HNLF. The first filter cavity was locked to 10 different transmission peaks (top) and the side-modes were measured at 1439 nm (stars), 1566 nm (circles), and 1625 nm (squares.) The measurement shows that the choice of lock point has no strong influence on the side-mode suppression, asymmetry, or shift of line center. The uncertainty in these measurements is ± 2 dB, due to amplitude noise of the frequency comb and frequency noise of the CW laser.

Measurement of Frequency Comb Using NIST 2 meter FTS

Moving the frequency comb out of the NIST Boulder laboratories is a major undertaking. The optics breadboard, vibration isolation legs, electronics rack, and major supporting instrumentation are all packed into shipping containers and transported via a chartered semi-truck. The comb system must then be unpacked and made operational, and at a remote observatory location obtaining new or replacement parts requires too much time to be practical. Because of these risks, before attempting to use the comb for astronomical observations we undertook a dry-run of the comb calibrator at the NIST labs in Gaithersburg, Maryland. There was low risk involved, as no telescope time was used and obtaining spare parts was simple, and the visit provided the opportunity to measure the comb using the NIST 2 meter Fourier transform spectrograph (FTS) – the same instrument used for reference measurements of other astronomical calibration sources, both absorption cells

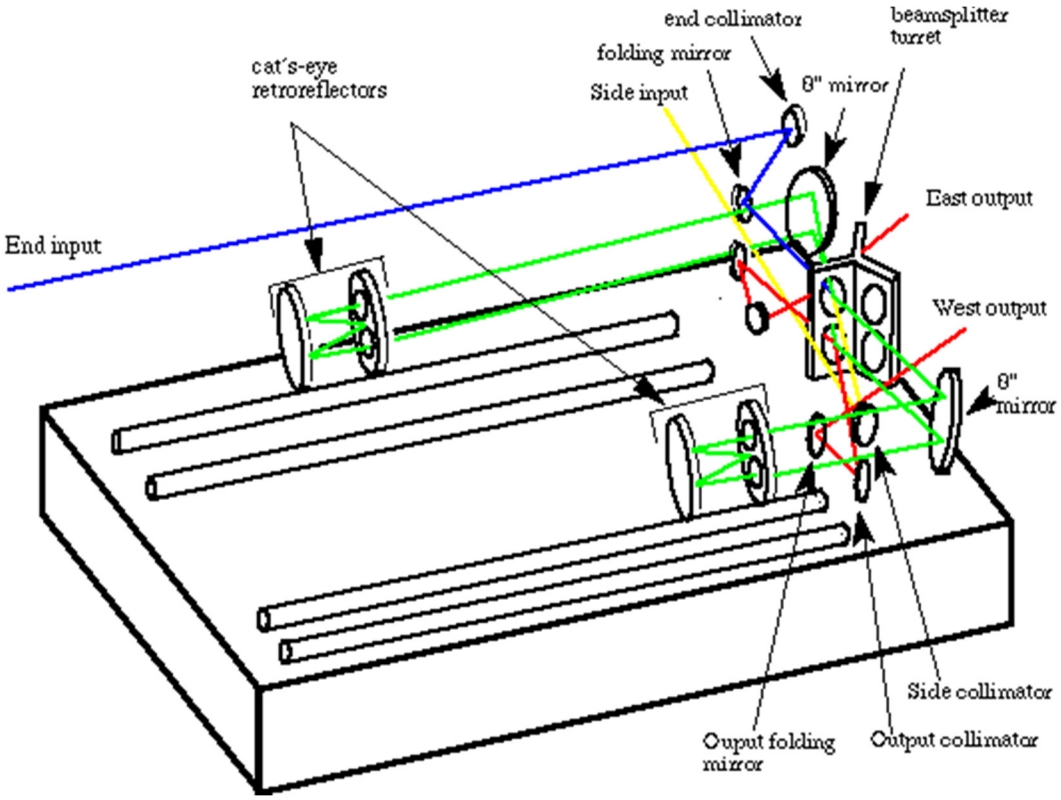

Figure 21 NIST 2 meter FTS optical layout. Courtesy NIST Atomic Spectroscopy Group.

and lamps. During this measurement, the frequency comb was configured such that the repetition frequency was 12.5 GHz, as described in Ref. [67].

Fourier transform spectroscopy utilizes a carefully calibrated Michelson interferometer to measure the optical spectrum of a source [19]. If the source spectrum has intensity distribution *I(σ)*, where σ is the wavenumber [cm^{-1}], at path length difference *x* the intensity detected at the balanced FTS output is simply the sum of the interference of every color:

$$I(x) = \int_0^\infty I(\sigma)\cos\big(2\pi\sigma x\big)d\sigma. \tag{5.4}$$

The FTS scans the path length difference *x* while recording the spectrogram *I(x)*. For accurate measurement of the path length difference the fringes from a stabilized CW laser are simultaneously recorded, with the optical fringes used to measure *x* with nm-level precision. Once the interferogram is measured, the optical spectrum is retrieved by Fourier transform:

$$I(\sigma) = \int_{-L}^{L} I(x)\cos(2\pi\sigma x)dx. \tag{5.5}$$

The spectrometer's response to a monochromatic source, with symmetrized spectrum

$$I(\sigma) = \frac{1}{2}I_0\big(\delta(\sigma-\sigma_0)+\delta(\sigma+\sigma_0)\big), \tag{5.6}$$

is:

$$\begin{aligned} I_{FTS}(\sigma) &= \int_{-L}^{L} I_0\cos(2\pi\sigma_0 x)\cos(2\pi\sigma x)dx, \\ &= L\,\mathrm{sinc}\big(2\pi L\big(\sigma-\sigma_0\big)\big) + L\,\mathrm{sinc}\big(2\pi L\big(\sigma+\sigma_0\big)\big). \end{aligned} \tag{5.7}$$

The resolution of the FTS is thus set by the maximum path length difference *L*, and the standard formula for the FTS resolution is

(5.8) $$\delta\sigma = \frac{1}{2}\frac{1}{L}.$$

Thus the NIST 2-meter FTS has resolution of 0.0025 cm^{-1}. It is important to remember, however, that the sinc function is extremely broad, falling off as 1/x and shown in Figure 22. This is key to the application of the FTS to measurement of a frequency comb; while the 2 meter FTS provides resolution of 0.0025 cm^{-1}, or 75 MHz, when looking for the side-modes of a filtered frequency comb the fact that a bright mode of the filtered comb is diminished by only one order of magnitude at an offset of f_{rep} (250 MHz) makes the direct measurement of even weakly suppressed modes impossible.

To measure the frequency comb using the NIST FTS, comb light was delivered to a 2 inch diameter PTFE integrating sphere by a single-mode optical fiber. The spectrometer recorded the interferogram of the comb, and to build signal-to-noise multiple scans were made and co-added. The resulting interferogram and spectrum are shown in Figure 23. Due to the breadth of the comb modes, and the slight uncertainty in the FTS line-shape function, it is not possible to resolve the effects of nearest-neighbor side modes using these spectrograms.

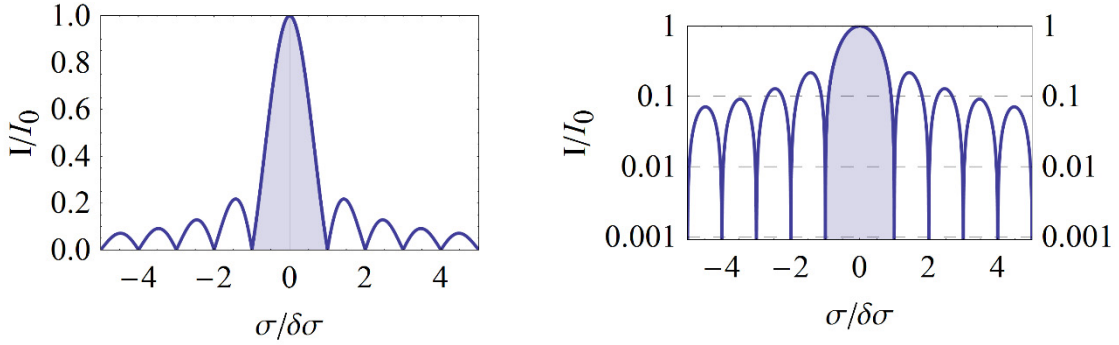

Figure 22 Graph of the absolute value of the sinc(x) function on both linear and logarithmic scales. The shaded region shows the signal within one resolution element ±δσ. A significant property of the FTS is the strong over-spilling of the signal from a strong feature.

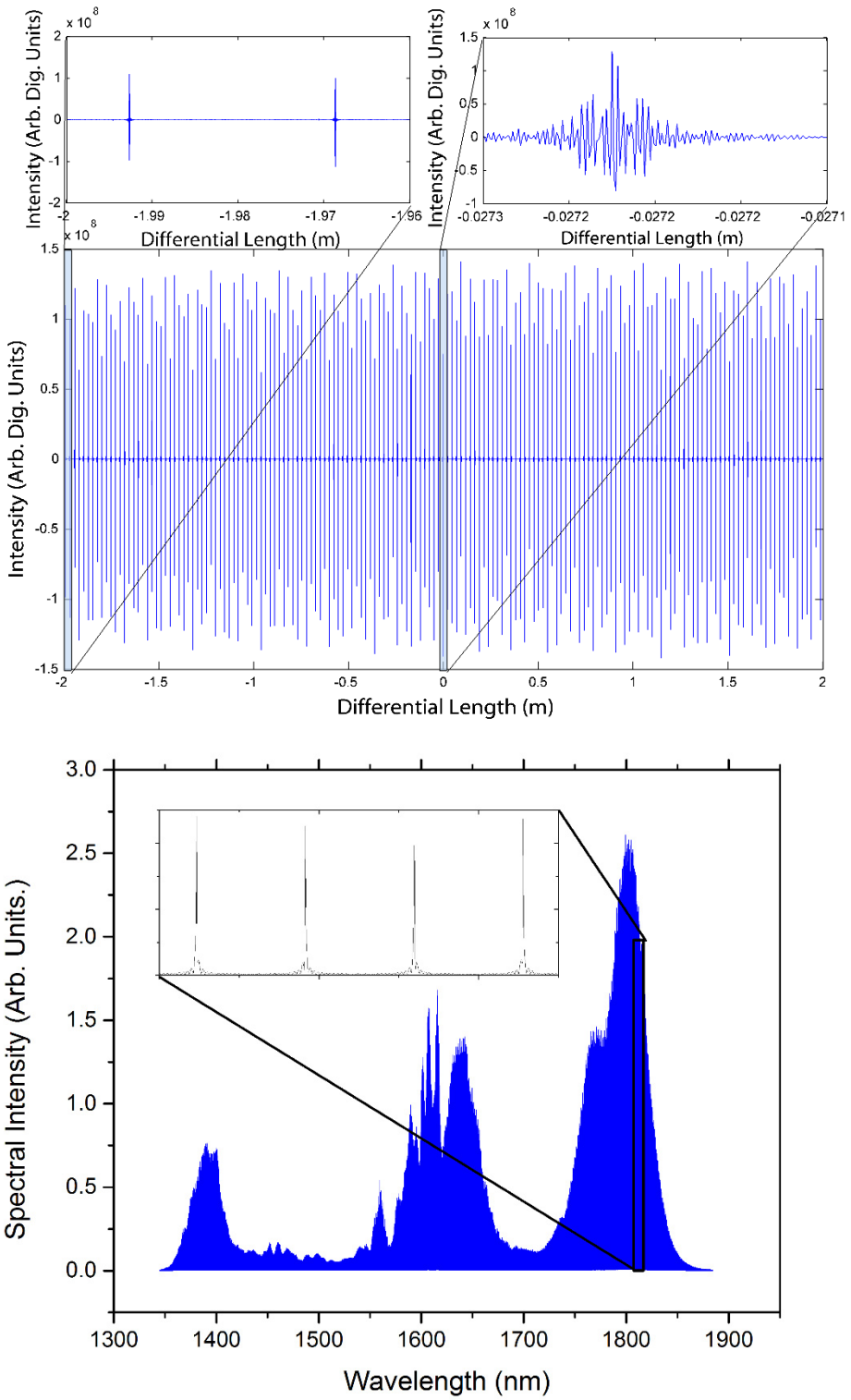

Figure 23 Top: Interferogram of frequency comb measured by FTS. Unlike classical light sources, the frequency comb maintains coherence across the full 2 meter path length difference. Bottom: Spectrum as determined by FTS. Note that, because of the lack of apodization and the sinc-function instrument response, each bright comb mode extends far beyond the 75 MHz FTS resolution. This precludes the use of this measurement technique for the determination of side-mode levels.

While the side-mode levels were undetectable in the measurement, the FTS data were able to provide information about both the comb performance and the behavior of the FTS. One significant result is that the high-repetition rate comb is fully coherent at all wavelengths, including the light at wavelengths longer than 1800 nm. Because these wavelengths were unmeasurable in our Boulder laboratory with our optical spectrum analyzer, the data here is the sole confirmation of the comb-structure above 1700 nm. A second result was derived from fitting each comb mode's wavenumber and intensity using the instrument-response function, itself derived from the interferogram of a single-frequency laser. The comb mode intensities are plotted in Figure 24 (a). Using the mode positions as determined by the fit, the linearity of the FTS can also be characterized. The comb mode frequencies were fit to a line. The residuals, shown in Figure 24 (b), show that there is no remaining

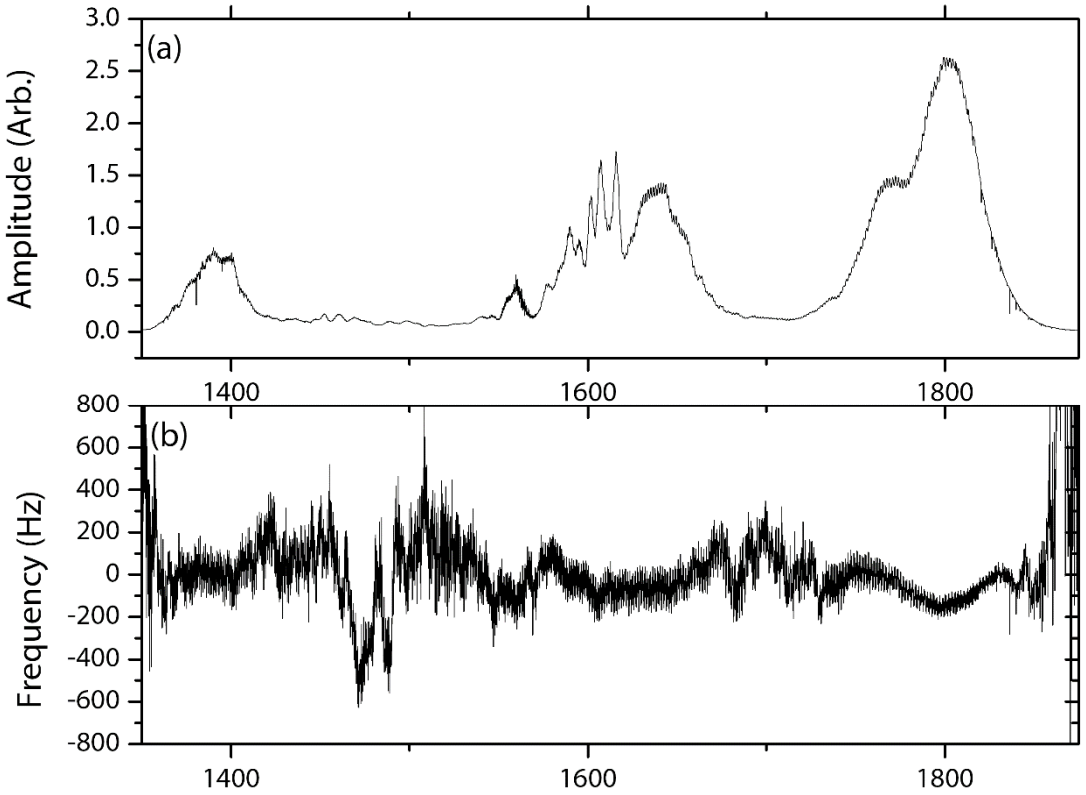

Figure 24 (a) Measured frequencies and intensities of each mode of the 12.5 GHz frequency comb. The individual modes are too closely spaced to be resolved here (there are 5100 in all.) (b) Residuals from fit of mode frequencies to straight line (frequency comb equation). The actual frequency is 12.500 GHz, while the FTS measurement is 12.5077 GHz.

structure and that the FTS wavenumber axis is linear to within several hundred Hz across the full 1350—1850 nm wavelength region.

Calibration of the Pathfinder spectrograph

After testing in the NIST laboratories in Boulder, Colorado, the laser frequency comb-based calibrator was transported to the McDonald Observatory in southwest Texas where it was used to calibrate the Pathfinder spectrograph at the Hobby-Eberly telescope (HET), pictured in Figure 25. The Pathfinder spectrograph is a prototype fiber-fed near-IR spectrograph with resolution λ/Δλ= 50,000 operating from 1-1.8 μm [70, 69]. The spectrograph is assembled on an optical breadboard inside a passively stable room-temperature enclosure with a liquid nitrogen cooled HgCdTe detector array having 1024 × 1024 pixels on an 18.5 μm pitch (HAWAII-1 HgCdTe Astronomical Wide Area Infrared Imager.) To reduce the thermal background from the warm optics, cascaded cold edge-pass filters inside the detector dewar are used to reject out-of-band radiation. Three 300 μm core multimode fibers, potted in epoxy and polished one atop the other, feed the spectrograph. One fiber carries light from the telescope, while the other two are used for calibration. The spectrograph's resolution is set by use of a 100 μm entrance slit, cross-dispersed and imaged into 4.4 pixels of the focal-plane array. For the demonstration of the LFC calibrator, the angles of the spectrograph gratings were adjusted away

Figure 25 Left: Hobby-Eberly telescope at the McDonald Observatory at Ft. Davis TX. Right: Photograph of the Penn State University Pathfinder spectrograph.

from their designed Y-band positions for operation in the H-band. In this configuration, fractions of three echelle orders were imaged onto the focal-plane array, covering a total of 22.5 nm of spectral bandwidth between 1537 nm and 1627 nm. The drift of the spectrograph was measured during the run using both uranium-neon lamp lines and the LFC, and is typically hundreds of meters per second per day. Because the telescope and calibration fibers closely track each other, this drift has been shown to limit RV precision only at levels below 3 m/s [69].

The laser frequency comb, which consists of a 19-inch electronics rack and a 2.5 ft × 4 ft optical breadboard floating on vibration-isolating air legs, was set up in the spectrograph room of the HET, adjacent to the thermal and acoustic enclosure housing Pathfinder. Calibration light was coupled from the single-mode fiber output of the LFC into a 300 mm core fiber using a 4 inch diameter PTFE (Teflon) integrating sphere with an internal baffle. Although the power loss through the integrating sphere was roughly a factor of 106, there was sufficient light available for the spectrograph. The 300 mm fiber output from the integrating sphere was then sent to the Pathfinder calibration bench, where an arrangement of beamsplitters allowed for the illumination of the spectrograph's two 300 mm calibration fibers with combinations of the LFC and hollow-cathode U/Ne and Th/Ar lamps.

Using the ability to illuminate the two calibration fibers of spectrograph with either frequency comb light or a hollow cathode U/Ne lamp, a series of measurements were made. In one experiment, frequency comb light was sent down each calibration fiber, which provided a measure of the difference in dispersion between the fibers. These data are shown in Figure 28, and demonstrate the few-picometer difference in dispersion solutions. This is expected, and is a reminder of the difficulties in performing a truly absolute calibration. In addition, an *in situ* measurement of the U/Ne lamp's spectrum from 1454 nm to 1638 nm was recorded, using the LFC and Pathfinder spectrograph, shown in Figure 26. The data for this measurement were collected in only a few hours, demonstrating the strength of the LFC as a calibration tool for astronomical spectroscopy. The results of this measurement were used to construct an atlas of spectral lines in the U/Ne spectrum suitable

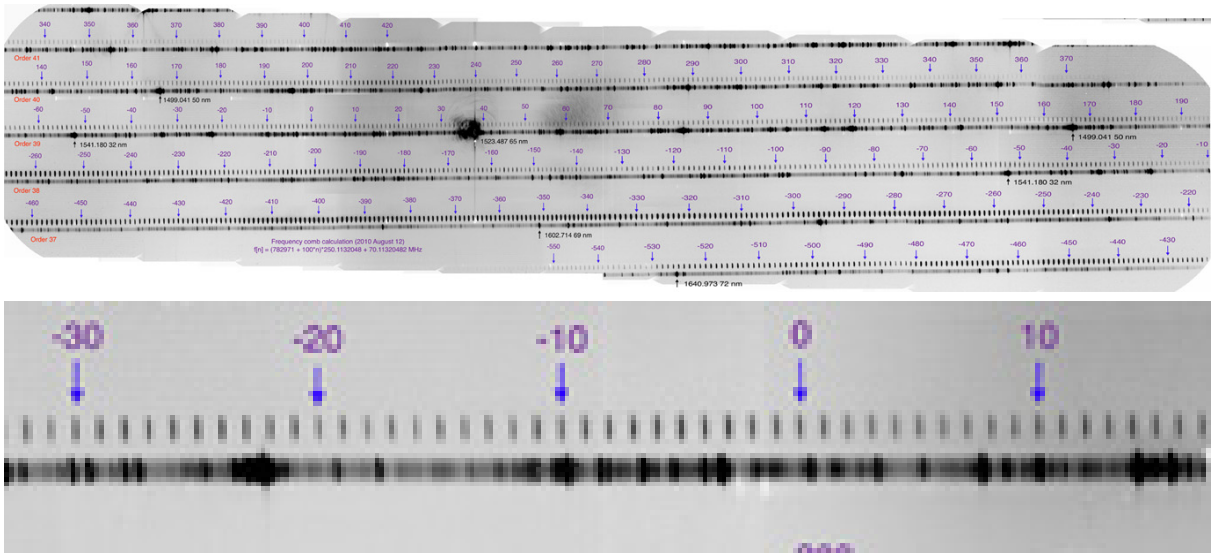

Figure 26 Spectra of uranium-neon hollow cathode lamp and laser frequency comb as detected by Pathfinder spectrograph.

for calibration of astronomical spectrographs and published with our collaborators at Penn State University [73].

An additional configuration allowed for the coupling of comb light into a multimode fiber routed to a position near the prime focus of the HET, where it could illuminate a screen used for flat-field calibration of the science fiber. The high power of the LFC combined with the various configurations of illumination of the

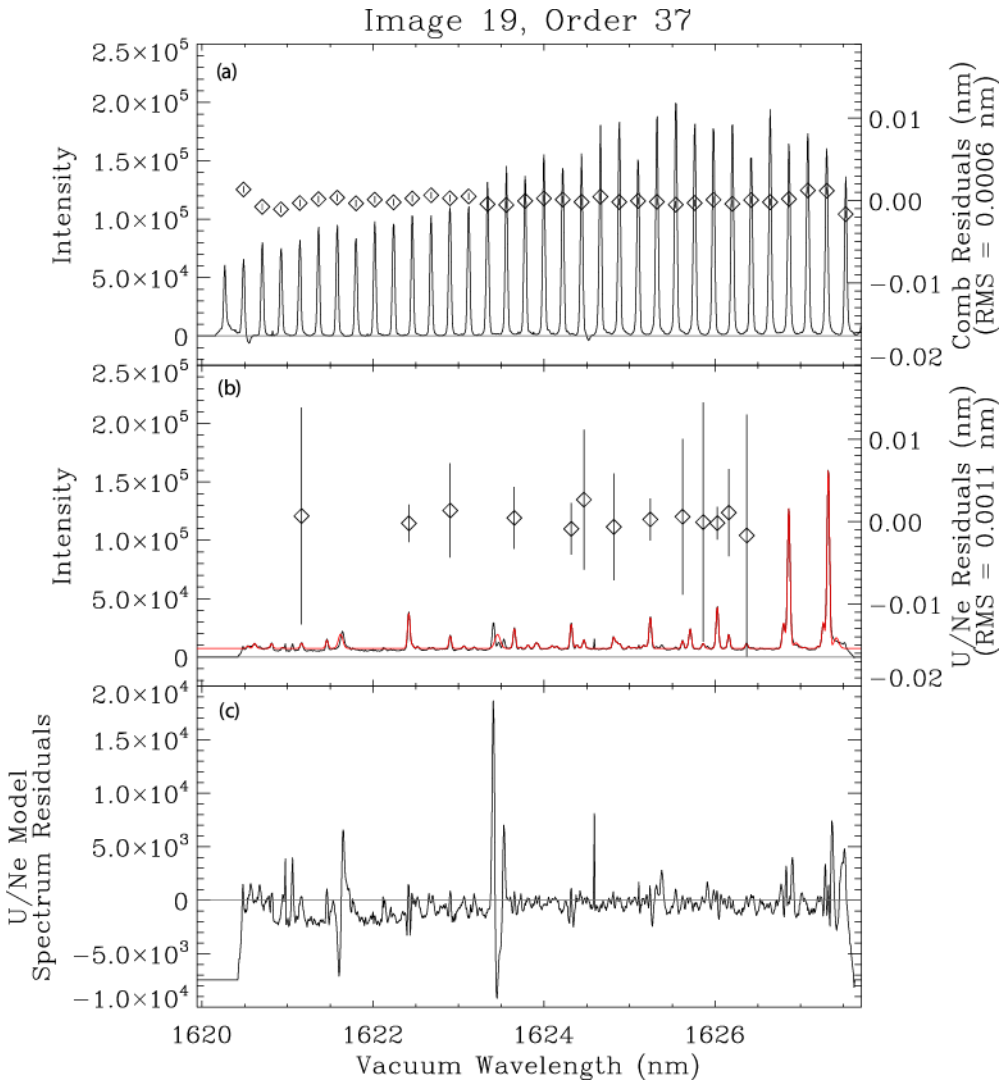

Figure 27 Processed data for one echelle order for one portion of the uranium-neon lamp. (a) Extracted laser frequency-comb spectrum. (b)Extracted hollow-cathode lamp. (c) Residual between hollow cathode data and model spectrum. Figure from [73].

three spectrograph fibers provided a means of cross-checking the quality of spectra obtained using the different spectrograph fibers. While not studied in detail in these preliminary experiments, we envision taking advantage

of this flexibility in the future to examine and reduce systematic effects related to time-varying pointing errors, non-uniform mode excitation (modal noise), and the speckle-type pattern from the coherent LFC calibrator.

In the present experiments it was seen that modal noise [6, 26], which is the changing illumination of the detector resulting from the interference of the finite number of excited optical modes in the 300 mm fibers,

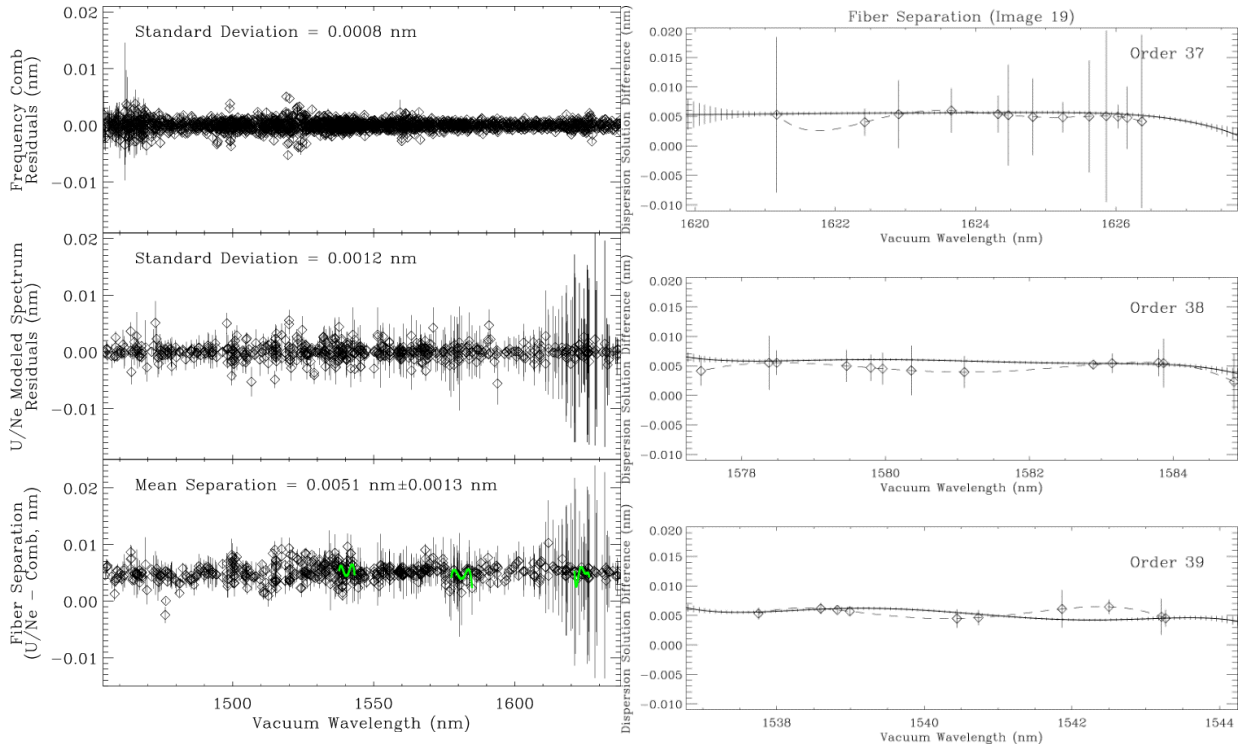

Figure 28 Left: Precision of frequency comb and uranium neon lamp calibration. Left top: Residuals of each comb mode frequency from low-order polynomial. Left middle: Residuals of uranium-neon lamp from fit of bright, isolated features in lamp spectrum. Left bottom: Difference between comb and lamp dispersion solutions. The areas marked in green are enlarged and shown to the right. Right: dispersion solutions for frequency comb –frequency comb (solid) and frequency comb-uranium neon lamp (dashed) in each of three echelle orders. Vertical bars show error. Figures from Ref. [73].

limited the attainable RV precision to ~ 10 m/s. To mitigate the effect of modal noise, we employed the integrating sphere for coupling the single-mode laser light into the 300 mm optical fiber and a commercial paint mixer for active fiber agitation. In spite of these efforts, modal noise still dominated all other limitations on RV precision, such as point-spread function changes due to the pupil illumination of the telescope, detector

response, the signal-to-noise ratio, and the number of stellar lines. More details about the impact of modal noise on measurements with the LFC are presented in section 5.1 of Ref. [73]. The particular issue of coupling single spatial mode frequency comb light to the multimode fibers and spectrograph is a new aspect of this problem which will require further investigation.

The frequency comb was operated together with the Pathfinder instrument at the HET over a two-week period. Over this time, the calibration spectrum had a constant envelope and power output, and the filter cavities could be locked to transmit the same 25 GHz subset of modes. The long-term stability of the comb frequencies was determined by the Rb clock, which was measured at NIST both before and after the experiment to have fractional absolute accuracy of 1×10^{-10}.During the observation run, 648 spectra were recorded with 5 minute integration times, of which 91 were of astronomical objects, including the stellar targets HD16873, Sigma Draconis, Vega, Eta Cassiopeae, and Upsilon Andromeda. Useful spectra were obtained on three nights with good weather and seeing, and three nights with variable conditions. During these measurements, the comb operated without fault, although adjustments to the servos were required before each night. A typical spectral image for HD16873 is shown in Figure 29(c) and extracted spectra are presented in Figure 29(d). As seen in the figures, the comb provides a uniform grid of calibration markers with high signal-to-noise for each echelle order. The simultaneously-recorded science spectra show both absorption features intrinsic to the stellar atmosphere as well as sharp telluric CO_2 lines from the earth's atmosphere. Radial velocities of the known stable star Eta Cassiopeae, obtained with the comb as the simultaneous reference to track instrument drift, are shown in Figure 30. The derived uncertainty of each 5 minute exposure was ~ 30 m/s, and typically 6-11 such exposures were acquired back-to-back. The scatter in the data about the mean for the back-to-back exposures was ~ 28 m/s, consistent with the uncertainty attributed to each exposure.

The dominant limitation on precision is again modal noise, and was seen to average down when the back-to-back exposures were combined. This indicates that the mode pattern is not static, but changes on a time-scale similar to the 5 minute exposure time. All of the data in Figure 30 are derived from the analysis of a single echelle order, and in spite of modal noise limitations show an H-band RV precision of ~ 10 m/s, a level competitive in the NIR (with an uncooled instrument testbed). These preliminary results are very encouraging

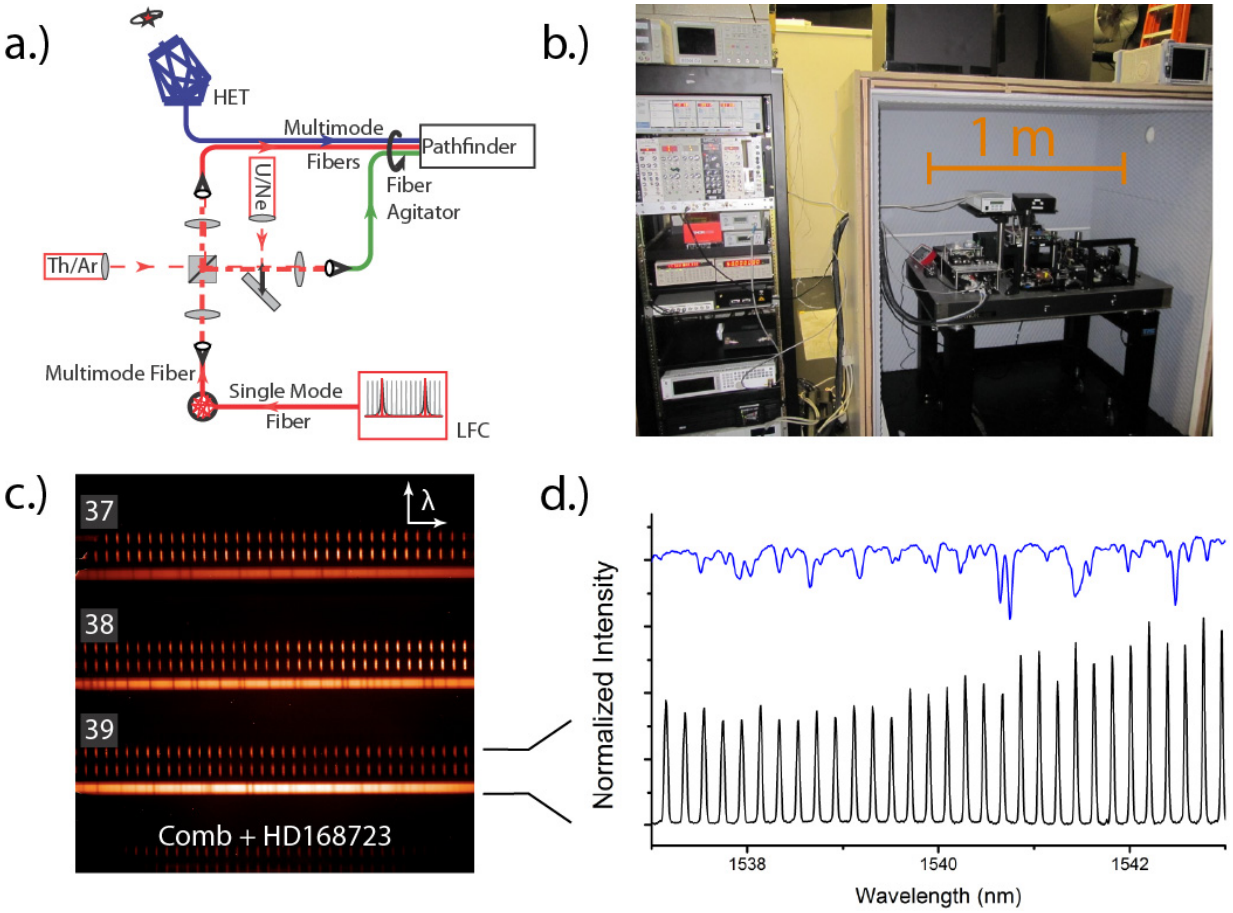

Figure 29 a.) Schematic of the coupling of light sources into Pathfinder spectrograph. Free space beam splitters direct the different calibration sources – LFC, U/Ne, and Th/Ar – into the two calibration fibers. A commercial paint shaker is used as a fiber agitator to mitigate modal noise from the multimode fibers. b.) A photograph of the laser frequency comb calibrator in the spectrograph room at the Hobby-Eberly telescope at the McDonald Observatory. The electronics rack, left, houses the laser drivers, electronics for servo loops, and other electronics. The optics breadboard, right, holds the mode-locked laser, f–2f interferometer, two filter cavities, and fiber-optic components. The entire optics breadboard is enclosed within a wood-foam acoustic enclosure. c.) Image from focal-plane array of Pathfinder spectrograph showing light from both the laser frequency comb and the star HD168723. Echelle orders 37, 38, and 39 are visible, with wavelengths of 1536.6 nm to 1543.9 nm, 1577.1 nm to 1584.6 nm , and 1619.7 nm to 1627.4 nm. d.) Line out showing the 25 GHz laser frequency comb over a single echelle order.

and motivate the further development and optimization of high-precision infrared frequency comb spectroscopy.

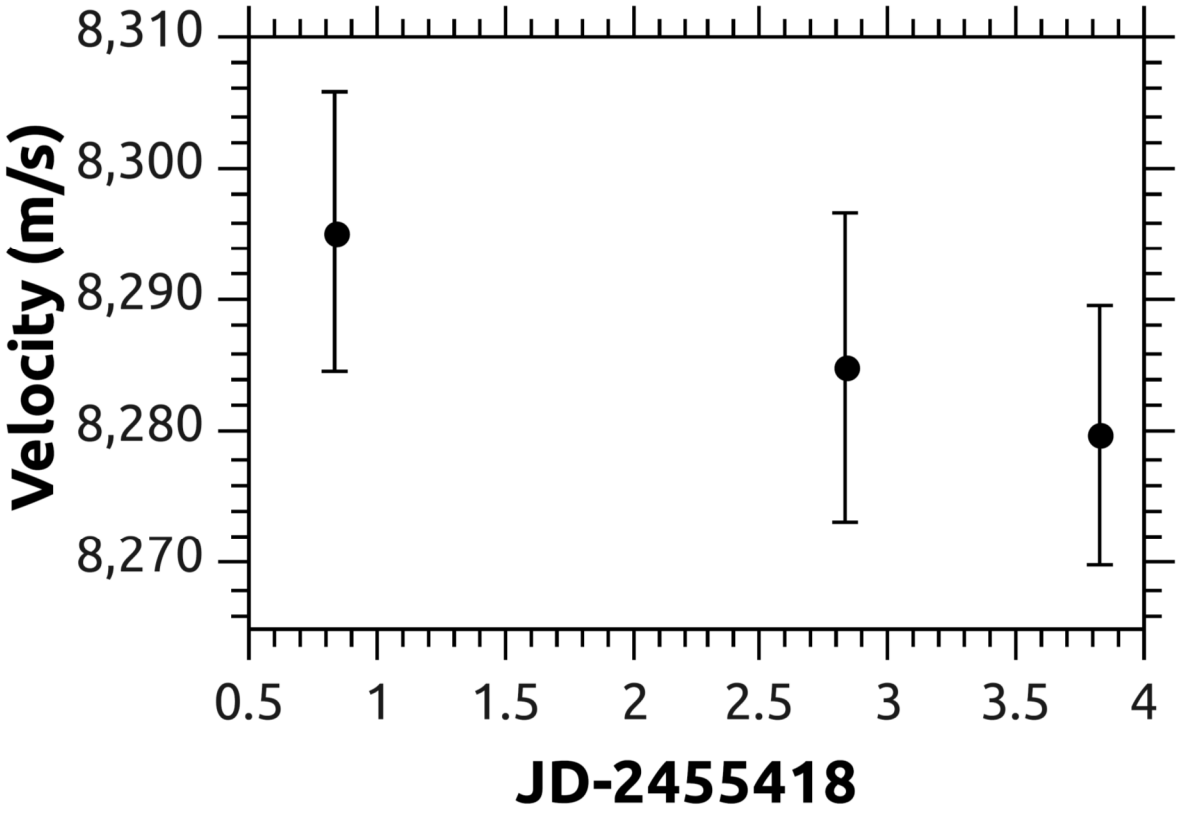

Figure 30 Radial Velocities were calculated from one order for the star Eta Cas using a binary mask cross-correlation similar to that described in Ref. [4], with the correlation mask generated from an NSO FTS atlas of the solar spectrum. We only included the deep stellar absorption lines, well separated from telluric features, as part of the correlation. This returns not only the relative velocity of Eta Cas for every night, but also the 'absolute velocity' of the star since the wavelength solution is referenced to the frequency comb, and the mask is referenced to the solar velocity. The 'absolute velocity' we measure is entirely consistent with the velocities for Eta Cas reported by Nidever et al. [61] (8314 m/s), exhibiting only a ~ 25 m/s difference even though different analysis techniques and entirely different stellar lines at very different wavelengths are used in both cases. The error bars shown in the figure are photon noise limited error bars, calculated using the theoretical prescription of Bouchy, Pepe, and Queloz [9].

Chapter 6

GENERATION OF A 1 MICRON COMB FROM THE ERBIUM LASER

Calibration of Next-Generation Spectrograph

The Pathfinder spectrograph used in Chapter 5 was a demonstration instrument, and was disassembled after the frequency comb calibration experiment. Pathfinder will be succeeded by a facility-class spectrograph, the Habitable-zone Planet Finder (HPF), which has been funded by an NSF Major Research Instrumentation grant and which will be installed permanently on the Hobby-Eberly telescope at the McDonald Observatory. Whereas the University of Florida FIRST spectrograph proposes to observe in the H band (1450—1700 nm), the HPF will observe in the Z, Y, and J bands which span 800—1320 nm. These shorter wavelength bands together are much broader than the H band alone, and the Y band (980-1110 nm) in particular has the fewest telluric lines and the largest number of useful lines for M stars. The HPF aims to achieve radial velocity precision of better than 3 m s^{-1}, making it the premier precision near-IR spectrograph in the US. Reaching this goal will require both a good understanding of systematic errors in the spectrograph, as well as a precision on-sky calibration standard.

A laser frequency comb system based upon either a mode-locked erbium or ytterbium fiber laser can provide such a calibrator. While at first glance the choice of an ytterbium laser that emits a spectrum centered at ~1050 nm seems clear, there are several compelling reasons to base a system on an erbium laser. The efforts in generating an erbium comb for the H band provided both a very stable, fully frequency stabilized erbium

comb and a large knowledge base in erbium technology. A more fundamental motivation for choosing an erbium comb relates to the zero-dispersion wavelength of silica. Because erbium lasers operate at wavelength where silica is anomalously dispersive and the fact that the waveguide dispersion induced by shrinking the mode size in a fiber is normal, it is possible to fabricate solid fibers with anomalous and normal dispersion. This permits the generation of the octave-spanning supercontinuum spectrum required for frequency-comb stabilization with a fully-spliced, alignment-free device, and as a result, an erbium comb can run essentially indefinitely and is relatively immune to misalignment.

As part of the collaboration between CU/NIST and the astronomical spectroscopy group at Penn State University, we have worked to develop a laser frequency comb system for permanent installation at the observatory for use as a primary calibration mode for the HPF. The next several chapters report on the technology which has been developed to support this effort, both extending the spectral coverage of the frequency comb to near 1 μm and also investigating alternative filtering schemes for a generating broad-bandwidth high repetition-rate comb.

First-generation system for coherent 1 micron light

Prior efforts have extended the spectral coverage of mode-locked erbium lasers by making use of second harmonic generation and nonlinear broadening [34] or a combination of large mode-area fibers and cascaded nonlinear fibers [60]. Here, we present a technique for generating a visible light frequency comb from a mode-locked erbium laser that is self-referenced and frequency-stabilized using established techniques. In prior experiments we noted that nonlinear broadening of an erbium comb shifts significant pulse energy to the 1 μm region, as can be seen in Figure 31. We make use of this, and demonstrate that these spectra, when amplified with a core-pumped Yb:fiber amplifier [41, 43, 42], produce a high-quality comb source at 1 μm. The amplifier output is then compressed to provide a 70 fs pulse, which is spectrally broadened to below 650 nm using

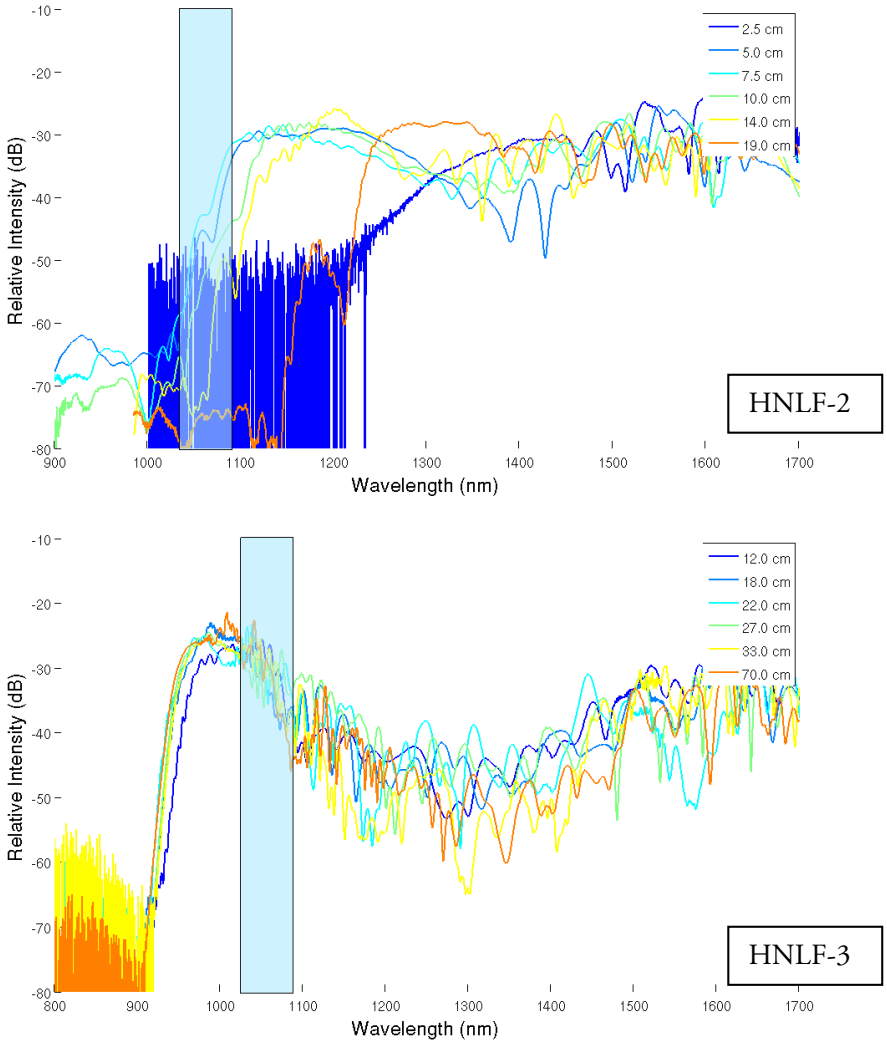

Figure 31 Optical supercontinuum spectra obtained launching sub-70 fs, 1.6 nJ pulses into Sumitomo fibers HNLF-2 (ZDW at 1550 nm) and HNLF-3 (ZDW at about 1400 nm). Shaded region indicates ytterbium gain bandwidth.

microstructured fiber. The combined output of the hybrid erbium-ytterbium system is a fully stabilized frequency comb spanning nearly two octaves of bandwidth from 650 nm to beyond 2000 nm. The coherence properties of this broad-bandwidth comb are verified with heterodyne measurements and through the comparison of interleaved f-2f interferometers spanning this spectral region.

Intense ultrashort pulses at 1.05 μm are generated from a 250 MHz mode-locked Er:fiber laser [97] using a series of amplifiers and nonlinear fibers [42], shown in Figure 33. One third (35 mW) of the light produced by the Er:fiber laser is amplified in a core-pumped Er:fiber amplifier to an average power of 450 mW. Dispersion management and nonlinear pulse-shortening are achieved by carefully trimming the length of standard anomalous-dispersion single-mode fiber (SMF) between the laser and the gain fiber, and by making use of a normal-dispersion Er:doped fiber [86] (nLight Er80 4/125). After recompressing the amplified pulses

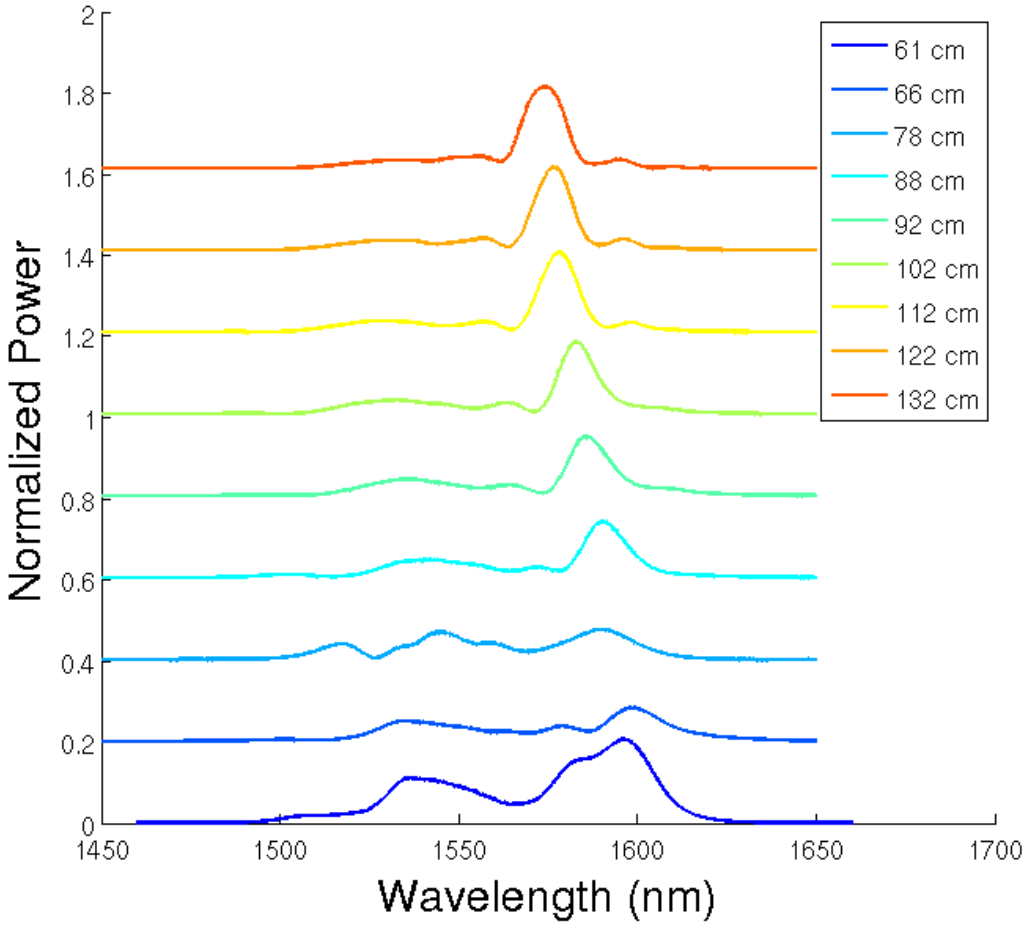

Figure 32 Optical spectra taken with fixed length of Er80-4/125 fiber and short length of single-mode fiber after amplifier (~ 30 cm) as fiber between mode-locked erbium comb and gain fiber is varied. The length chosen is ~ 78 cm, where maximum spectral broadening occurs during amplification.

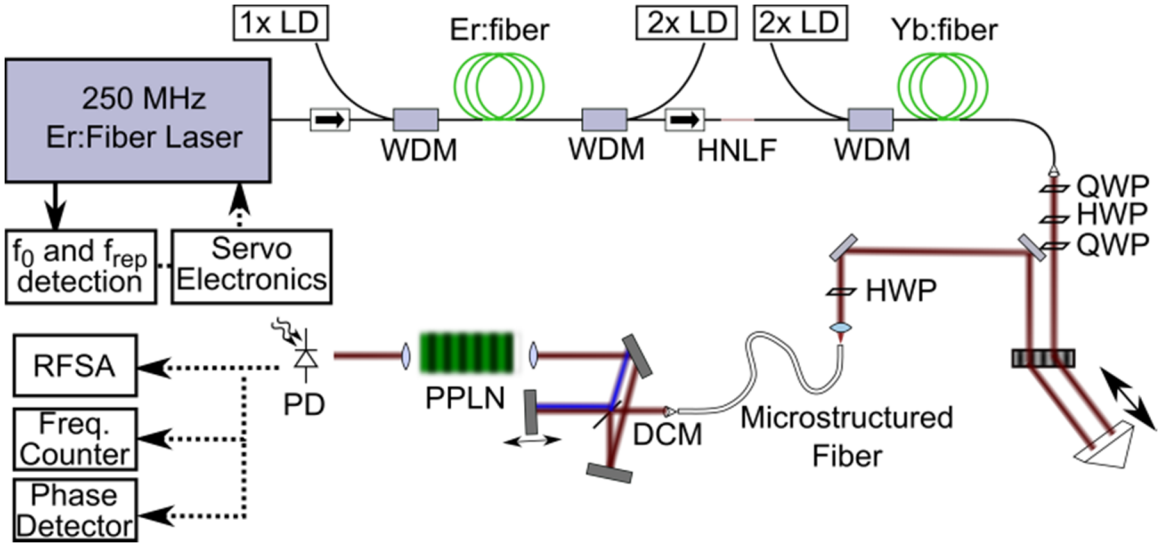

Figure 33 Schematic of apparatus used to generate and characterize 660 nm—1400 nm spectrum. LD: 600 mW, 976 nm laser diode; WDM:wavelength division multiplexer; Q(H)WP: quarter (half) waveplate; DCM: dichroic mirror; PPLN: periodically-poled lithium niobate; PD: photodiode; RFSA: radio-frequency spectrum analyzer.

in SMF, a pulse duration of 70 fs at 1580 nm is achieved as measured using SHG-FROG [40].The erbium amplifier output is fusion spliced to a 5 cm long piece of solid-core highly nonlinear fiber (HNLF) [32] with dispersion of 7.7 ps nm^{-1} km^{-1} at 1600 nm, which is in turn output-coupled by splicing to a length of SMF. This generates a supercontinuum with ~ 8 % of the 240 mW power coupled into the SMF falling between 1000 nm and 1100 nm. Within that range, the placement of the spectral peak can be refined by tuning the polarization state of light entering the Er:fiber amplifier and the HNLF. For example, to allow amplification in Yb fiber at 1030 (1050) nm, the peak can be centered at 1027 (1065) nm, with 14 (11.5) mW of power in a 70 (100) nm bandwidth. The HNLF output is then coupled into a core-pumped ytterbium fiber amplifier that provides an amplified average power of 400 mW at a pump power of ~ 1 W. For environmental stability, the entire fully-spliced amplifier and HNLF apparatus is placed inside a 15 cm × 15 cm × 10 cm box.

Using a volume holographic single grating compressor [47], the amplified 1050 nm pulses are compressed to 70 fs duration, as measured by SHG-FROG (Figure 36). To generate a spectrum extending into

the visible, these pulses are coupled into a 0.5 m microstructured nonlinear fiber with a zero-dispersion wavelength of 945 nm. Accounting for losses in the grating compressor and fiber coupling, about 110 mW of power was launched into the microstructured fiber. This generates an octave-spanning spectrum from 660 nm to 1430 nm (Figure 34).

Coherence Measurement Setup & Results

In order to verify that the light produced by the chain of amplifiers and nonlinear fibers retains the coherence of the mode-locked laser, a series of heterodyne measurements were conducted. First, a second output from the mode-locked Er:laser was used to generate an octave-spanning spectrum from 1 μm to 2 μm, which enabled frequency stabilization of the carrier-envelope offset frequency (f_{CEO}) with a standard f-2f

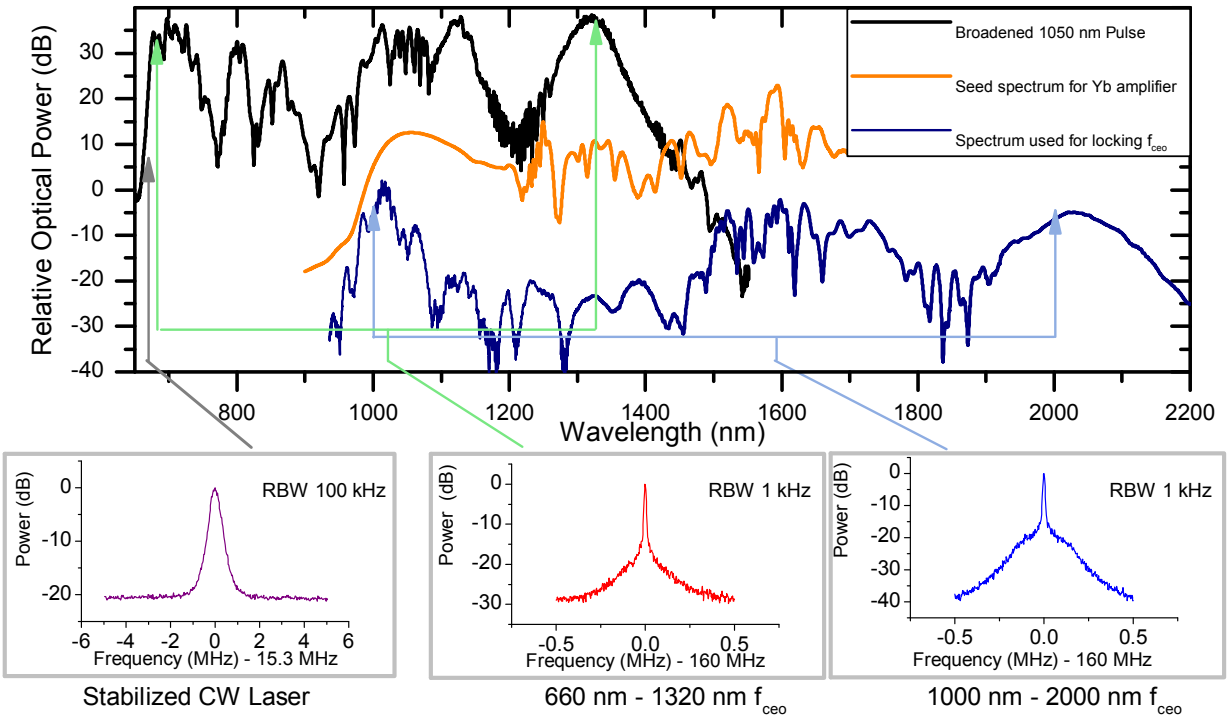

Figure 34 Top: Optical spectra of the broadened Er:comb used to seed the Yb:fiber amplifier, the broadened Yb comb, and the (independent) octave-spanning spectrum used to stabilize the Er:laser. Bottom: Heterodyne beat notes of the LFC with a 657 nm cavity-stabilized laser, the f_{CEO} beat from 660 nm to 1340 nm, and the f_{CEO} beat from 1 μm to 2 μm.

interferometer and feedback to the laser's pump current. The laser repetition rate (f_{rep}) was also stabilized relative to a Rb clock or hydrogen maser. Subsequently, utilizing the octave-spanning spectrum from the microstructured fiber, a second f-2f interferometer between 660 nm and 1320 nm was constructed to detect an out-of-loop copy of f_{CEO}. We then used a high-resolution (Λ) frequency counter [20] to characterize the instability of the in-loop (1 μm to 2 μm) and out-of-loop f_{CEO} beats. The Allan deviations computed from the time series of 1 s counter readings are shown in Figure 35. As seen, the instability of the in-loop f_{CEO} is counter-limited near 2×10^{-18} at 1 s of averaging time, while the instability of the out-of-loop f_{CEO} is only 640 mHz deviation (fractionally 1.4×10^{-15}) at 1 s averaging time.

We also measured the phase noise of the two copies of f_{CEO} (Figure 37). Above Fourier frequencies of approximately 400 Hz, the agreement between the two sets of data is nearly exact. However, at low frequencies,

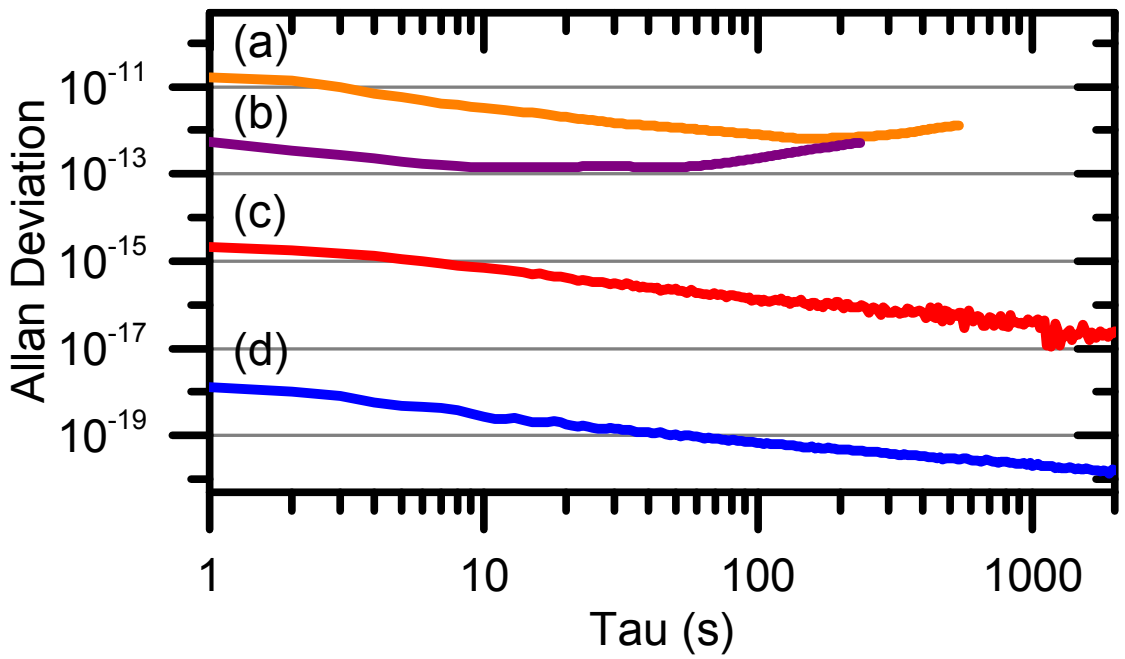

Figure 35 Fractional stability measurements of several portions of the LFC. Beat between the visible portion of the LFC and a 657 nm cavity-stabilized laser when the LFC is stabilized to a Rb clock (a) and when stabilized to a hydrogen maser (b). At short times, the relative instability is limited by the Rb clock or maser, while at long times the stability is dominated by the cavity drift. Curves (c) and (d) are the instability of f_{CEO} measured out-of-loop between 660 nm and 1340 nm and in-loop between 1 μm and 2 μm, respectively.

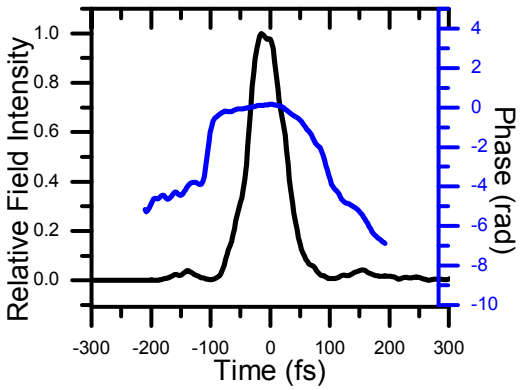

Figure 36 Amplitude and phase of the amplified 1050 nm pulse after compression, retrieved by SHG-FROG. The FWHM pulse duration is 70 fs and the average power is 300 mW.

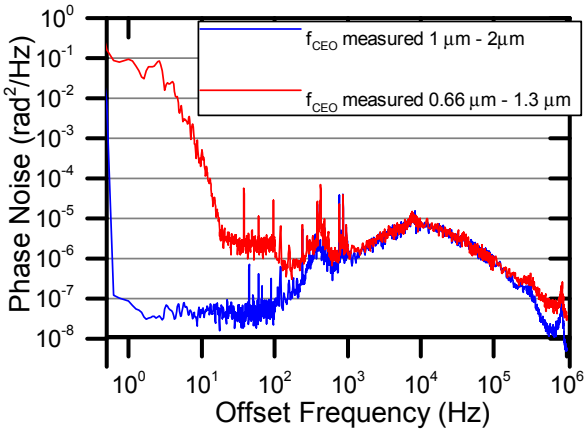

Figure 37 Phase noise of fCEO measured on the signal used to lock the laser (blue) and the out-of-loop Yb branch (red).

the phase noise of the out-of-loop f_{CEO} increases significantly – consistent with the counter data of Figure 35. Quantitatively, the integrated phase noise from 1 MHz to 1 Hz is seen to increase from 0.61 (in-loop) to 0.78 radians (out-of-loop.) A portion of the added frequency noise is due to the nonlinear processes used to generate the light. However, the two offset-beat detection arms are separated by 3 optical amplifiers, 3 pieces of nonlinear fiber, several meters of standard single-mode optical fiber, and a number of free-space optics. Thermal and acoustic perturbations of this significant out-of-loop path add excess phase noise at low frequencies. While we could expect improvements with additional environmental isolation, the data of Figure 37and Figure 35 already demonstrate sub-radian and sub-Hertz coherence of the visible and infrared spectra.

Additional independent evidence of the good coherence of the broad bandwidth continuum is provided by measurement of a beat note between the visible comb light and a cavity-stabilized 657 nm CW laser (linewidth ~ 1 Hz). A signal-to-noise ratio of >25 dB (300 kHz resolution bandwidth) was achieved and was used to drive a frequency counter. The instability of this beat is shown in Figure 35. When the mode-locked laser is referenced to a Rb microwave clock, the measured stability is consistent with the 2×10^{-11} fractional stability of the Rb clock itself; referencing the laser to the H maser reduces the short-term instability by more

than an order of magnitude. At time scales of tens of seconds, both measurements show the long-term drift of the optical cavity to which the CW laser is stabilized.

Problems with non-PM system

During the testing of the first-generation 1040 nm light generation system, it became apparent that the coherence of the output of the system was closely related to the precise polarization state of the light inside the amplifier. The most likely physical explanation for this effect, also noted in Ref. [86], is nonlinear polarization instability [1]. Recall that the propagation of an optical pulse along a birefringent optical fiber is governed by the coupled equations

$$\begin{aligned} \frac{dA_+}{dz} &= \frac{i\Delta\beta}{2}A_- + \frac{i\gamma}{3}\left(|A_+|^2 + 2|A_-|^2\right)A_+, \\ \frac{dA_-}{dz} &= \frac{i\Delta\beta}{2}A_+ + \frac{i\gamma}{3}\left(|A_-|^2 + 2|A_+|^2\right)A_-. \end{aligned} \tag{6.1}$$

It can be shown that, at optical powers above

$$P_{\mathrm{cr}} = \frac{3}{2}\left|\frac{\Delta\beta}{\gamma}\right|, \tag{6.2}$$

the state of linear polarization along the fiber's fast axis becomes unstable. Here, the birefringence $\Delta\beta = 2\pi / L_{\mathrm{B}}$, where L_{B} is the beat length [m]. Qualitatively, this can explained by the nonlinear birefringence surpassing the linear birefringence in magnitude, leading to a sensitive dependence of the fiber's total birefringence upon the optical peak power. The polarization evolution of the pulse is thus strongly coupled to perturbations in the pulse envelope, leading to instabilities. In the fiber amplifier used above, the relevant parameters are 1 m < L_B < 10 m, γ = 1.1 W km^{-1}, and the pulse energy is $\sim 1.6\,\mathrm{nJ}$. Assuming a sec^2-type pulse where the peak power is

$$P_{\mathrm{pk}} = 0.88\frac{E_{\mathrm{pulse}}}{\tau_{\mathrm{fwhm}}}, \tag{6.3}$$

the critical power is reached at a pulse duration of 160 to1600 fs, depending upon the exact birefringence.

In the laboratory, a coherent 660 nm—1320 nm f-2f beat note could only be detected when the polarization state of light was precisely set by means of free-space wave plates and could only be maintained after allowing the optical fibers to settle without manipulation for several days. The instability was significant, and it was the limiting factor in the counting measurements presented in Figure 35. While it could be possible to use an active polarization-controller to stabilize the coherence of the light generated by the amplifier and supercontinuum system, a passively stable system is preferable. For this reason, a second-generation system using all polarization-maintaining optical fibers was constructed and tested.

All-PM Version

Description of components

Polarization-maintaining (PM) fibers are simply optical fibers in which a stress structure is incorporated, breaking the cylindrical symmetry of an optical fiber. A common design known as PANDA is shown in Figure 38. By giving the fiber a well-defined birefringence much greater in magnitude than stress-

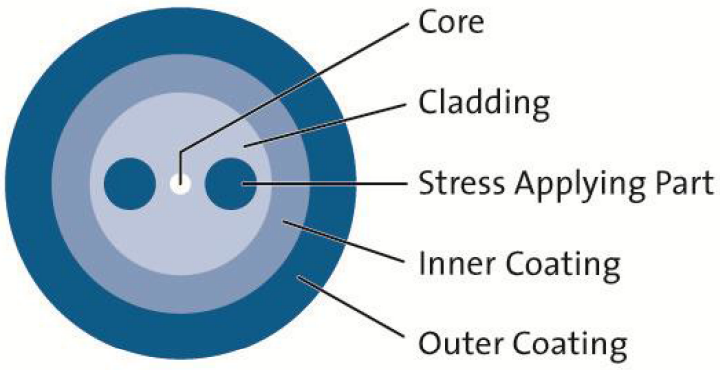

Figure 38 Schematic of PANDA PM optical fiber. Figure provided by Corning Incorporated.

induced birefringence, the evolution of linearly polarized light launched onto one of the two eigenaxes of the fiber is made almost completely stable. While PM fiber optics are more complex than conventional single-mode fibers, from the point of view of the experimentalist the key challenge when building a polarization-maintaining fiber-optic device is simply sourcing polarization maintaining fibers with suitable characteristics. A summary of polarization-maintaining fiber equivalents to telecom-wavelength single-mode fibers is provided in Table 1. Other components, such as wavelength-division multiplexers (for combining signal and pump beams), isolators,

and couplers, can all be purchased as commercial off-the-shelf parts or as custom parts with user-supplied fiber. The devices used for this work are listed in Table 2.

Table 1 Polarization maintaining fiber equivalents for useful single-mode fibers.

Single-Mode Fiber	PM Analog	PM Fiber Dispersion at 1550 nm	PM Structure	Notes
SMF-28e	PM PANDA 1550	-21,600 fs^2/m	PANDA	PANDA 1550 has dispersion similar to but not identical to SMF-28e. Dispersion data available upon request from Corning.
nLight Er80-4/125	nLight Er80-4/125-PM-HD	32,100 fs^2/m	PANDA	This fiber is not advertised and varies batch-to-batch. Specification allows for variations in small signal absorption of ±20 dB/m; typical values seem to be near 100 dB/m. Dispersion value is as measured in Chapter 6.
Sumitomo HNLF with anomalous dispersion	OFS HNLF	Strongly Anomalous	Elliptical	Sumitomo Electric does not seem to manufacture a PM highly-nonlinear fiber with the strongly anomalous dispersion key to generation of light at wavelengths below 1100 nm. An OFS fiber has been a good substitute.

Table 2 Fiber-optic devices used in all-polarization maintaining system

Fiber-optic Device	Manufacturer	Model Number	Notes
Fused PM 980/1550 WDM	AFW	WDM-PM-1598-B-P-7-0-1WPM	High-power (1 W)
Microoptic 980/1050 WDM	Micro-Optics	Custom	With Nufern PM980XP fiber for signal and reflect ports. Power handling 1 W CW. Blocking filter on pump port for 60 dB blocking of 1050 nm light in pump port (to protect pump diodes.)
PM Circulator	Thorlabs	CIR1550PM	

Construction of System

An all polarization-maintaining erbium-doped fiber amplifier is constructed using the PANDA 1550 fiber, Er:doped gain fiber, and fused WDM listed in Table 1 and Table 2. To determine the optimum lengths of gain fiber, a fiber amplifier was constructed using 230 cm of gain fiber, pumped in the forward (co-propagating) direction with 500 mW of 976 nm pump light and in the backwards (counter-propagating) direction with 1000 mW of 976 nm light. The Menlosystems 250 MHz comb with 35 mW of average output power served as the signal. The amplifier output power was then measured as the length of erbium fiber was reduced by repeatedly cutting, splicing, and re-measuring the output power. The results of these measurements are shown in Figure 40 and Figure 41, and for the final design a gain-fiber length of 100 cm was chosen.

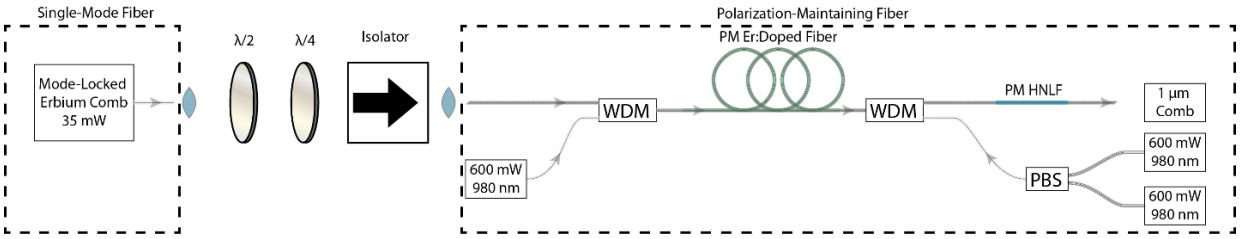

Figure 39 Physical layout of polarization-maintaining fiber amplifier. The fiber laser delivers light via single-mode fiber, and a short free-space section rotates the polarization then polarizes the light using an optical isolator. The amplifier itself is constructed in the same manner as a single-mode (non-PM) amplifier.

The length of "pre-chirp" fiber, or PANDA 1550 placed between the mode-locked laser and the amplifier, was chosen by using approximately the same length of fiber as was used in the non-PM system. The length of fiber was then varied while the pulse was characterized via FROG until an optimal length of 100 cm of total PANDA was chosen, as shown in Table 3. It should be noted that another "optimal" length of pre-chirp fiber of much shorter length may give even better results, but the long length of fiber chosen here produces relatively short pulses while also allowing for comfortable long fiber pigtails, which permits the simple and rugged enclosure of the completed amplifier.

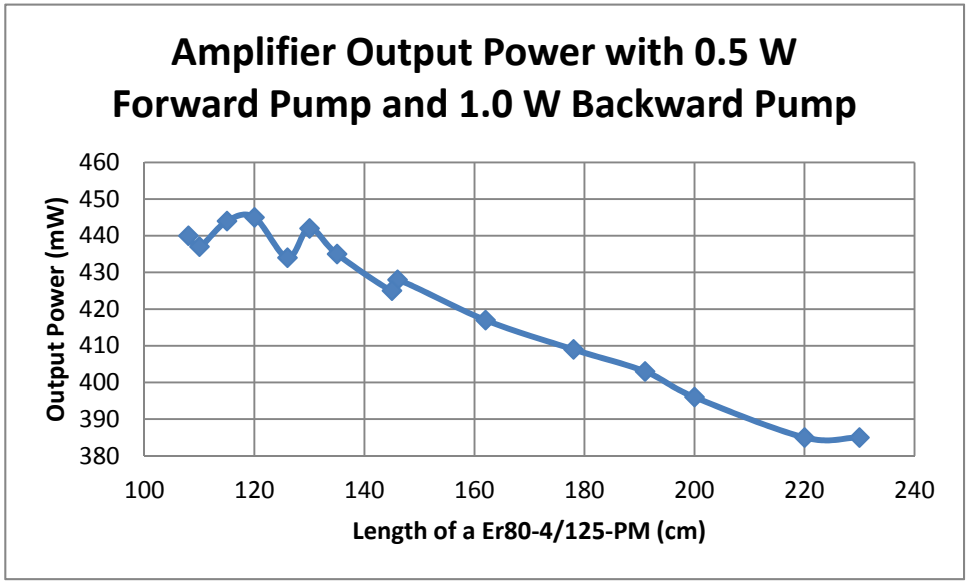

Figure 40 Measurement of erbium-fiber amplifier output power using Er80-4/125-PM gain fiber and forward and backward pumping. The seed signal is the 35 mW output of the 250 MHz Menlosystems erbium comb. Measurement was performed by repeatedly cutting and re-splicing the gain fiber.

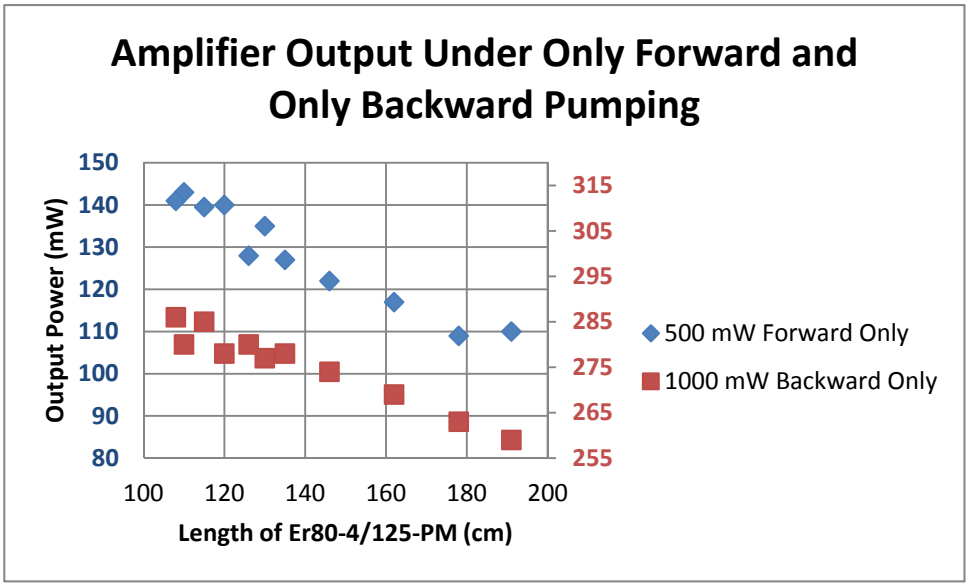

Figure 41 Secondary results from cut-back measurement showing power output of amplifier under forward-only and backwards-only pumping. The seed signal is the 35 mW output of the 250 MHz Menlosystems erbium comb. These configurations were not used for this work, but are potentially useful in the design of other amplifiers.

With the lengths of gain fiber and pre-chirp fiber chosen, all that remains is to choose the optimal length of PANDA fiber after the amplifier for compression of the pulse. While it is possible to do find an approximate "best length" by varying the compression fiber length in ~ 10 cm steps, more information can be obtained by means of a more fine-grained measurement. To this end, a series of 38 cut-back measurements were performed, with each cut removing approximately 2 cm of PANDA fiber after the amplifiers. Pulse measurements were made with both 3 pump diodes (1 co- and 2 counter-propagating) and 2 pump diodes (2 counter-propagating). The results of these measurements are shown in Figure 42 and Figure 43, in which the dynamics of the amplified pulse as it undergoes compression are revealed. In the time domain, it can be seen that, upon reaching a minimum pulse length, the pulse propagates with nearly fixed length, likely due to soliton formation.

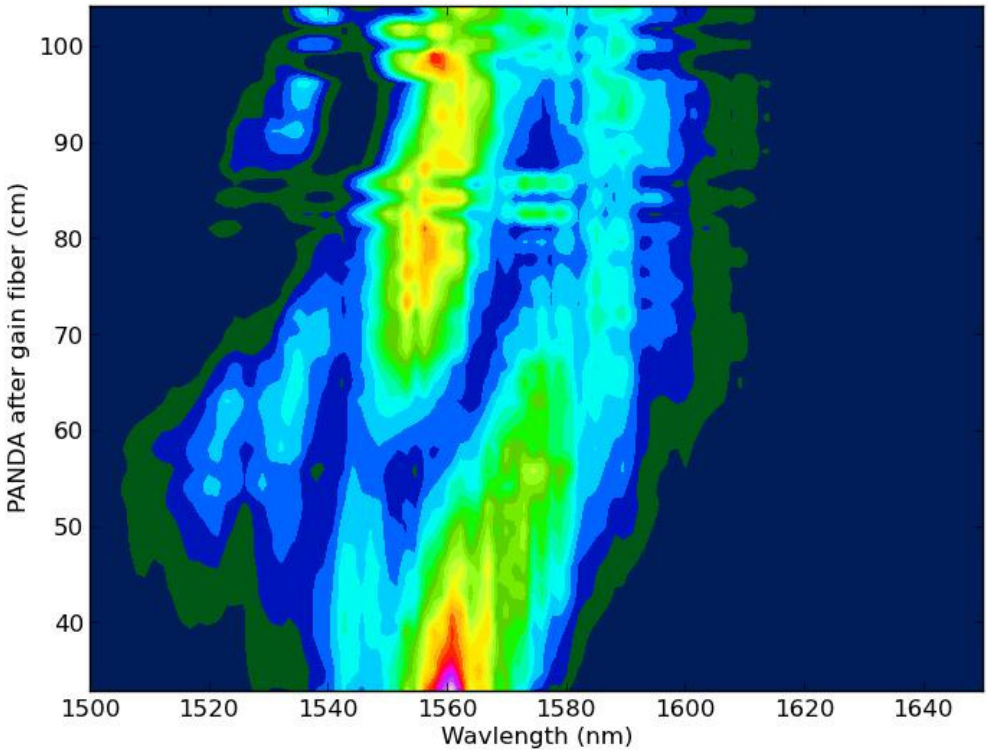

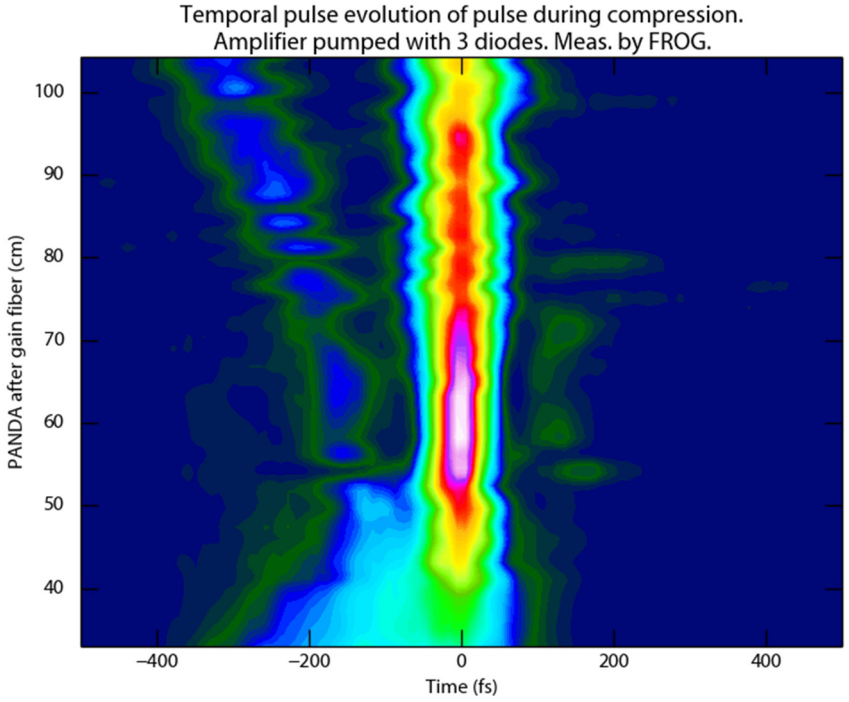

Figure 42 Waterfall plots in the wavelength (top) and time (bottom) domains of pulse compression after erbium-doped fiber amplifier pumped with 3 pump diodes. Data for top plot is measured by optical spectrum analyzer, while data for the bottom is retrieved by FROG from a spectrogram.

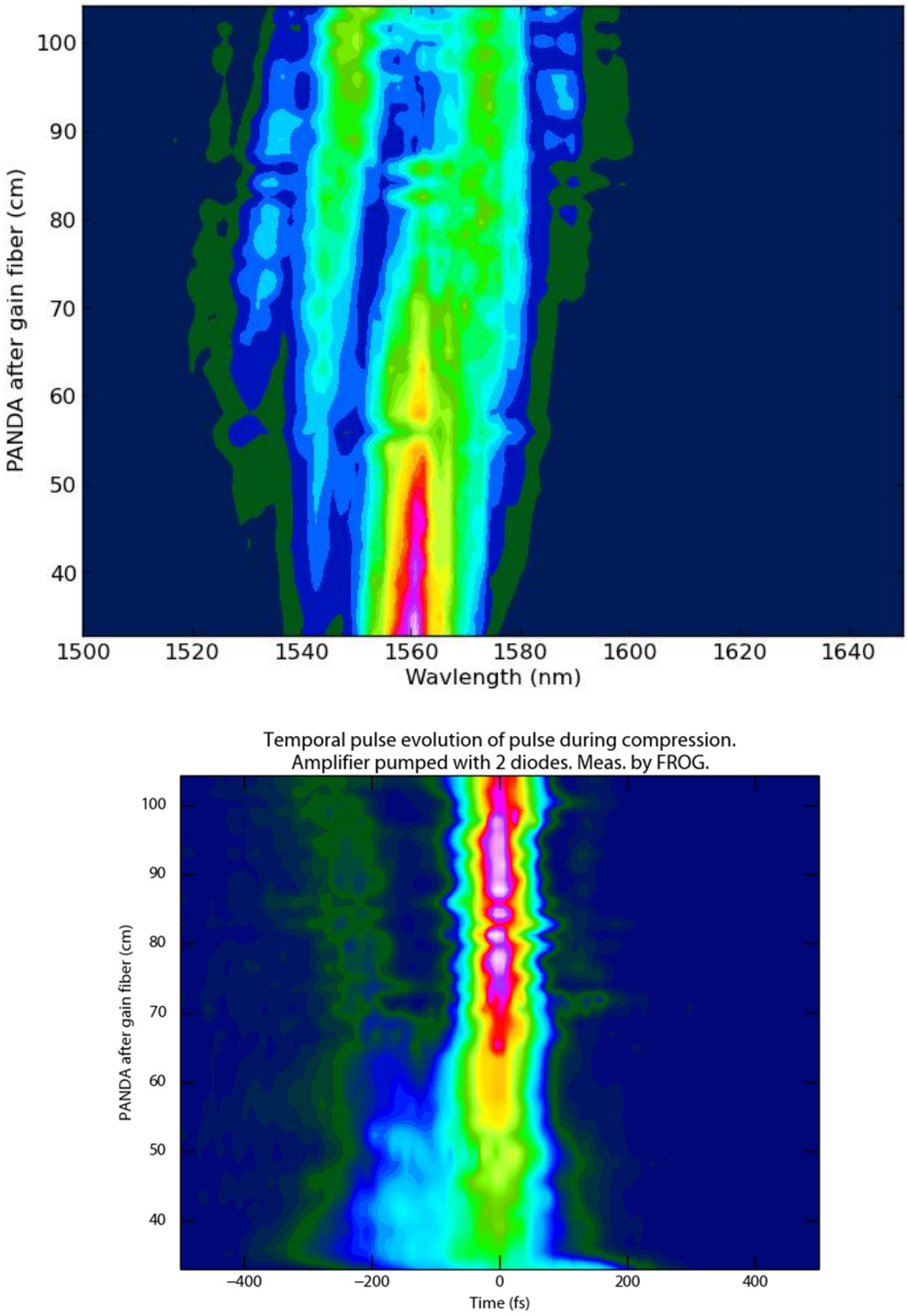

Figure 43 Waterfall plots in the wavelength (top) and time (bottom) domains of pulse compression after erbium-doped fiber amplifier pumped with 2 pump diodes. Data for top plot is measured by optical spectrum analyzer, while data for the bottom is retrieved by FROG from a spectrogram.

Table 3 Pulse measurements used to determine optimal length of PANDA fiber between laser and gain fiber. Note that FROG has a direction-of-time ambiguity, which is apparent in some of these plots.

Length of Pre-chirp Fiber (Compression fiber length fixed)	FROG retrieved time-domain pulse intensity (red) and phase (green), as plotted by Femtosoft, LLC software.
120 cm	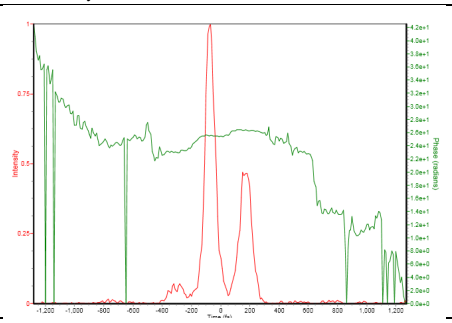
113 cm	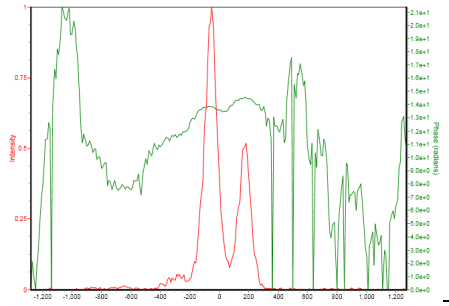
100 cm	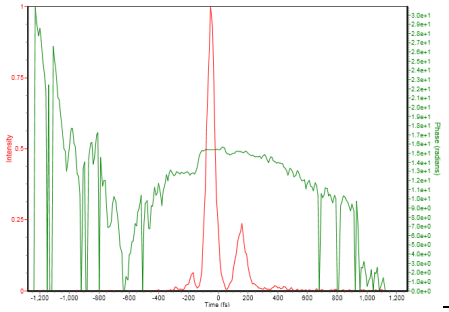
95 cm	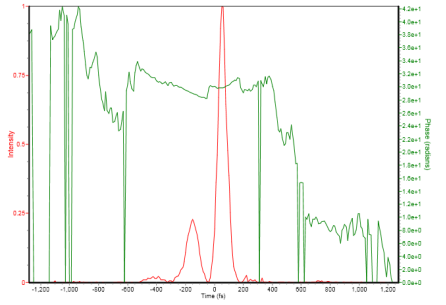
90 cm	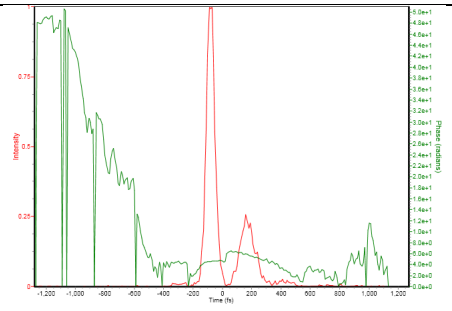

All-PM System Results

To verify that the new polarization-maintaining fiber amplifier produces light with equal coherence to the first-generation system, the output was tested as a source of visible comb light. In a first experiment, the f—2f measurement between 660 and 1320 nm was repeated and a beat with ~ 20 dB signal-to-noise was observed (unfortunately, these data were not saved.) Experimenting with other optical fibers, it was noted that yellow, green, and even blue-green light could be produced. In particular, launching temporally compressed output of the amplifier onto one axis of a polarization-maintaining PCF with ZDW of 780 nm, it was possible to generate very large amounts of light at 532 nm, as can be seen in Figure 44. The coherence of this light was investigated by heterodyne with a single-frequency solid-state diode-pumped 532 nm laser (Verdi V8). A beat was observed with SNR of more than 20 at a resolution bandwidth of 300 kHz. Most significantly, this beat was extremely stable and completely unaffected by manual manipulation of any of the PM fiber optics comprising the amplifier. This stability is exactly what was desired, and this polarization-maintaining frequency-conversion system is well-suited to the spectrograph calibration application.

For the generation of a Z,Y, and J band calibrator, it is important to generate a frequency comb spanning 800—1320 nm with low amplitude variation. This spectrum must be generated by nonlinear broadening, and two different fibers were tested. One is designed for supercontinuum generation, with zero dispersion at 1050 nm (NKT NL-1050-ZERO-2) while the second fiber has normal dispersion (NKT NL-1050-NEG-1.) While nonlinear fibers that are normally dispersive at the pump wavelength are less conducive to the generation of broad-band supercontinua, they are known to produce flatter, less structured, and more stable spectra as compared to more standard zero dispersion designs [31]. Experimentally, we see results which mirror these expectations. Coupling the 70 fs pulses into the nonlinear fiber, 0.5 nJ pulses are launched into samples of each fiber, resulting in the supercontinua shown in Figure 40. The anomalously dispersive fiber is clearly capable of

generating a Z-J band spanning spectrum, while the normally dispersive fiber covers the Y band (970—1110 nm) with a flat spectrum, while reaching to parts of the Z and J bands.

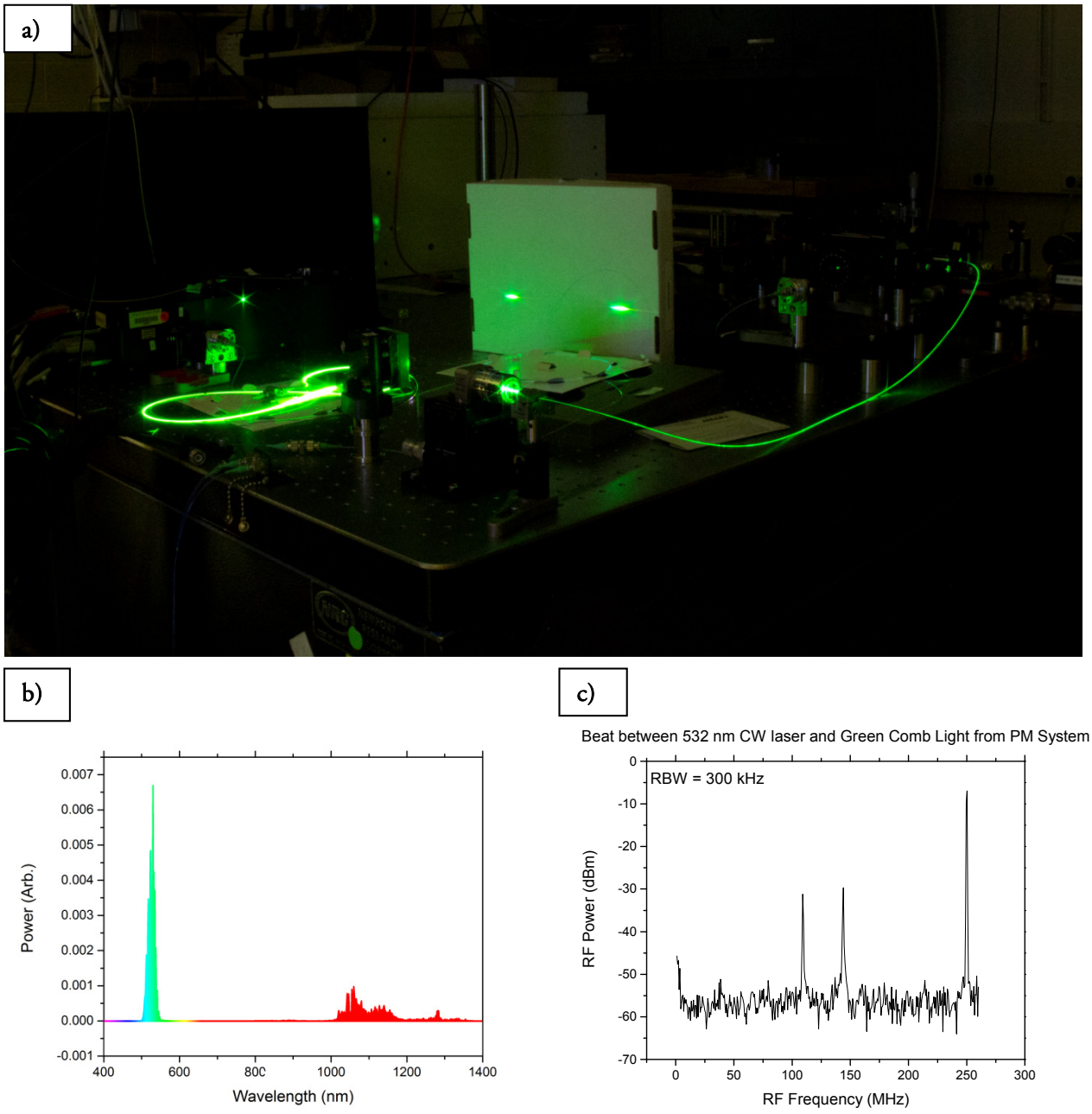

Figure 44 (a) Photograph of PM amplifier (green fibers in lower left) generating green supercontinuum (fiber in foreground.) The visible supercontinuum spectrum is dispersed using a diffraction grating onto the card in the center. (b) Spectrum of supercontinuum recorded by optical spectrum analyzer (grating monochromator.) (c) Heterodyne beat between the green supercontinuum with CW 532 nm laser (Verdi V8). Significantly, the coherence of this light is extremely stable and no special efforts to obtain optimal coherence of the beat were necessary.

These experiments were conducted using only a pre-amplifier capable of generating 400 mW of average power, 120 mW of which were coupled into the PCFs. While this is the maximum power to which the erbium laser has been amplified, an experiment was conducted using a different 100 MHz laser and ytterbium-fiber power amplifier capable of generating few-W levels of power. The same two nonlinear fibers were seeded with light from this system, and the results are shown in Figure 41. This experiment indicates that for full coverage of the Z-J bands a power amplifier may be needed, for our initial work we restrict the scope to generating a filtered comb in the Y band, and opt to use the normal-dispersion NL-1050-NEG-1 fiber with spectrum shown in Figure 46.

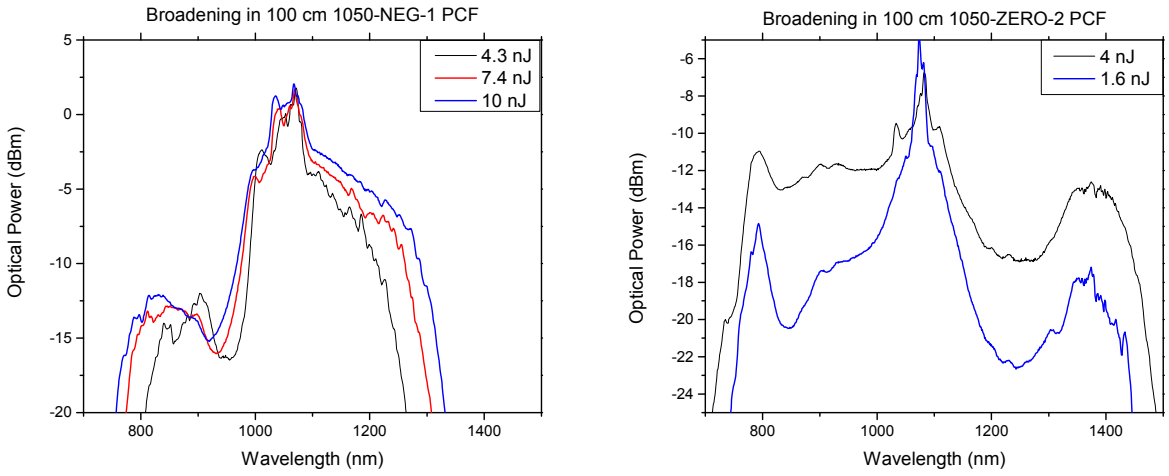

Figure 45 Supercontinuum spectra achieved by nonlinearly broadening strongly amplified 100 MHz, sub-200 fs ytterbium mode-locked laser. While this light was not used as a frequency-comb, these data are a useful guide to the power scaling of the spectra with pulse energy. The energies quoted here are the coupled pulse energies, determined by measuring the total output power of each fiber on a thermal power meter and dividing by the 100 MHz pulse repetition frequency.

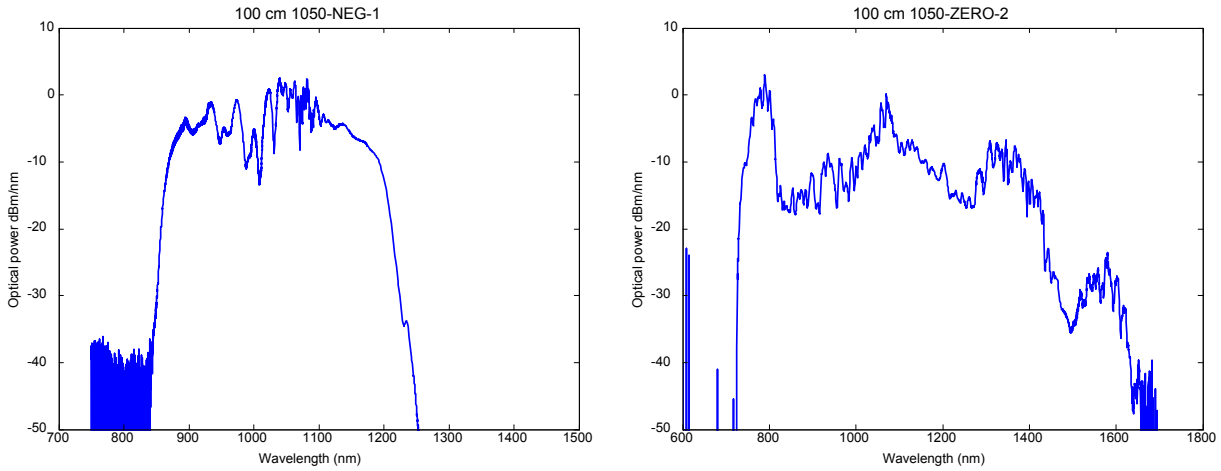

Figure 46 Supercontinuum spectra achieved by nonlinearly broadening 250 MHz erbium comb after extension to 1050 nm and amplification in core-pumped ytterbium fiber amplifier. Coupled pulse energy is ~ 0.6 nJ.

Conclusion

In summary, we demonstrated an all-fiber source of high quality, 70 fs pulses at 1050 nm. The short duration and high peak power of these pulses enable coherent and continuous extension of the Er:fiber-based frequency comb to visible wavelengths. We believe this source will be useful for applications such as broad-bandwidth spectroscopy and LFC-based calibration of high-precision astronomical spectrographs in the near-infrared and visible.

Chapter 7

THEORY AND MODELING OF ULTRAFAST FIBER OPTICS

Erbium and ytterbium-doped fiber amplifiers are key to the extension of high-repetition rate mode-locked fiber lasers. While erbium-doped fiber amplifiers (EDFAs) have been used throughout this thesis, the theory of their performance has not yet been discussed, because EDFAs are typically designed using simple guidelines. This is due largely to the challenges of characterizing a light field contained inside an optical fiber, as well as the fact that, when all is said and done, the only real degree of freedom is the length of a few fibers. While the restriction to only a few degrees of freedom is fundamental, it is possible to use modeling to better understand and design nonlinear amplifiers.

The measurements presented in Chapter 6 provide an opportunity to connect the actual devices with theory, and the aim of this chapter is to outline the linear and nonlinear optics at work, determine the important parameters in the all-polarization maintaining fiber EDFA, and show that the performance of the amplifier can in fact be predicted with good accuracy. These data and models will hopefully assist in the design of new amplifiers using the same fibers. First, the physics of erbium fiber amplifiers will be presented and results from a numerical model will be shown. Second, the self-similar parabolic pulse solution to the generalized nonlinear Schrödinger equation with gain is shown, and a numerical split-step solver is demonstrated. Finally, measurements of fiber dispersion, erbium-fiber distributed gain, and the complex electric field of the input pulse are used as inputs for the model and a comparison of the model result with the experimentally measured behavior is made.

Erbium Fiber Physics

The physics governing the operation of rare-earth doped fiber amplifiers has been extensively studied, as have means of modeling the amplifiers' operation [29, 84, 92]. In the work presented here, the important gain ion is Er^{3+}, and we will focus on the behavior of erbium-fibers. The electronic transitions of Er^{3+} important to amplification and lasing are the 980 nm pump transition, ${}^4I_{15/2}$-${}^4I_{11/2}$, and the 1520 nm – 1570 nm signal transition, ${}^4I_{15/2}$-${}^4I_{13/2}$. At room temperature, the spectral bandwidth of the lasing transition is very broad. This is a result of the crystal-electric field, which leads to Stark splitting of the ground and metastable states. As a result, the total number of ${}^4I_{15/2}$-${}^4I_{13/2}$ transitions for each particular Er^{3+} ion is 56, while the magnitude of the splitting varies from $10 \text{ to } 100 \text{ cm}^{-1}$ [56]. At room temperature, these transitions are homogenously broadened by electron-phonon interactions to such an extent that they are not resolvable. The co-doping of aluminum along with erbium into the glass matrix facilitates the presence of Er^{3+} ions at a wide range of bonding distances, enhancing the inhomogeneous broadening and leading to flatter gain and absorption spectra [29].

In the simplest case, a fiber optic amplifier can be described [29] by the coupled rate equations for the population of excited erbium ions $n_2(r,\phi,t)$ and the optical power $P_k(z)$ in each channel of bandwidth $\Delta\nu_k$ centered at the optical frequency ν_k. The coupled equations for n_2 and P_k are as follows. The number density of the metastable state is governed by the optical pumping from each optical field and by the non-radiative decay of the excited state,

$$\frac{dn_2}{dz} = \sum_k \frac{I_k(r,\phi,t)}{h\nu_k}\left(\sigma_{ak} n_1(r,\phi,t) - \sigma_{ek} n_2(r,\phi,t)\right) - \frac{n_2(r,\phi,t)}{\tau}, \tag{7.1}$$

where τ is the lifetime of the metastable state, σ_{ak} and σ_{ek} are the absorption and emission cross-sections at ν_k and n_1 and n_2 are the population densities of the ground and metastable states, related by the equation

$$n_t(r,\phi,z) = n_1(r,\phi,z) + n_2(r,\phi,z), \tag{7.2}$$

where n_t is the local erbium ion density. Each optical field is coupled to the erbium ions,

$$\frac{dP_k}{dz} = \int_0^{2\pi}\int_0^{\infty}\left(u_k \frac{I_k(r,\phi,z)}{P_k(z)}\right)\left(\sigma_{ek} n_2(r,\phi,z)\left(P_k(z) + mh\nu_k\Delta\nu_k\right) - \sigma_{ak} n_1(r,\phi,z) P_k(z)\right) r dr d\phi\,. \tag{7.3}$$

The factor u_k accounts for the direction of the beam, with possible values of $+1$ (forward) and -1 (backwards.) The term proportional to $mh\nu_k\Delta\nu_k$ accounts for spontaneous emission, with m being the number of supported optical modes. It is equal to 2 in a single-mode fiber, one for each orthogonal polarization state. To solve these equations numerically, numerical integration is used. Variables for each of the pump, signal, and amplified spontaneous emission (ASE) fields are initialized, and a Runge-Kutta integrator is used to perform the numerical integration. In the presence of counter-propagating beams it is necessary to repeatedly run the integrator in the $+z$ and then $-z$ directions until a solution converges which accounts for the interaction of light traveling in opposite directions along the fiber.

It is important to note that these equations assume a simple 2-level system, an assumption which begins to break down at pump power levels above 1 W, where the rate of pumping from ${}^4I_{15/2}$-${}^4I_{11/2}$ becomes comparable to the non-radiative decay rate. For this reason, quantitative results from this model are inaccurate, predicting up to twice as much optical power output as is experimentally realized. The results do, however, provide qualitative insight into the behavior of fiber amplifiers, and an example simulation with fiber parameters meant to approximate the nLight Er80-4/125 fiber is shown in Figure 47.

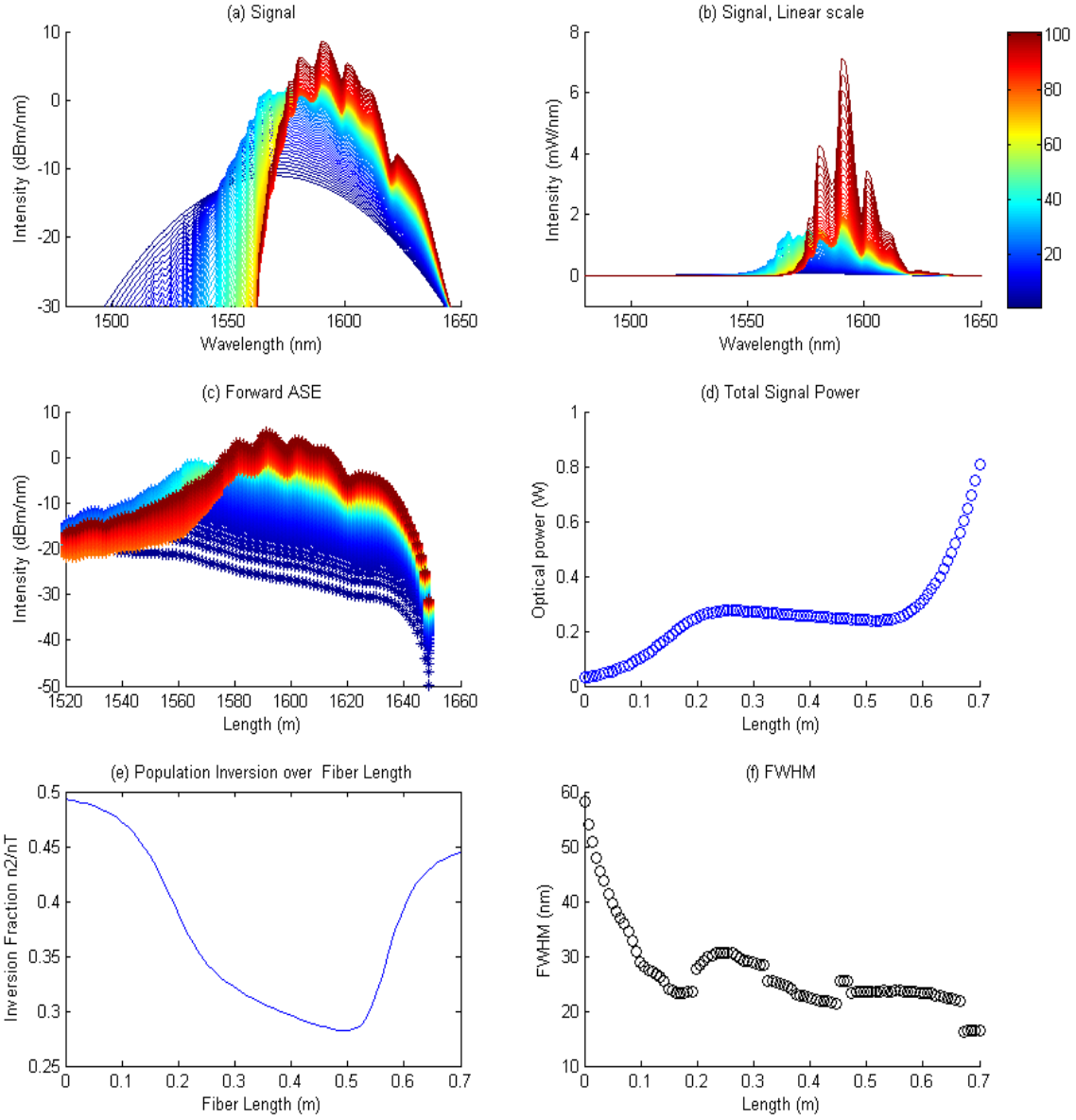

Figure 47 MATLAB implementation of numerical model from Ref. [29]. Spectroscopic data for aluminum phosphate co-doped erbium-doped fiber [35] are used, along with values approximating the nLight Er80-4/125 fiber for the erbium ion doping concentration, fiber numerical aperture, and mode-field diameters of the pump and signal fields. Subplots (a) and (b) show the signal spectrum as it moves through the doped fiber, with blue being the seed and red being the output after 70 cm of fiber; the input is a Gaussian spectrum with total power 35 mW and σ=25 nm. The pump field has a wavelength of 976 nm and powers of 0.5 W in the co-propagating direction and 1.0 W in the counter-propagating direction. (c) Amplified spontaneous emission (ASE) traveling in the forward (co-propagating) direction in each of 100 bins. The integrated signal-to-ASE ratio is 8×103. (d) Total signal power as a function of fiber length. Note that the calculated 800 mW of signal output power is not realistic; the experimentally achievable output power for this amplifier is approximately 450 mW. (e) Fractional population of metastable state as a function of fiber length. (f) Full-width at half maximum of signal optical spectrum. Note that the spectral bandwidth compresses as the signal gains power. This "gain-narrowing" lengthens the transform-limited pulse duration.

For the purposes of generating highly coherent supercontinuum spectra by broadening in nonlinear fibers, it is desirable to obtain sub-70 fs pulses. The model results shown in Figure 48 highlight an important consequence of the limited gain-bandwidth of the doped fiber: a limitation on the shortest pulse achievable by linear gain. The output spectrum of a power EDFA has a typical bandwidth of ~ 6 THz and therefore a transform-limited pulse with 90 fs duration. In order to generate the desired shorter pulses without resorting to lossy techniques such as gain-flattening filters, nonlinear optics must be used.

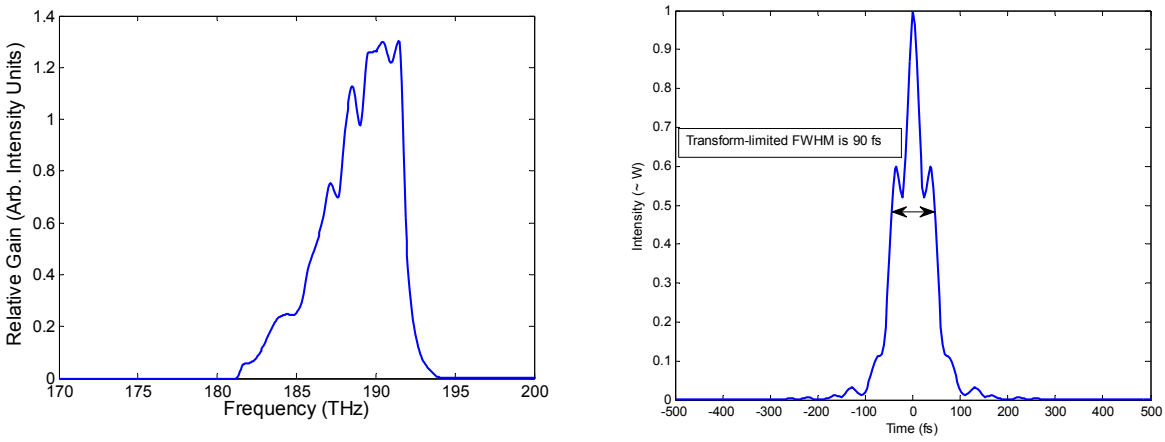

Figure 48 (a) Typical spectrum of flat, broadband seed amplified by erbium-doped fiber. (b) Fourier transform of erbium fiber emission spectrum. The 90 fs transform-limited pulse duration is consistent with the 6 THz gain bandwidth of erbium fiber and a time-bandwidth product of 0.54.

Nonlinear Amplifiers with Normal Dispersion

There exists an extremely useful solution to the nonlinear Schrodinger equation in the presence of gain. An excellent review of this self-similar pulse phenomenon can be found in [23], and I will provide a short summary. Historically, the possibility of wave-breaking-free pulse amplification was discovered by Anderson *et al* [2], followed by an observation of nonlinear pulse shortening by Tamura and Nakazawa in 1996 [86]. In

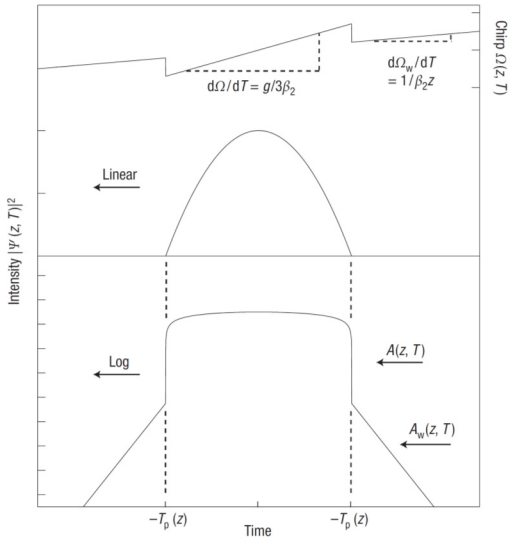

Figure 49 Asymptotic solution to the NLSE with gain. Figure from [23].

2000, Fermann *et al* [27] showed parabolic pulse evolution in an ytterbium amplifier, making use of frequency-resolved optical gating to definitively show the characteristic linearly chirped parabolic pulse.

Qualitatively, it is fairly easy to see how a normal-dispersion gain fiber is able to use nonlinearity to achieve nonlinearly-broadened output spectrum while simultaneously avoiding pulse breakup. It is well known that nonlinear self-phase modulation acts upon an optical pulse by symmetrically broadening the pulse' spectrum while also imposing a normal-dispersion chirp upon the pulse. While an anomalous dispersion fiber would tend to reverse this effect, compressing the pulse inside the gain fiber, a normally dispersive fiber will instead permit the pulse broadening. This leads naturally to the pulse peak power decreasing, but in an amplifier gain can precisely balance the dispersive decrease in peak power. In the case where the effects of gain, dispersion, and nonlinearity are "perfectly" balanced, a pulse with a parabolic-shape can propagate down through the amplifier, gaining increasing spectral bandwidth as it propagates [2, 86, 27]. The following section uses a simple

toy model to show how such an amplifier can be used for achieving spectrally-broad amplified pulses, even when seeded with non-parabolic pulses.

The evolution of optical pulses in nonlinear media is determined by the linear dispersion of the medium, which describes the rate at which different colors of light accumulate phase as they traverse a material, and the nonlinear parameter, which accounts for the modification of the refractive index of the medium by the presence of an optical field. Dispersion can be defined by the expression

$$\frac{\partial A}{\partial z} = i\beta(\omega)A \ , \tag{7.4}$$

where A is the spectral density [$W^{1/2}$] and

$$\beta(\omega) = \sum_{n=0}^{\infty} \frac{1}{n!}(\omega - \omega_0)^n \beta_n \ . \tag{7.5}$$

Here, the β coefficients are usually referred to as the "orders of dispersion." The first significant coefficient is β_2 , the second-order or group-delay dispersion, followed by β_3 (third-order) and higher terms. The nonlinear parameter γ accounts for both the nonlinear index of refraction n_2 of an optical fiber and also the confinement of the optical field within it. It is defined as

$$\gamma = \frac{\omega_0 n_2(\omega_0)}{cA_{\text{eff}}(\omega_0)}, \tag{7.6}$$

where ω_0 is the optical pulse's angular carrier frequency and A_{eff} is the effective area of the optical mode.

The governing equation for the evolution of an optical pulse in an amplifier is the nonlinear Schrödinger equation with gain [23],

$$i\frac{\partial A}{\partial z} = \frac{\beta_2}{2}\frac{\partial^2 A}{\partial T^2} - \gamma \mid A \mid^2 A + i\frac{g}{2}A, \tag{7.7}$$

where A [$W^{1/2}$] is the pulse envelope, β_2 [fs^2 m^{-1}] is the group delay dispersion at the signal frequency, γ [$W^{-1}m^{-1}$] is the nonlinear parameter, and g is the distributed fiber gain [m^{-1}].

A simple type of pulse to model with this equation is the Gaussian pulse, which has the following properties. Consider a transform-limited pulse with Gaussian envelope[1],

$$E_{gaussian}(t) = A_t \sqrt{e^{-\log(2)\left(\frac{2t}{\Delta t}\right)^2}}\, e^{-i\omega_0 t} + C.C. \tag{7.8}$$

here Δt [s] is the pulse full width at half maximum, and ω_0 [rad s^{-1}] is the carrier frequency. An expression for a *chirped* Gaussian pulse is desired, with the effect of group-delay dispersion taken into account. To understand the effect of dispersion, it is most natural to transform to the frequency-domain. This is accomplished via a Fourier transform, with the frequency-domain Gaussian pulse given by

$$E_{gaussian}(\omega) \frac{A_t \Delta t}{\sqrt{4\log(2)}} e^{-(\omega-\omega_0)^2 \frac{\Delta t^2}{8\log 2}} . \tag{7.9}$$

The action of group-delay dispersion (GDD) in the frequency domain is simply the addition of quadratic phase,

$$\phi_{GDD}(\omega;\omega_0) = \frac{\beta_2}{2!}(\omega-\omega_0)^2 , \tag{7.10}$$

where β_2 [s^{-2}] is the total GDD. The phase is applied to the pulse by multiplying by the phasor $\exp(-i\phi)$, and the chirped Gaussian pulse in the frequency domain is

$$E_{gaussian}(\omega) \frac{A_t \Delta t}{\sqrt{4\log(2)}} e^{-(\omega-\omega_0)^2 \frac{\Delta t^2}{8\log 2}} \exp\left(-i\frac{\beta_2}{2}(\omega-\omega_0)^2\right). \tag{7.11}$$

A second Fourier transform yields the linearly chirped pulse-envelope in the time domain,

[1] This derivation proceeds along the lines of Newport's tutorial "The Effect of Dispersion on Ultrashort Pulses."

(7.12) $$E_t\left(t;\beta_2\right) = A_t\sqrt{\frac{\Delta t^2}{\Delta t^2 + i4\log 2\beta_2}}e^{-\frac{2\log 2t^2}{\Delta t^2 + i4\log 2\beta_2}}.$$

Commonly the pulse energy E_p [J] and transform-limited time duration are known, and the peak electric field intensity A_t can be expressed in terms of these,

(7.13) $$A_t = \frac{4E_p}{\sqrt{\pi}\Delta t}.$$

Using this expression for the chirped Gaussian pulse, the NLSE with gain can be numerically solved.

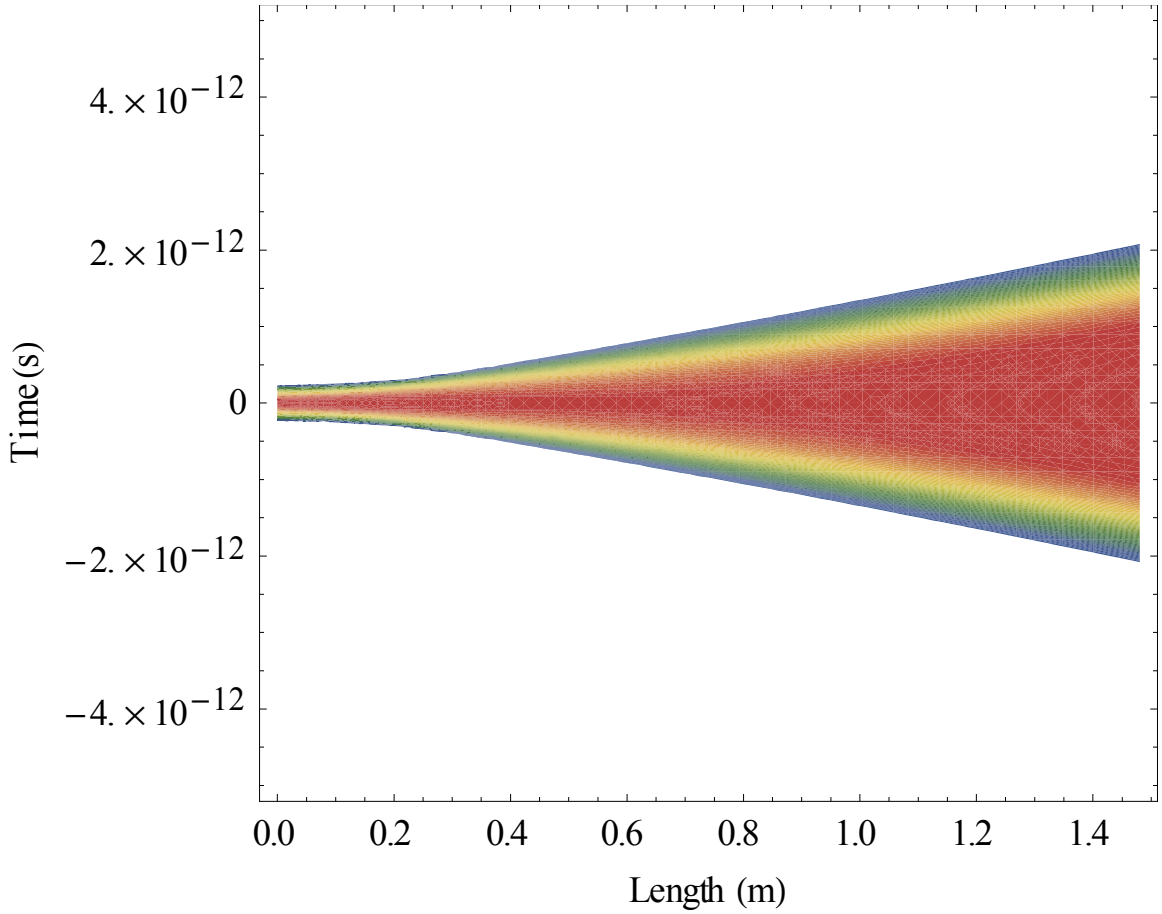

Figure 50 Solution of nonlinear Schrodinger equation with gain for 150 fs, 140 pJ, transform-limited input pulse with β_2=32,000 fs^2 m^{-1} , g = 2 m^{-1}, and γ=5 W km^{-1}.

Of particular interest is the effect of the pulse chirp on the dynamics during amplification. *Mathematica* can be used to solve Eq. (7.7) fed with the pulse envelope defined in Eq. (7.12) with realistic values for dispersion, gain, and nonlinearity. A sample result of this calculation is shown in Figure 50. To see the effect of pulse chirp upon the nonlinear amplification, a phase plot showing the pulse frequency bandwidth versus pulse temporal duration can be made for a range of anomalous to normal chips, shown in Figure 51. It can be seen that anomalously chirped pulses undergo simultaneous temporal and spectral compression, followed by a rapid increase in spectral bandwidth. The model result indicates that for these pulses, larger input chirps lead to more rapid spectral expansion as a consequence of higher pulse energy at the point of shortest duration. Conversely, normally chirped pulses do not suffer from any spectral compression, but monotonically increase in temporal and spectral bandwidth. In this case, lower initial chirp leads to larger and more rapid spectral expansion. While the model used here is extremely simple, a more careful study using a fully coupled nonlinear-fiber amplifier model has been performed with the same result: the optimum chirp for ultrashort pulse generation in a normally dispersive gain medium is anomalous [15].

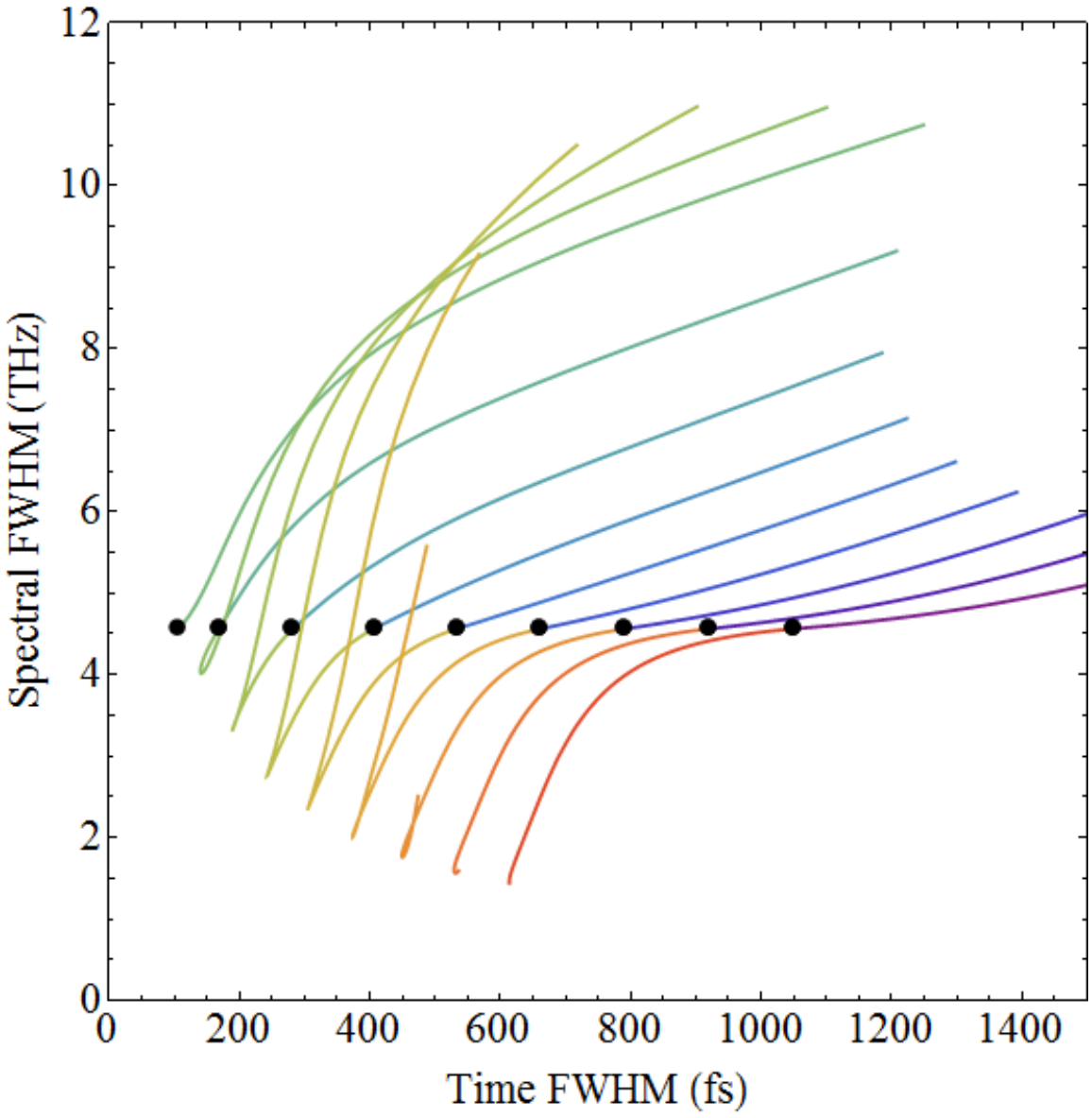

Figure 51 Dependence of nonlinear pulse amplification upon pulse chirp. Amplifier is seeded with chirped Gaussian pulse of 150 fs transform limited pulse duration. Different curves correspond to different initial dispersions, from -100,000 fs^2 to 10000 fs^2. The red curve is the most anomalously chirped, while the purple is the most normal. Input pulse energy is 140 pJ, gain is 2.0 m^{-1}, gain fiber nonlinear coefficient is γ=5 W^{-1} km^{-1}, and dispersion is 32,000 fs^2/m.

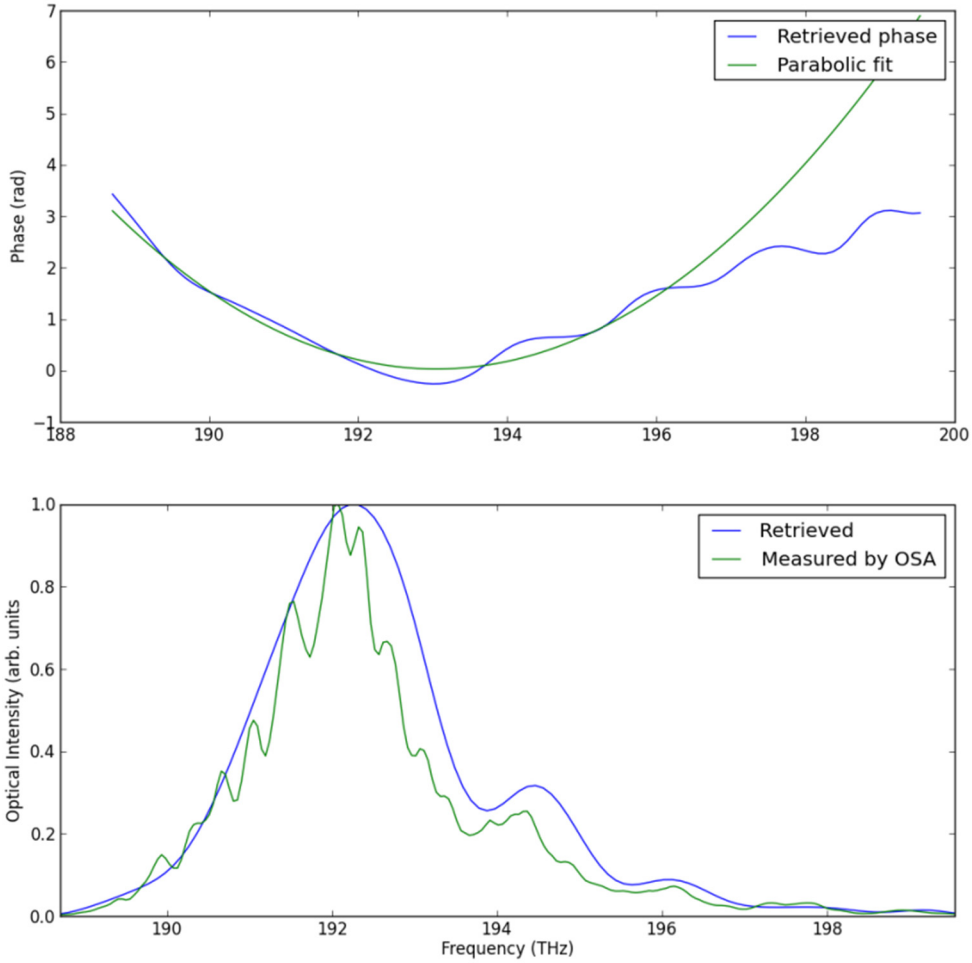

Figure 52 Retrieved phase and intensity of 1550 nm pulse as it is compressed in PM fiber. Note the good agreement of the phase with a parabola, characteristic of self-similar type amplification as well as the presence of higher order dispersion at higher frequencies.

Split-Step Integration

While the simple model presented above is useful for gaining insight into the normal-dispersion amplifier, accurately predicting the behavior of a pulse during nonlinear amplification and compression in single-mode fiber requires accounting for higher orders of dispersion, Raman gain, and the gain spectrum of

the fiber. A good starting point for the implementation for this model is a MATLAB code included in Chapter 3 of Ref. [24]. This code uses a split-step Fourier integrator, in which the effects of linear dispersion in the frequency domain and nonlinear interactions in the time domain are periodically evaluated as integration proceeds along the fiber. To accurately model the amplifier gain, linear gain is accounted for by scaling the total gain spectrum shown in Figure 48 and scaling to achieve the experimentally realized gain. While this scheme does not account for the amplifier dynamics, it is sufficient to get very good agreement with experimental results. I should note that while the code presented in Ref. [24] is excellent, as written the code will not properly set the phases of a chirped input pulse. To remedy this, line 50 of the code listing for *gnlse.m* should be modified to read

```
[Z, AW] = ode45(@rhs, Z, ifftshift(ifft(A)), options); % Run integrator
```

Fiber Parameters

In order for the models used in the section to generate physical outputs, accurate measurements of the dispersion of the erbium-doped gain fiber and the pulse entering the amplifier are required. The values used in this chapter were derived from frequency-resolved optical gating (FROG) measurements in conjunction with the known dispersion properties of the PANDA 1550 fiber and estimates of the nonlinear coefficient. These measurements were performed as follows.

First, the dispersion of the single-mode PANDA PM 1550 fiber is estimated by calculating the group delay dispersion of the amplified 1550 nm pulse as measured in the FROG cutback experiment. Measurements of the pulse chirp are shown in Figure 57, and from the change of chirp with fiber length an approximate β_2 value of -21,600 $fs^2\ m^{-1}$ or D = 17 ps $nm^{-1}\ km^{-1}$ is obtained. This result is in very good agreement with the value reported by Corning for this fiber of D = 17.5 ps $nm^{-1}\ km^{-1}$, and this gives a high degree of confidence in this method for measuring the fiber dispersion. The total group-delay dispersion of the pulse entering the gain fiber

was measured to be -18,000 fs^2 and the gain fiber length is almost exactly 1 meter. Neglecting the effect of nonlinearity on the pulse chirp, the group delay dispersion of the gain fiber is calculated to be 32,100 fs^2 m^{-1}, or D = -25 ps nm^{-1} km^{-1}.

The remaining unknown parameter is the nonlinearity coefficient, which can be roughly estimated by making use of the specified mode-field diameter of the erbium-doped fiber and neglecting the effect of dopants on the nonlinear refractive index. Simply scaling the nonlinear coefficient for single-mode optical fiber by the ratio of mode-field areas, see Table 4, gives an approximate nonlinear coefficient for the nLight Er80-4/125 gain fiber of 5 W km^{-1}.

Table 4 Estimation of nonlinearity coefficient for erbium doped fiber using simple area scaling.

	SMF-28e	Er80-4/125
Mode Field Diameter	10.4 μm	6.5 μm
Nonlinearity Coefficient	1.1 W^{-1} km^{-1}	*2.8* W^{-1} km^{-1}

Results and Conclusion

Using this model along with measurements of the gain fiber dispersion, compression fiber dispersion, gain fiber gain-spectrum, input pulse spectrum, and input pulse chirp, the nonlinear fiber optic amplifier can be accurately simulated. A waterfall-type chart showing the evolution of the 250 MHz Menlosystems laser through a 1 m long length of Er80 4/125 gain fiber followed by compression in anomalously dispersive PANDA 1550 fiber is shown in Figure 53. Notably, the fiber length of maximum compression predicted by the model agrees to within 5 cm of experiment, see Figure 55, and the time-domain pulse envelope almost identically

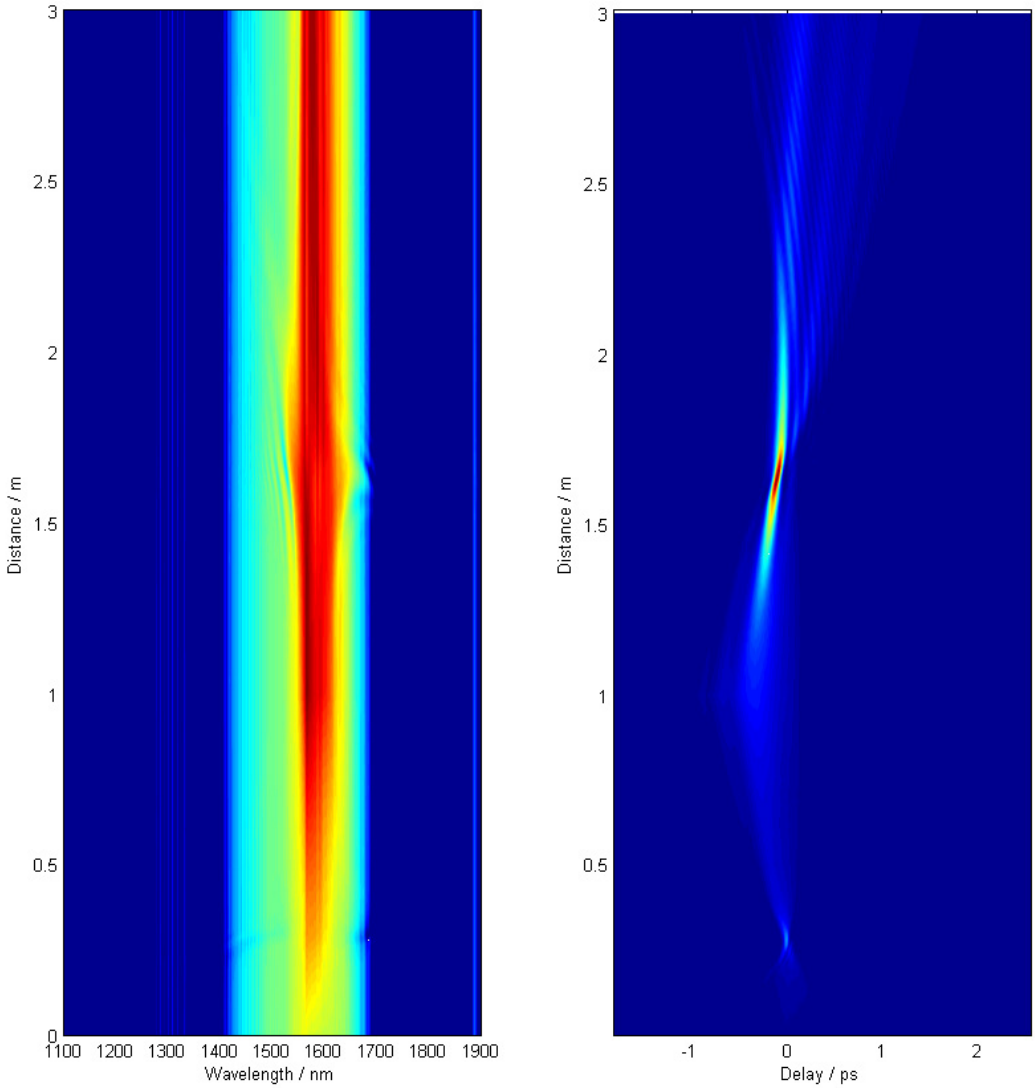

Figure 53 Full split-step integrator-based GNLSE solution for amplification in normal dispersion fiber followed by compression in polarization-maintaining PANDA 1550 fiber. Launched pulse has 140 pJ pulse energy (35 mW at 250 MHz) with optical spectrum and chirp measured by frequency-resolved optical gating. The gain fiber length is 1 m with distributed gain sufficient to give 1.6 nJ output pulse energy, and the spectral dependence of the gain spectrum of Er:fiber is taken into account. The pulse has initial anomalous chirp, and initial compression of pulse can be seen after approximately 25 cm of gain fiber. Amplification and normal dispersion end after 1 m, and the gain-less PM compression fiber properties are applied for lengths 1—3 m.

matches experiment, see Figure 54. The quality of the match, and the fact that good agreement between theory and model is achieved only by including the nonlinearity of the gain fiber, together indicate that the important

dynamics are accounted for in the split-step integrator with a fixed gain envelope. It is hoped that this result, as well as the fiber parameters reported in this chapter, will expedite the design of other ultrafast nonlinear fiber-optic systems.

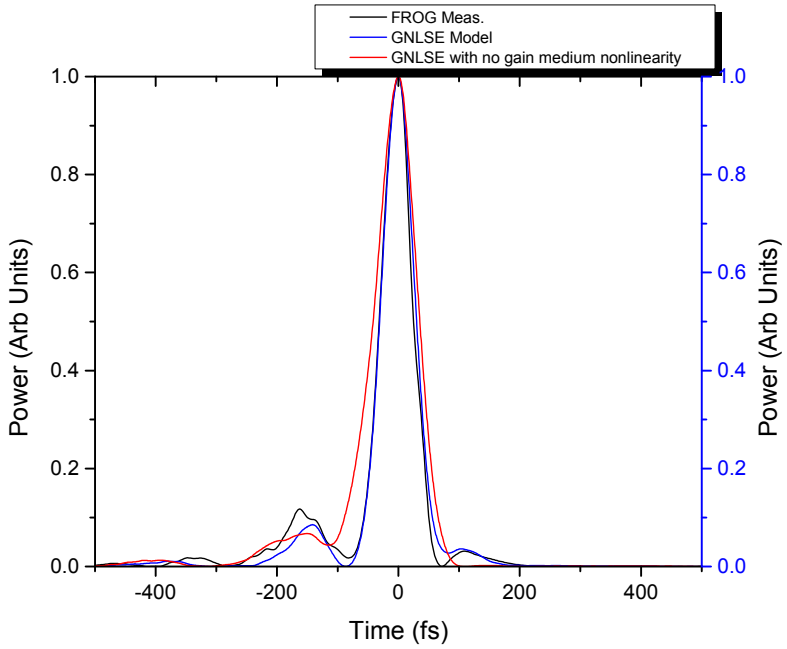

Figure 54 Comparison of measured pulse at minimum temporal duration compared to the evolution of the pulse shown in Figure 52 using the nonlinear Schrodinger equation with gain. Also shown is the model result without gain-medium nonlinearity (but with compression fiber nonlinearity.) Length of compression fiber in the experiment is 63 cm of PANDA 1550, while both model results use 61 cm of compression fiber. This length was ideal for both model runs.

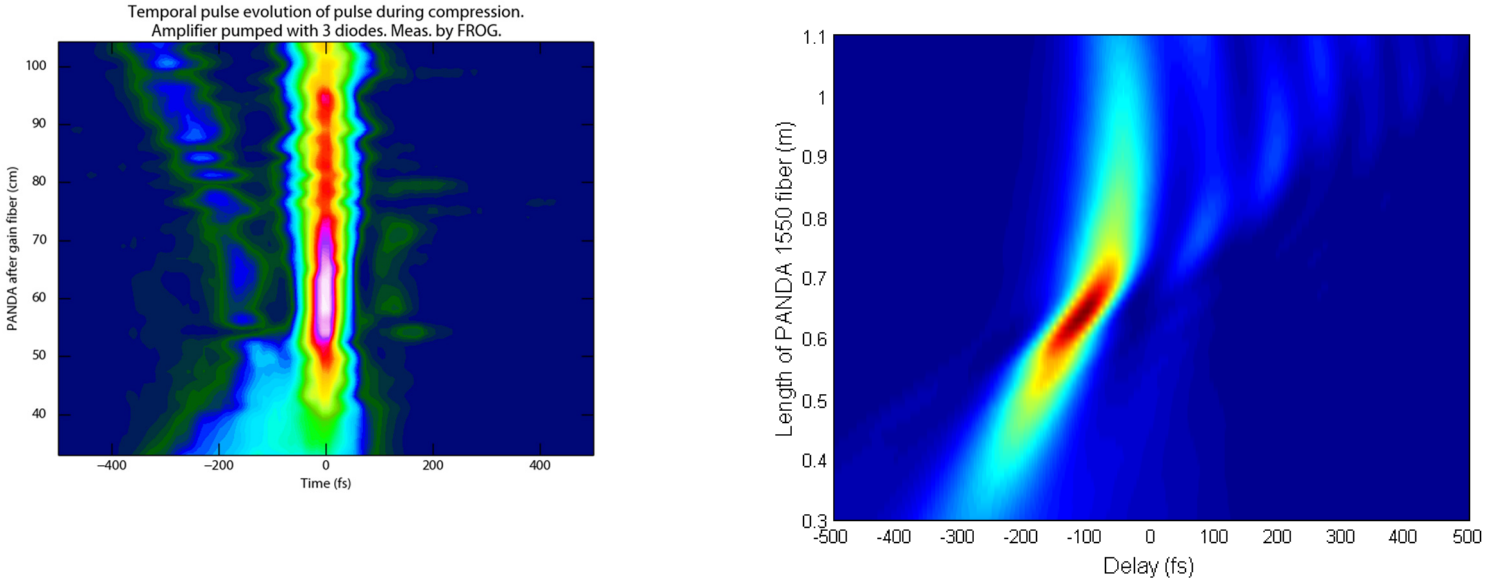

Figure 55 Left: Measured pulse intensity of 1.6 nJ pulse generated by normal-dispersion erbium fiber amplifier. Measurements are FROG retrievals over 38 cutbacks of the PANDA 1550 compression fiber. Right: Model of the same amplifier, seeded with measured pulse entering Er:fiber and assuming Er:fiber β_2=32,100 fs^2 and γ=5 W km^{-1}. Both experiment and model use 1.0 m of Er:fiber. The distortion in the model data (left) is due to a nonlinear group velocity; this is not apparent in the measurements (right) due to an alignment step in the data processing.

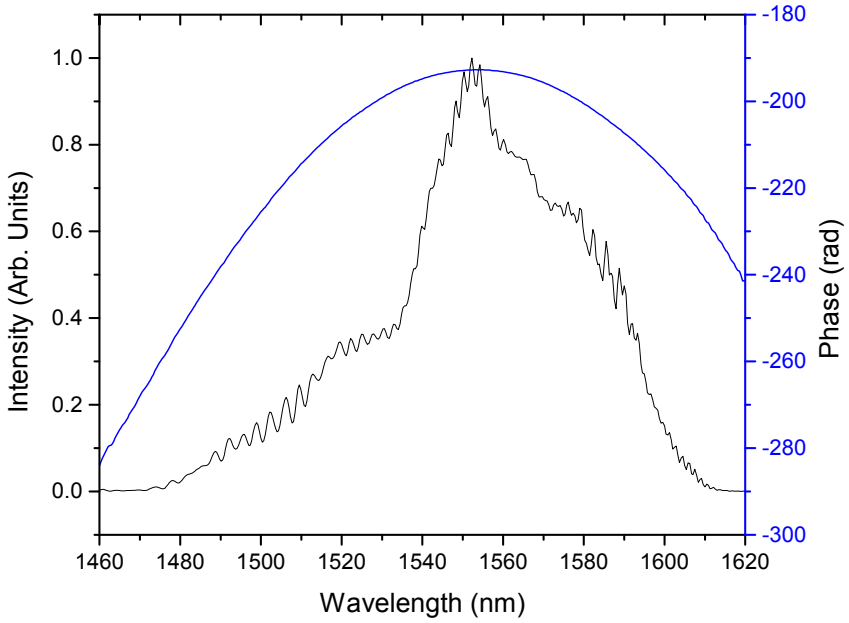

Figure 56 Optical intensity spectrum and spectral phase of pulse as it enters erbium doped gain fiber in the nonlinear normal dispersion amplifier. The chirp on the pulse was measured to be -18,000 fs^2.

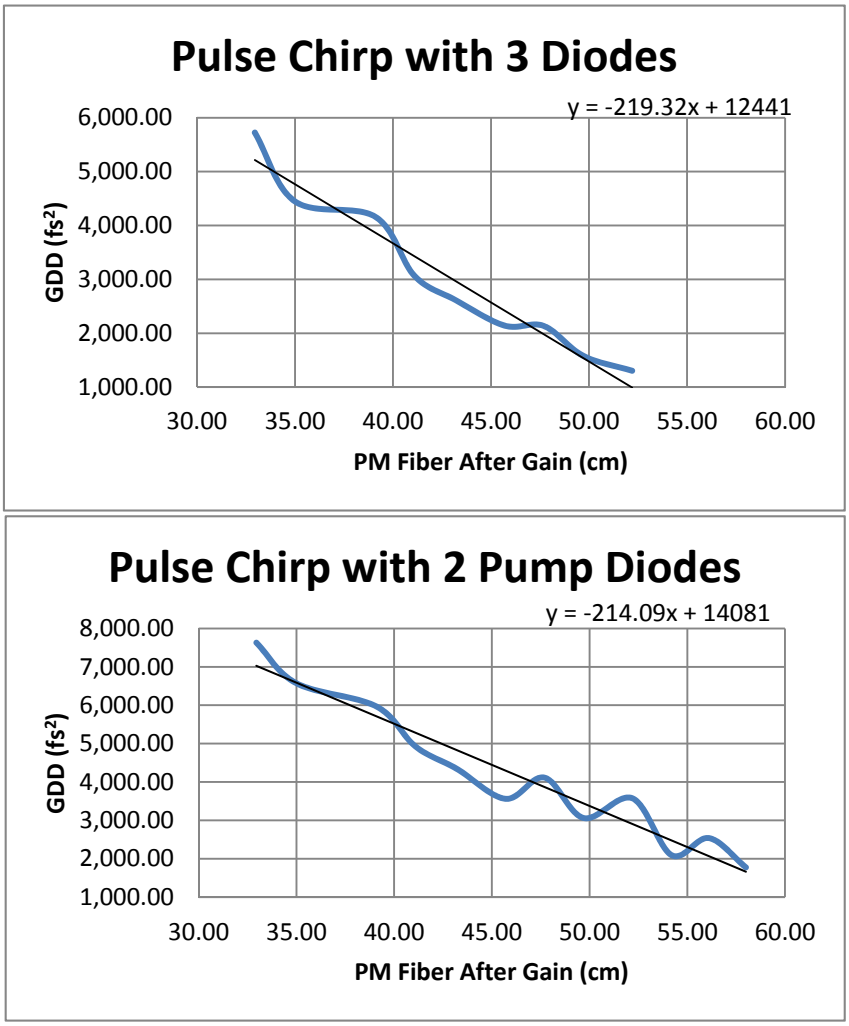

Figure 57 Group delay dispersion of the amplified 1550 nm pulse as it propagates through the PANDA fiber. GDD numbers are obtained by fitting second order polynomials to the spectral phase data retrieved by FROG. The two and three pump cases correspond to ~ 1 nJ and 1.6 nJ pulse energies.

Chapter 8

NEXT-GENERATION HIGH REPETITION RATE FREQUENCY COMB

Whereas our first generation comb was destined for an H-band spectrograph capable of resolving 12.5 GHz comb modes, the HPF calibrator will observe the Z, Y, and H bands which cover portions of the range from 820 nm to 1340 nm while requiring a comb mode-spacing of 30—45 GHz. Developing a frequency comb with the same design as the H band comb would be a major challenge due to the requirements of larger optical bandwidth and a higher repetition-frequency. At higher pulse repetition frequencies, the average power required to drive supercontinuum generation increase proportionally, and it is expected that several watts of average power would be needed to generate a 500 nm-wide, 30 GHz supercontinuum. An additional concern is the effect of four-wave mixing upon the filtered frequency comb. As was seen Chapter 5 and has been widely reported by other workers in the field [67, 14, 66], parametric gain in nonlinear fibers pumps energy from the intense comb modes into weaker ones, subverting the action of the Fabry-Perot cavities. While this effect can be minimized by use of several high finesse cavities, a very careful measurement of each comb mode is required to verify that all suppressed modes are, in fact, too weak to skew the calibration.

For our next-generation system, we consider an alternative scheme which places supercontinuum generation before the Fabry-Perot cavities, thus avoiding the side-mode amplification problem altogether. This topology was, in fact, one of the first ideas suggested for generating a broad-band frequency comb. To achieve an optical bandwidth greater than the mirror-dispersion limit, this design envisions multiple filter-cavities

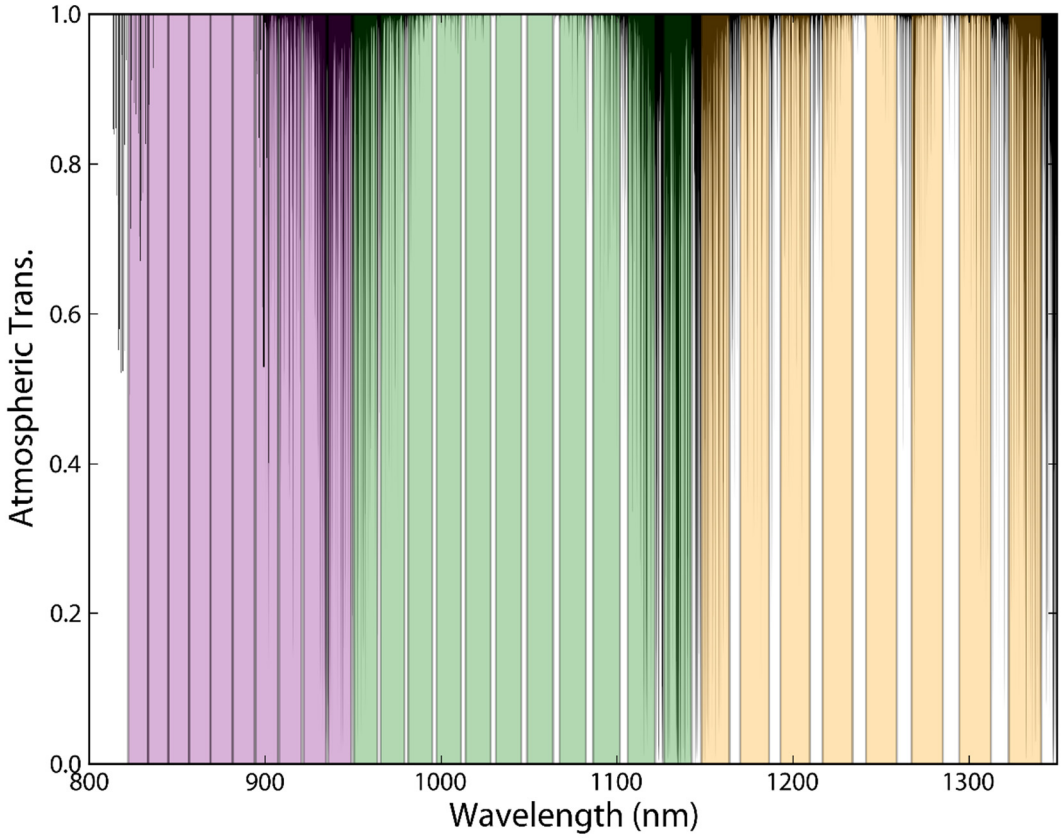

Figure 58 Atmospheric transmission (black) coverage of HPF spectrograph (shaded rectangles).

working in parallel to filter a very broad spectrum [11]. While this idea was not particularly well-suited for visible wavelengths where it is important to have a continuous calibration spectrum, the near-IR is naturally broken up into a series of bands (Z,Y,J) which are each less than 150 nm broad, as can be seen in Figure 58. The strong absorption bands at 935—963 nm and 1106—1163 nm discourage the recording of a continuous spectrum, as evidenced by the gaps in the HPF spectral coverage; it is thus unnecessary for a frequency-comb calibrator to continuously span the entire 820—1320 nm wavelength range. The design for the new calibrator uses a set of three parallel filters operating in each of the Z, Y, and J bands. As a first demonstration of this technique, a filter cavity for the Y band (964—1105 nm) was designed, constructed, and tested.

The design considerations for the mirrors comprising a parallel filter cavity are quite different than for a sequential filter-and-broaden scheme used in the H band. The parallel configuration places only linear optics between the filter cavities and the spectrograph, which eliminates the possibility of parametric amplification of suppressed comb modes and permits the use of much lower finesse cavities. At the same time, whereas in the sequential cavity design the optical bandwidth is limited primarily by the gain-bandwidth of optical amplifiers, the limitation now comes from the filter cavity bandwidth. As a result of these considerations, it is therefore desirable to construct filter cavities with the minimum necessary finesse, relaxing constraints on the mirror coating and permitting larger variations in cavity dispersion. It should be noted that cavities with extended bandwidth have been fabricated by making use of two mirrors with different coatings, which together provide zero-dispersion over nearly 20 % fractional bandwidth [17]. Because of the added cost and complexity of this design, we opted instead to use a traditional low-dispersion mirror coating design for this first effort.

In order to design a mirror set, a set of design goals must be first formulated. Because the coating dispersion can only be optimized, the mirror reflectivity is most significant design choice. The lower bound on reflectivity is set by the requirement that the center-of-mass of all "bright" modes in the calibration comb be accurate to a particular level of accuracy. The HPF seeks to achieve 1 m s^{-1} precision, and this same level, fractionally 3×10^{-9}, is chosen as the comb accuracy goal. To make this criterion concrete, "bright" comb modes are defined where the cavity transmits at above 5 % efficiency. Putting these together, the concise requirement is that for **all** comb modes with **better** than 5 % transmission, the comb-mode center of mass will be **within** 3×10^{-9} of the central mode frequency.

The calculation for the center-of-mass shift induced by a filter cavity is simple. The transmission function of the Fabry-Perot was derived earlier, see Eq. (3.14), and for two identical mirrors is

$$T(\omega) = \frac{\left(1-R\right)^2}{\left(1-R\right)^2 + 4R\sin^2\left(\left[\frac{\omega n d}{c} + \phi\right]\right)}. \tag{8.1}$$

For this calculation we will consider only a single resonance offset be some frequency shift, and it is appropriate to neglect the phase shift ϕ. When the phase is insignificant, the cavity transfer function is perfectly periodic and the center of mass calculation can be performed around any cavity resonance. The resonances around 0 Hz are simplest to work with, and the center-of-mass calculation is simply

$$\delta f = \sum_{n=-N}^{N} T\left(2\pi\left(n \times f_{rep} + \Delta f_{\text{comb-cavity}}\right)\right), \tag{8.2}$$

where N is the half-filter factor equal to $c\ /\ (4df_{rep})$ and $\Delta f_{\text{comb-cavity}}$ is the frequency offset between the comb modes and the cavity resonance. While in a real cavity this shift is due to the combined effects of higher-order dispersion, for the tolerance calculation it is simply a frequency value. To translate from an absolute to a relative frequency shift, δf is simply divided by the optical frequency, here 300 THz.

In the simplest case, each parallel branch would use only a single filter cavity, as opposed to several identical stacked filter cavities. Using the constraints above and numerically evaluating Eq. (8.2), it is clear that a reflectivity of greater than 99.84 % is required, as can be seen in Figure 59. Unfortunately, it is not possible to manufacture extremely broad-band mirrors with such a high reflectivity, and as a result it is necessary to consider a Y band filter using two cascaded cavities. Adding a second cavity effectively squares the attenuation, and as a result mirrors with 99.48 % reflectivity are sufficient to meet the design requirements.

The design and fabrication of low-dispersion mirrors is not trivial, and the mirror design was carried out in conjunction with Advanced Thin Films. In the design processes, the mirror reflectivity was reduced to 99.4 % in order to minimize the effects of dispersion. After a series of back-and-forth refinements for the coating performance, Advanced Thin Films provided not only the nominal design performance for both reflectivity and

dispersion of the mirrors, but also tolerance data which took the effects of random manufacturing errors into account. These data were analyzed using a series of numerical models for the cavity, the results of which are shown in Figure 60. As the figure indicates, in the ideal case the cavity performance should be excellent across the entire Y band and even in the worst-case it would provide comb-modes across the band.

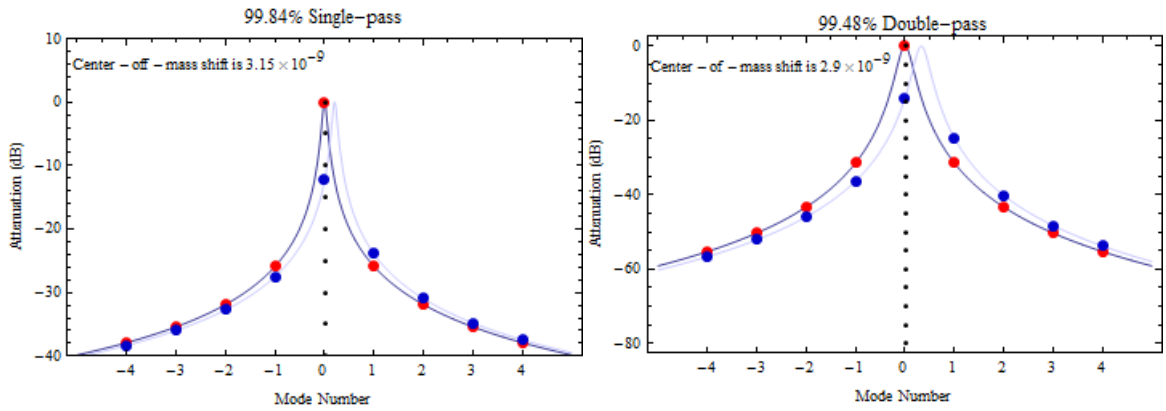

Figure 59 Left: calculated center-of-mass shift for cavity built using 99.84 % reflective mirrors at the 5 % transmission point. Right: Shift for two cascaded 99.48 % mirrors at the 5 % transmission point. In each figure the red points show the attenuation of the comb modes when there is zero offset between the cavity and comb, while blue points show the suppression when the cavity has walked off to the 5 % transmission point. The dotted black line indicates the center-of-mass of the cavity-filtered comb.

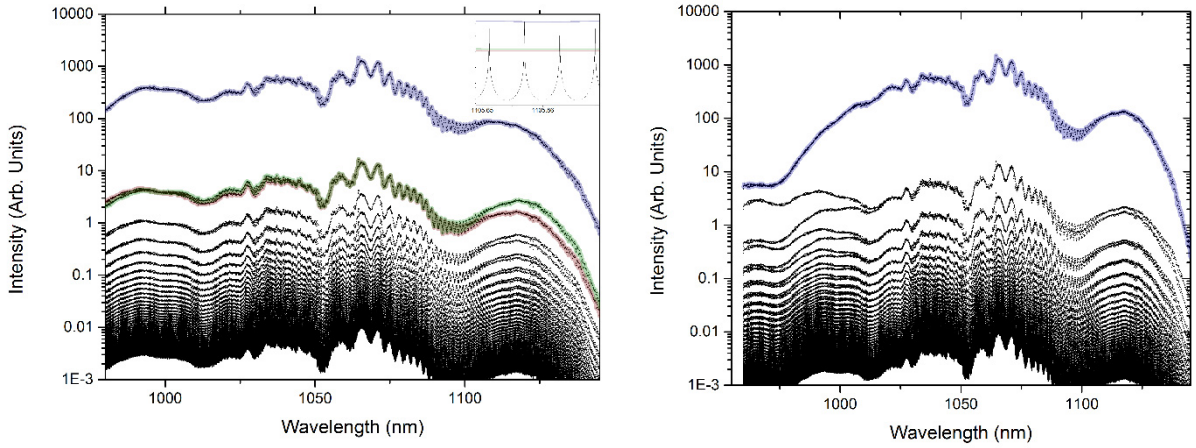

Figure 60 Left: Performance of Fabry-Perot cavity constructed using nominal (error-free) mirror performance. Excellent performance is expected from 960—1120 nm. Red, green, and blue highlights indicate groups of modes spaced by the cavity FSR. Right: Performance under worst-case error (1 % layer thickness errors conspiring for the worst result.) In this numerical model, the FSR is 30 GHz, the mode-spacing of the comb is 250 MHz, and the cavity length is locked to the resonant peak at 1064 nm which gives optimum over-all transmission of the comb for all wavelengths. This simulates the locking of the cavity to the comb via PDH.

Cavity built using Y-Band Mirrors

A batch of mirrors was fabricated using this design, with a large variety of 0.5 " mirror substrates. This selection of substrates allows higher order transverse cavity modes to be suppressed for a wide variety of cavity free spectral ranges. Using two of these mirrors, a cavity with FSR of 30 GHz was assembled using the same optomechanical design as the H band cavities. To facilitate the characterization of the cavities, the cavity was locked to a continuous-wave laser via the Pound-Driver-Hall technique. This CW laser was itself locked to a comb-mode using an AOM to allow variable offset, including zero offset, between the CW laser and the comb. The CW laser apparatus is shown in Figure 61.

The performance of the filter cavity is shown in Figure 62, and is not as broad as the design goal. While good performance is achieved from 970—1080 nm, at wavelengths above 1080 nm the cavity modes quickly become misaligned with the comb modes. This is indicative of excess dispersion. While initially it was suspected that this dispersion could be a result of air dispersion, experiments in which the cavity was purged with dry N_2, as well as a calculation of the dispersion of air, confirm that dispersion of the magnitude seen can only be due to the cavity's mirrors.

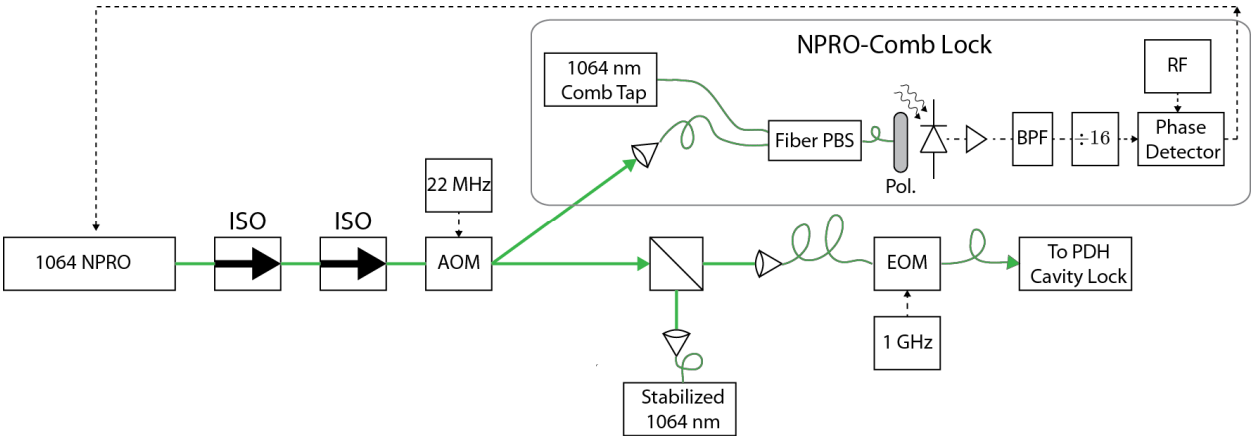

Figure 61 Diagram of the 1064 nm laser used as in this chapter. An acousto-optic modulator (AOM) is used to frequency shift a portion of the laser's output. This frequency shifted light is optically heterodyned with the laser frequency comb and the beat note is used to lock the NPRO laser to the comb. The remainder of the light is split two ways, with one portion used for diagnostics and the other portion phase modulated with a travelling-wave electro-optic modulator (EOM) to produce 1 GHz side-bands for filter cavity locking using the Pound-Driver-Hall technique.

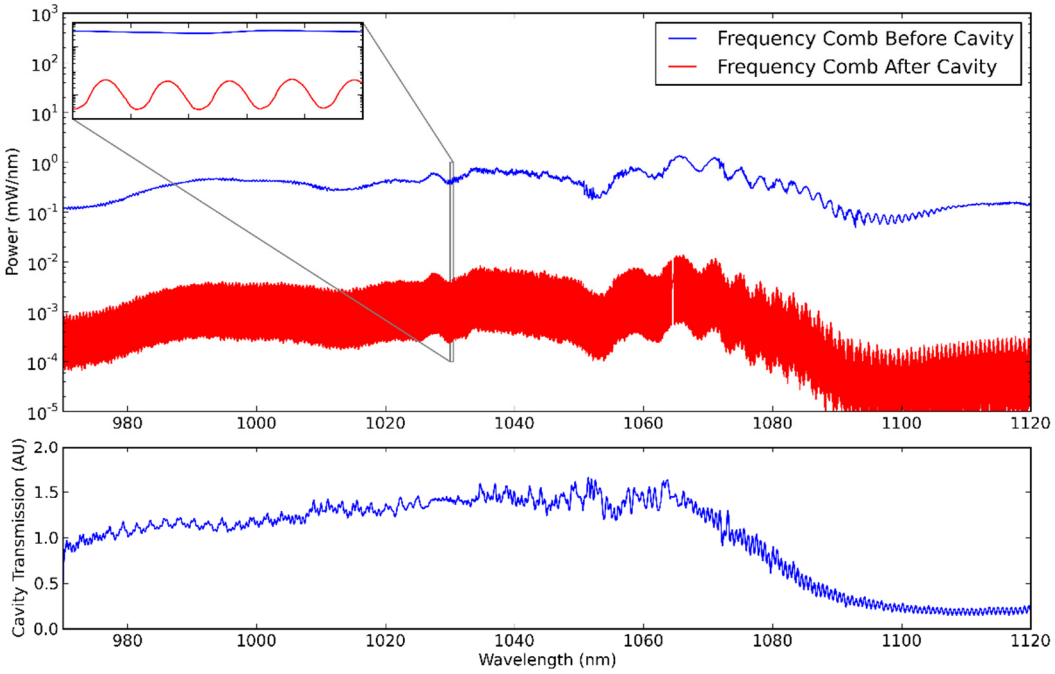

Figure 62 Filtering using 30 GHz Y-band filter cavity using 99.4 % reflective low-dispersion mirrors. Top: Optical spectrum of laser frequency comb before and after filter cavity. Bottom: (Scaled) ratio of comb modes after cavity to power entering cavity. Note the severe decrease in efficiency at 1080 nm, indicating the walk-off of comb and cavity modes. For these experiments, the Fabry-Perot cavity was locked with zero offset to an optimal comb-mode at 1064 nm via PDH.

Measurement of Mirror Dispersion

The next step after the disappointing initial results from filter cavities built with the 980—1120 nm mirror set is to fully characterize the phase and reflectivity properties of the mirror coating. Most important is an explanation for the discrepancy in predicted and actual performance of the cavity at 1112 nm, which will be of use when choosing future coating designs. While the lack of readily available CW lasers between 1064 nm and 1112 nm prohibits the use of heterodyne measurements to perform characterization, it is possible to completely measure the mirror reflectivity and dispersion by use of a Fabry-Perot cavity and comb.

The idea of using a laser frequency comb and resonant cavity to characterize the cavity dispersion is not a new one, and several schemes have been developed for characterizing mirror dispersion [88, 76, 49]. While in each case the frequency comb is used to measure the positions of the mirror resonances, the scheme implemented here stabilizes the cavity to a CW laser, then scans the cavity by variation of the laser frequency [49].

Using the mirrors under test, a Fabry-Perot cavity is constructed with FSR equal to some multiple m of the mode-locked laser repetition frequency f_{rep}. Light from the frequency comb and a comb-referenced CW

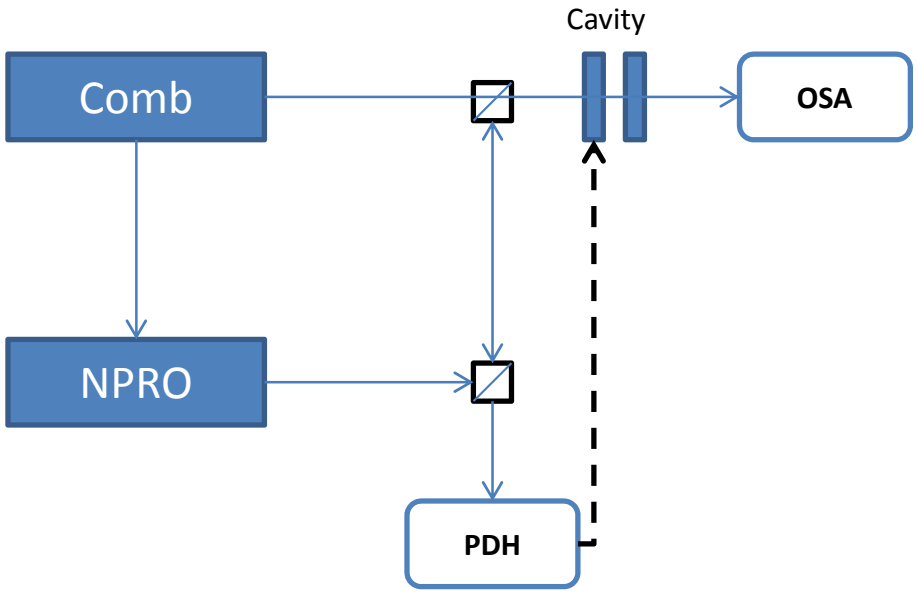

Figure 63 Schematic of mirror dispersion measurement. The NPRO laser is locked with tunable offset to a frequency comb mode; the Fabry-Perot cavity length is stabilized using PDH to this laser. The comb, which is only locked to the cavity via the NPRO laser, is simultaneously coupled into the cavity. An optical spectrum analyzer (OSA) records the transmitted comb spectrum with 0.02 nm resolution.

laser are combined and launched into the cavity. Using the Pound-Drever-Hall scheme, the length of the cavity is stabilized to the CW laser. The light transmitted by the cavity is sent to the spectrometer, which measures the cavity transmission function

(8.3) $$T(f;d),$$

where d is the cavity's length and the frequency $f = m \times FSR + f_0$. A schematic of the measurement scheme is shown in Figure 63. To determine the cavity's finesse $F(f)$ and phase $\phi(f)$, these measurements are repeated as the cavity length d is scanned by tuning the CW laser frequency.

To interpret the experimental results, the relationship between the cavity transmission function, cavity finesse, and cavity dispersion must be derived. The experiment here is similar to the one described in Li, 2010 [49], and the derivation below follows this reference closely. The cavity transmission function was derived in Chapter 3, and in the case of a cavity constructed using two identical mirrors it simplifies to

(8.4) $$T(\omega;d) = \frac{\big(1 - R(\omega)\big)^2}{\big(1 - R(\omega)\big)^2 + 4R(\omega)\sin^2\left(\frac{1}{2}\left[\frac{2\omega n d}{c} + 2\phi(\omega)\right]\right)}.$$

In the measurement described above, the cavity length d is referenced to a CW laser, and the relationship between the variation in laser frequency and cavity length must be derived. For arbitrary ω, the resonance condition is

(8.5) $$m \times \pi = \frac{\omega n d}{c} + \phi(\omega),$$

and, solving for d, the cavity length is

(8.6) $$d = \frac{c}{n\omega}\big(m\pi + \phi(\omega)\big).$$

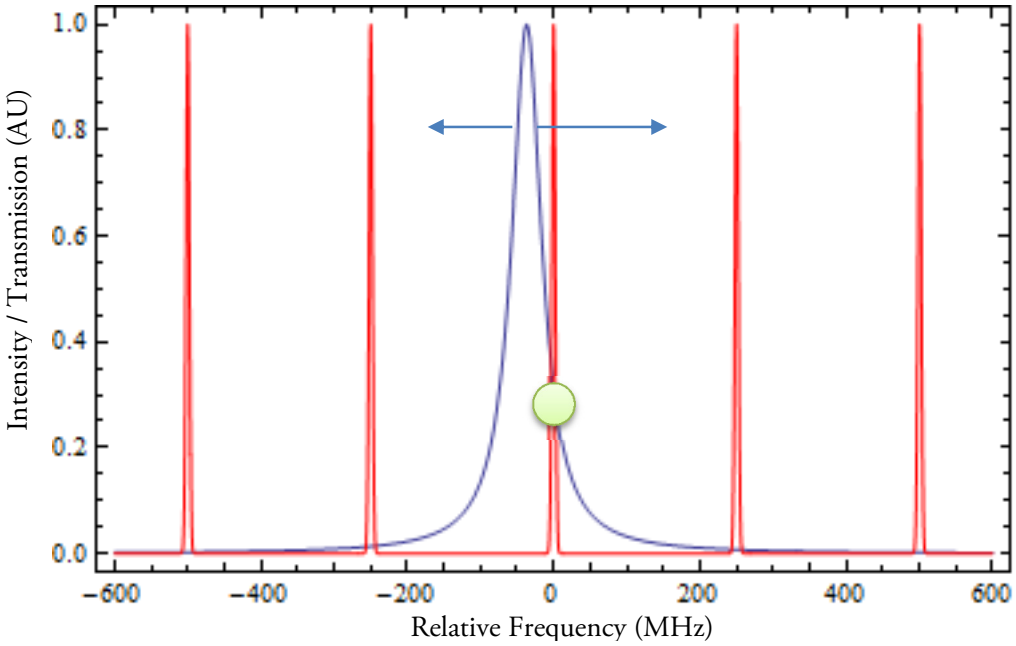

Figure 64 Diagram of cavity dispersion measurement. The transmission of the comb lines (red) as attenuated by the filter cavity (blue) is recorded as the cavity mode is shifted. The variation in the amount of light transmitted (green) provides information about the width of the cavity resonance and its offset relative to the laser frequency comb.

In the experiment, the cavity length is varied by changing the frequency of the m^{th} cavity resonance, where m is the index of the resonance originally nearest the CW laser. Holding m fixed, the cavity length d can be expanded in a power series with respect to ω, of which the leading term is:

$$\delta d = \frac{c}{n\omega^2}\left(\omega\frac{\partial\phi}{\partial\omega} - m\pi - \phi(\omega)\right)\delta\omega. \tag{8.7}$$

The mirror dispersion is assumed to be low and as a result will not significantly affect the position of the cavity transmissions for small changes $\delta\omega < FSR$. This assumption allows the derivative term to be dropped, and making the obvious substitution the expression simplifies to

$$\delta d = -\frac{1}{\omega_0} d(\omega_0)\delta\omega, \tag{8.8}$$

Where, to very good approximation, the length is determined by the cavity FSR,

$$d(\omega_0) = \frac{c}{2FSR}. \tag{8.9}$$

Combining these expressions and noting that $\delta\omega \,/\, \omega = \delta f \,/\, f,$ the change in cavity length is given by

$$\delta d = -\frac{c}{2FSR \times f_{\mathrm{CW}}}\delta f. \tag{8.10}$$

This expression is in fact all that is required for analysis of the data. The function $T\big(\omega; d(\delta f)\big)$ is measured experimentally as δf is swept between $\pm FSR,$ and by applying (8.4) the parameters R and ϕ can be determined for each cavity resonance, as shown in Figure 65.

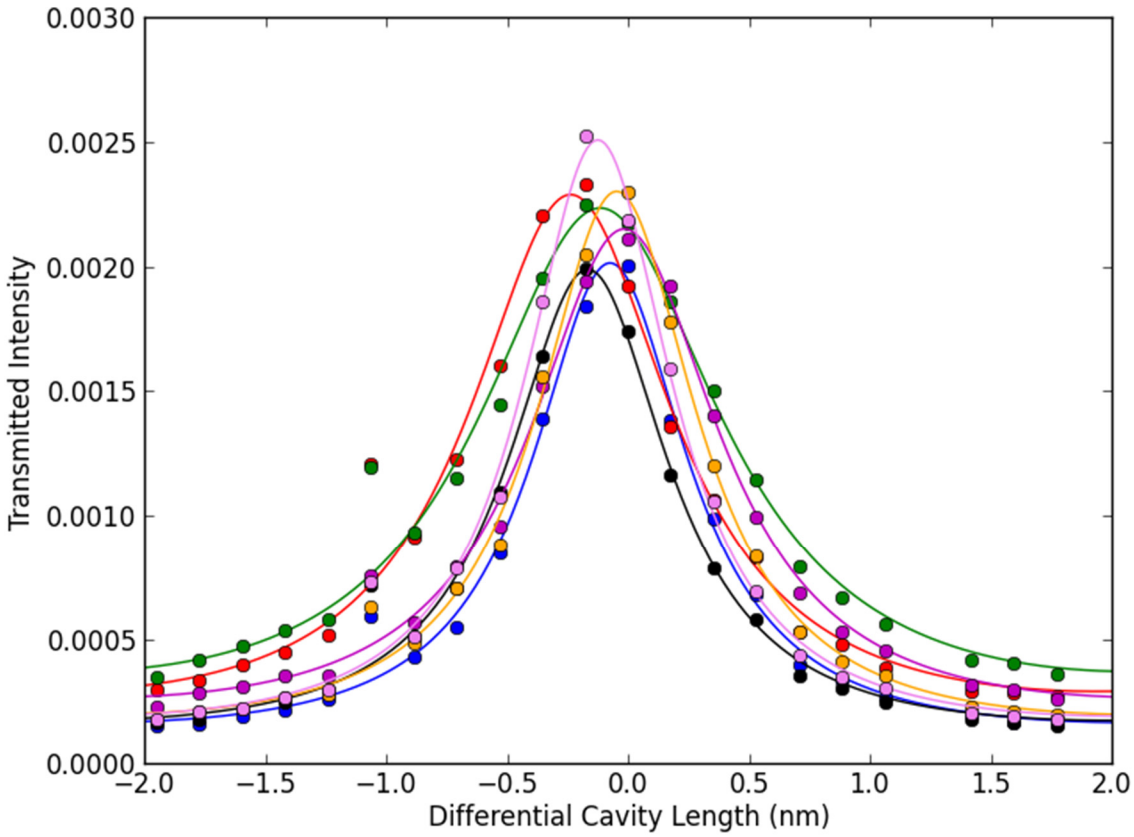

Figure 65 Data (points) and fit for 6 cavity modes near 1032 nm. Free parameters in the fit are the Fabry-Perot cavity finesse, cavity dispersion, and frequency-comb mode intensity.

Experiment and Results

Using the scheme described above and stepping the CW laser frequency in 10 MHz increments, the finesse and dispersion of the mirrors are calculated for each of the 1500 cavity modes between 980—1150 nm. The fit results are presented in Figure 67.

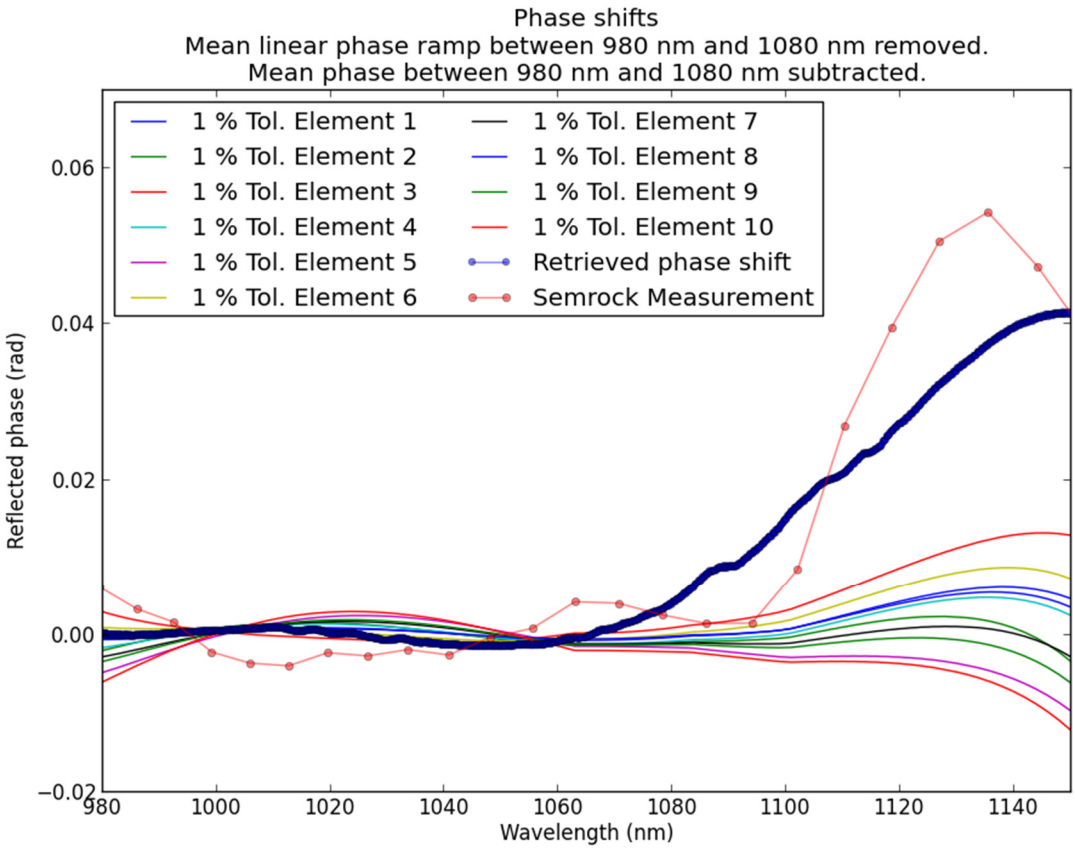

Figure 66 Comparison of relative phase shift of 99.4 % cavity mirrors.

With a measurement of the dispersion of the cavity mirrors, several calculations can be made which shed light on the apparently narrow cavity bandwidth. Using the measured dispersion and reflectivity data, the Fabry-Perot model cavity model can be used to calculate the effect of the mirrors on the frequency comb. The model output is shown in Figure 68, where the cavity can be seen to roll off at approximately 1080 nm. In fact, the dispersion is so great that the cavity modes and comb modes are offset by f_{rep} / 2 at 1100 nm. A direct comparison of the experimentally measured and modeling fractional cavity transmission can also be made, shown in Figure 68. The agreement between the model and experiment is very good, which is significant given

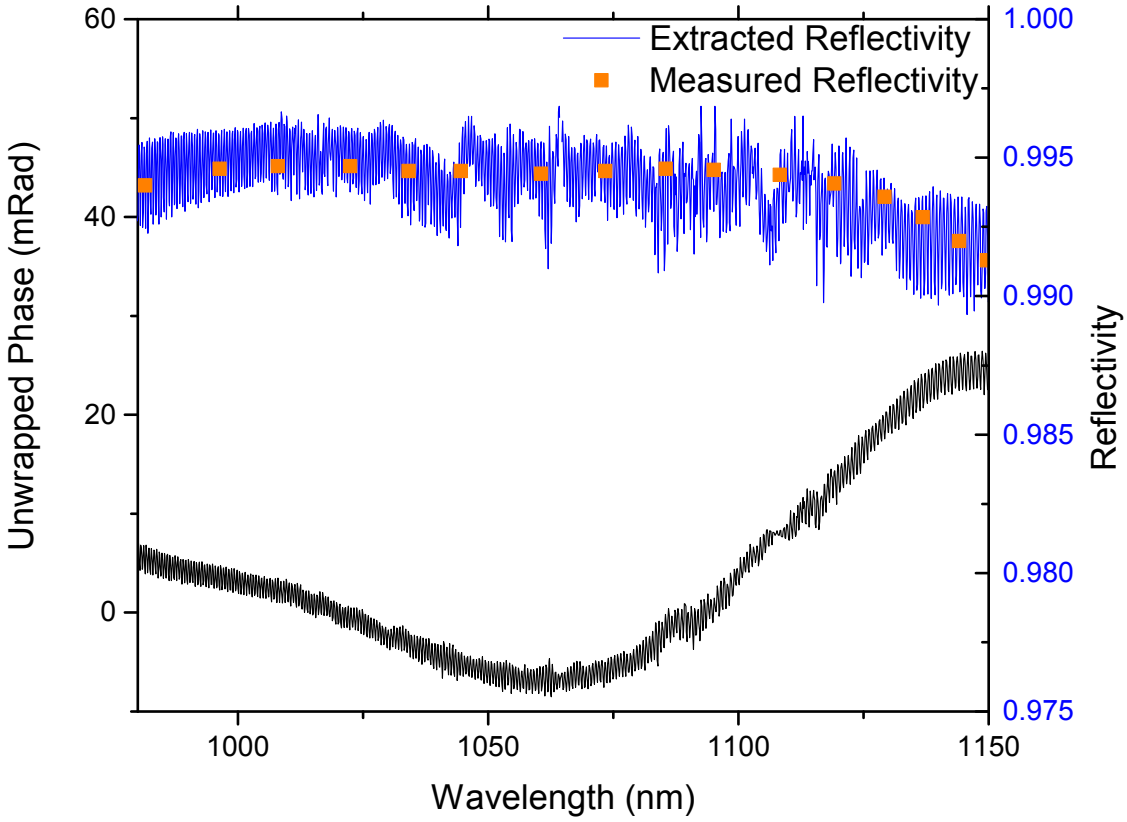

Figure 67 Cavity reflectivity and phase shifts as determined by fitting swept-cavity measurement. The high-frequency oscillations seem to be caused by an etalon effect somewhere in the measurement system and are not related to the spectrometer resolution. The good agreement between the reflectivity determined by the fit (blue) and the reflectivity as measured by a standard spectrometer (orange) provides confidence in the measurement.

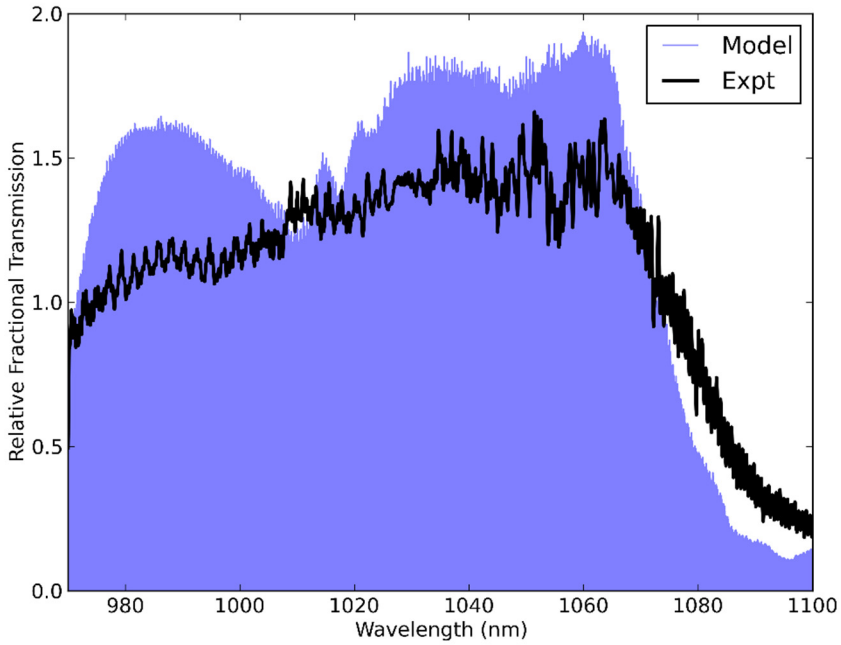

Figure 68 Comparison of measured and modeled cavity transmission as function of wavelength. In both experiment and model, cavity length is set to maximize transmission of the ~ 1064 nm mode which allows maximum transmission of the comb.

the independence of experiment, which measures the cavity transmission function with no adjustable parameters. Agreement between the measured reflectivity data indicates successful extraction of the cavity line width, and this result provides validation of both the model and dispersion measurement.

These results lead to the disappointing conclusion that it may not be practical to reliably fabricate mirrors that are capable of filtering more than ~ 100 nm of simultaneous bandwidth. Future filtering designs will have to take this into account, either by even more careful design of the coating and smaller tolerances in fabrication or by using a filtering scheme allowing for smaller filter-bandwidths,

Chapter 9

CONCLUSION

In the eight years since the first proposals for the application of frequency combs to astronomical observations, the field has grown from small-scale laboratory demonstrations to plans for permanent installations of frequency comb calibrators at a number of observatories. Our group at NIST and CU is directly involved with one such effort, and is developing a calibrator which will be installed at the Hobby-Eberly telescope within the next 5 years. Looking forward to the future of laser frequency comb calibration for astronomical spectroscopy, there are many exciting new ideas currently being developed. In addition to the techniques presented in this thesis, research is underway into calibrators based upon microresonator combs, stabilized passive Fabry-Perot etalons, and cascaded eletro-optic modulator systems. While the cosmological measurements will require the full precision of the atomically-referenced frequency comb, it is not yet clear which technology will provide the optimum balance of spectral bandwidth, brightness, and most importantly reliability for planet-finding applications.

This thesis has demonstrated the key technologies required for the development of future calibrators. By coupling the CU/NIST frequency comb system to the Penn State University *Pathfinder* spectrograph at the Hobby-Eberly telescope, we have shown that frequency combs can be used for precision calibration of astronomical spectra in the near-infrared, as well as learned valuable lessons about the rigorous reliability requirements for true facility-class instrumentation. The techniques developed herein for extending erbium fiber laser frequency combs into the visible using polarization-maintaining fiber amplifiers will have broad applications, not only to our next-generation comb for calibration of astronomical spectrographs, but also to

optical clock laser-comparisons, trace-gas detection, and broadening of micro-resonator based frequency comb systems. Using the extended erbium frequency comb, a novel broad-bandwidth filter cavity was designed and tested. While the resulting filter bandwidth was less than expected, measurements of the mirror dispersion accurately explain the behavior and indicate that achieving broad filtering bandwidth may be impractical. These lessons and technologies will be used in designing the next-generation calibrator, funded by a 5-year NST ATI grant. When installed at the Hobby-Eberly telescope, this system will support near-IR spectroscopy at new levels of precision, and will enable a search for habitable planets in close proximity to our own solar system.

REFERENCES

[1] Govind Agrawal. *Nonlinear Fiber Optics*. Academic Press, Burlington, MA, 2007.

[2] D. Anderson, M. Desaix, M. Karlsson, M. Lisak, and M. L. Quiroga-Teixeiro. Wave-breaking-free pulses in nonlinear-optical fibers. *J. Opt. Soc. Am. B*, 10(7):1185–1190, July 1993.

[3] Isabelle Baraffe and Gilles Chabrier. Mass-spectral class relationship for m dwarfs. *The Astrophysical Journal Letters*, 461(1):L51, 1996.

[4] A Baranne, D Queloz, M Mayor, G Adrianzyk, G Knispel, D Kohler, D Lacroix, JP Meunier, G Rimbaud, and A Vin. Elodie: A spectrograph for accurate radial velocity measurements. *A&AS*, 119:373–390, 1996.

[5] A. Bartels, D. Heinecke, and S. A. Diddams. Passively mode-locked 10 GHz femtosecond Ti:sapphire laser. *Opt. Lett.*, 33(16):1905–1907, 2008.

[6] J. Baudrand and G. A. H. Walker. Modal Noise in High-Resolution, Fiber-fed Spectra: A Study and Simple Cure. *PASP*, 113:851–858, July 2001.

[7] Jacob L. Bean, Andreas Seifahrt, Henrik Hartman, Hampus Nilsson, G?nter Wiedemann, Ansgar Reiners, Stefan Dreizler, and Todd J. Henry. The crires search for planets around the lowest-mass stars. i. high-precision near-infrared radial velocities with an ammonia gas cell. *The Astrophysical Journal*, 713(1):410, 2010.

[8] Andrew J. Benedick, Guoqing Chang, Jonathan R. Birge, Li-Jin Chen, Alexander G. Glenday, Chih-Hao Li, David F. Phillips, Andrew Szentgyorgyi, Sylvain Korzennik, Gabor Furesz, Ronald L. Walsworth, and Franz X. Kärtner. Visible wavelength astro-comb. *Opt. Express*, 18(18):19175–19184, Aug 2010.

[9] F Bouchy, F Pepe, and D Queloz. Fundamental photon noise limit to radial velocity measurements. *ASTRONOMY AND ASTROPHYSICS-BERLIN-*, 374(2):733–739, 2001.

[10] Robert W. Boyd. *Nonlinear Optics*. Academic Press, 2008.

[11] D. A. Braje, M. S. Kirchner, S. Osterman, T. Fortier, and S. A. Diddams. Astronomical spectrograph calibration with broad-spectrum frequency combs. *Eur. Phys. J. D*, 48:57–66, jun 2008.

[12] R. Paul Butler, Timothy R. Bedding, Hans Kjeldsen, Chris McCarthy, Simon J. O???Toole, Christopher G. Tinney, Geoffrey W. Marcy, and Jason T. Wright. Ultra-high-precision velocity measurements of oscillations in ?? centauri a. *The Astrophysical Journal Letters*, 600(1):L75, 2004.

[13] R Paul Butler, Geoffrey W Marcy, Eric Williams, Chris McCarthy, Preet Dosanjh, and Steven S Vogt. Attaining doppler precision of 3 ms. *Publications of the Astronomical Society of the Pacific*, pages 500–509, 1996.

[14] Guoqing Chang, Chih-Hao Li, David F. Phillips, Ronald L. Walsworth, and Franz X. Kärtnerm. Toward a broadband astro-comb: effects of nonlinear spectral broadening in optical fibers. *Opt. Express*, 18(12):12736–12747, 2010.

[15] Hung-Wen Chen, J Lim, Shu-Wei Huang, Damian N Schimpf, Franz X Kärtner, Guoqing Chang, et al. Optimization of femtosecond yb-doped fiber amplifiers for high-quality pulse compression. *Opt. Express20 (27)*, pages 28672–28682, 2012.

[16] J. Chen, J. W. Sickler, P. Fendel, E. P. Ippen, F. X. Kärtner, T. Wilken, R. Holzwarth, and T. W. Hänsch. Generation of low-timing-jitter femtosecond pulse trains with 2 GHz repetition rate via external repetition rate multiplication. *Opt. Lett.*, 33:959–961, apr 2008.

[17] Li-Jin Chen, Guoqing Chang, Chih-Hao Li, Andrew J Benedick, David F Philips, Ronald L Walsworth, and Franz X Kärtner. Broadband dispersion-free optical cavities based on zero group delay dispersion mirror sets. *Optics Express*, 18(22):23204–23211, 2010.

[18] Jung-Ho Chung and Andrew M Weiner. Ambiguity of ultrashort pulse shapes retrieved from the intensity autocorrelation and the power spectrum. *Selected Topics in Quantum Electronics, IEEE Journal of*, 7(4):656–666, 2001.

[19] Sumner P Davis, Mark C Abrams, and James W Brault. *Fourier transform spectrometry*. Access Online via Elsevier, 2001.

[20] S. T. Dawkins, J. J. Mcferran, and A. N. Luiten. Considerations on the measurement of the stability of oscillators with frequency counters. *IEEE Trans. Ultrason., Ferroelectr., Freq. Control*, 54(5):918–925, 2007.

[21] S De Silvestri, P Laporta, and O Svelto. Analysis of quarter-wave dielectric-mirror dispersion in femtosecond dye-laser cavities. *Optics letters*, 9(8):335–337, 1984.

[22] R. W. P. Drever, J. L. Hall, F. V. Kowalski, J. Hough, G. M. Ford, A. J. Munley, and H. Ward. Laser phase and frequency stabilization using an optical resonator. *Applied Physics B: Lasers and Optics*, 31(2):97–105, jun 1983.

[23] John M. Dudley, Christophe Finot, David J. Richardson, and Guy Millot. Self-similarity in ultrafast nonlinear optics. *Nat Phys*, 3(9):597–603, September 2007.

[24] John M Dudley and James Roy Taylor. *Supercontinuum generation in optical fibers*. Cambridge University Press, 2010.

[25] V. A. Dzuba, V. V. Flambaum, and J. K. Webb. Space-time variation of physical constants and relativistic corrections in atoms. *Phys. Rev. Lett.*, 82(5):888–891, February 1999.

[26] F. Grupp. The nature of the fiber noise with the foces spectrograph. *A&A*, 412(3):897–902, 2003.

[27] M. E. Fermann, V. I. Kruglov, B. C. Thomsen, J. M. Dudley, and J. D. Harvey. Self-similar propagation and amplification of parabolic pulses in optical fibers. *Phys. Rev. Lett.*, 84(26):6010–6013, June 2000.

[28] ME Fermann, MJ Andrejco, Y Silberberg, and ML Stock. Passive mode locking by using nonlinear polarization evolution in a polarization-maintaining erbium-doped fiber. *Optics letters*, 18(11):894–896, 1993.

[29] C Randy Giles and Emmanuel Desurvire. Modeling erbium-doped fiber amplifiers. *Lightwave Technology, Journal of*, 9(2):271–283, 1991.

[30] Herbert Goldstein. *Classical Mechanics*. Addison-Wesley, 1950.

[31] Alexander M Heidt, Alexander Hartung, Gurthwin W Bosman, Patrizia Krok, Erich G Rohwer, Heinrich Schwoerer, and Hartmut Bartelt. Coherent octave spanning near-infrared and visible supercontinuum generation in all-normal dispersion photonic crystal fibers. *Optics Express*, 19(4):3775–3787, 2011.

[32] M. Hirano, T. Nakanishi, T. Okuno, and M. Onishi. Silica-based highly nonlinear fibers and their application. *IEEE J. Sel. Top. Quantum Electron.*, 15(1):103 –113, jan 2009.

[33] Philip C. D. Hobbs. *Building Electro-Optical Systems*. Wiley-Interscience, 2000.

[34] Feng-Lei Hong, Kaoru Minoshima, Atsushi Onae, Hajime Inaba, Hideyuki Takada, Akiko Hirai, Hirokazu Matsumoto, Toshiharu Sugiura, and Makoto Yoshida. Broad-spectrum frequency comb generation

and carrier-envelope offset frequency measurement by second-harmonic generation of a mode-locked fiber laser. *Opt. Lett.*, 28(17):1516–1518, September 2003.

[35] Seppo Honkanen, Tomoko Ohtsuki, Shibin Jiang, S Iraj Najafi, and Nasser Peyghambarian. High er concentration phosphate glasses for planar waveguide amplifiers. In *Photonics West'97*, pages 32–40. International Society for Optics and Photonics, 1997.

[36] Paul Horowitz and Winfield Hill. *The Art of Electronics*. Cambridge, 1989.

[37] Edwin Hubble. A relation between distance and radial velocity among extra-galactic nebulae. *Proceedings of the National Academy of Sciences*, 15(3):168–173, 1929.

[38] William Huggins. Further observations on the spectra of some of the stars and nebulae, with an attempt to determine therefrom whether these bodies are moving towards or from the earth, also observations on the spectra of the sun and of comet ii., 1868. *Philosophical Transactions of the Royal Society of London*, 158:529–564, 1868.

[39] David J. Jones, Scott A. Diddams, Jinendra K. Ranka, Andrew Stentz, Robert S. Windeler, John L. Hall, and Steven T. Cundiff. Carrier-envelope phase control of femtosecond mode-locked lasers and direct optical frequency synthesis. *Science*, 288(5466):635–639, 2000.

[40] D. J. Kane and R. Trebino. Characterization of arbitrary femtosecond pulses using frequency-resolved optical gating. *IEEE J Quantum Electron*, 29(2):571–579, 1993.

[41] D. Kielpinski, M. G. Pullen, J. Canning, M. Stevenson, P. S. Westbrook, and K. S. Feder. Mode-locked picosecond pulse generation from an octave-spanning supercontinuum. *Opt. Express*, 17(23):20833–20839, November 2009.

[42] K. Kieu, R. J. Jones, and N. Peyghambarian. High power femtosecond source near 1 micron based on an all-fiber er-doped mode-locked laser. *Opt. Express*, 18(20):21350–21355, September 2010.

[43] Yunseok Kim, Young-Jin Kim, Seungman Kim, and Seung-Woo Kim. Long-term reliable phase-locked seed source for yb-fiber-based chirped pulse amplification. In *Proc. Conf. Lasers and Electro-Optics*, page FD7. Optical Society of America, 2010.

[44] M. S. Kirchner, D. A. Braje, T. M. Fortier, A. M. Weiner, L. Hollberg, and S. A. Diddams. Generation of 20 GHz, sub-40 fs pulses at 960 nm via repetition-rate multiplication. *Opt. Lett.*, 34:872–874, mar 2009.

[45] Maciej Konacki. Precision radial velocities of double-lined spectroscopic binaries with an iodine absorption cell. *The Astrophysical Journal*, 626(1):431, 2005.

[46] Ravi Kumar Kopparapu. A revised estimate of the occurrence rate of terrestrial planets in the habitable zones around kepler m-dwarfs. *The Astrophysical Journal Letters*, 767(1):L8, 2013.

[47] Ming Lai, Shui T. Lai, and Casimir Swinger. Single-grating laser pulse stretcher and compressor. *Appl. Opt.*, 33(30):6985–6987, October 1994.

[48] Chih-Hao Li, Andrew J. Benedick, Peter Fendel, Alexander G. Glenday, Franz X. Kartner, David F. Phillips, Dimitar Sasselov, Andrew Szentgyorgyi, and Ronald L. Walsworth. A laser frequency comb that enables radial velocity measurements with a precision of 1 cm s^{-1}. *Nature*, 452(7187):610–612, April 2008.

[49] Chih-Hao Li, Alexander G Glenday, Andrew J Benedick, Guoqing Chang, Li-Jin Chen, Claire Cramer, Peter Fendel, Gabor Furesz, Franz X K??rtner, and Sylvain Korzennik. In-situ determination of astro-comb calibrator lines to better than 10 cm s (-1). *Opt. Express*, 18(12):13239–13249, 2010.

[50] Peng Li, Guizhong Wang, Chen Li, Aimin Wang, Zhigang Zhang, Fei Meng, Shiying Cao, and Zhanjun Fang. Characterization of the carrier envelope offset frequency from a 490 mhz yb-fiber-ring laser. *Optics Express*, 20(14):16017–16022, 2012.

[51] C Lovis and F Pepe. A new list of thorium and argon spectral lines in the visible. *arXiv preprint astro-ph/0703412*, 2007.

[52] Christophe Lovis and D Fischer. Radial velocity techniques for exoplanets. *Exoplanets*, page 27, 2010.

[53] Geoffrey W Marcy and R Paul Butler. Precision radial velocities with an iodine absorption cell. *Publications of the Astronomical Society of the Pacific*, pages 270–277, 1992.

[54] M. Mayor and D. Queloz. A jupiter-mass companion to a solar-type star. *Nature*, 378:355–359, nov 1995.

[55] Donald H Menzel. The history of astronomical spectroscopy i qualitative chemical analysis and radial velocities. *Annals of the New York Academy of Sciences*, 198(1):225–234, 1972.

[56] W. Miniscalco. Erbium-doped glasses for fiber amplifiers at 1500 nm. *Lightwave Technology, Journal of*, 9(2):234–250, 1991.

[57] M. T. Murphy, T. Udem, R. Holzwarth, A. Sizmann, L. Pasquini, C. Araujo-Hauck, H. Dekker, S. D'Odorico, M. Fischer, T. W. Hänsch, and A. Manescau. High-precision wavelength calibration of astronomical spectrographs with laser frequency combs. *Mon. Not. R. Astron. Soc.*, 380:839–847, sep 2007.

[58] LE Nelson, DJ Jones, K Tamura, HA Haus, and EP Ippen. Ultrashort-pulse fiber ring lasers. *Applied Physics B: Lasers and Optics*, 65(2):277–294, 1997.

[59] Nathan R Newbury and Brian R Washburn. Theory of the frequency comb output from a femtosecond fiber laser. *Quantum Electronics, IEEE Journal of*, 41(11):1388–1402, 2005.

[60] J. W. Nicholson, A. D. Yablon, M. F. Yan, P. Wisk, R. Bise, D. J. Trevor, J. Alonzo, T. Stockert, J. Fleming, E. Monberg, F. Dimarcello, and J. Fini. Coherence of supercontinua generated by ultrashort pulses compressed in optical fibers. *Opt. Lett.*, 33(18):2038–2040, September 2008.

[61] David L. Nidever, Geoffrey W. Marcy, R. Paul Butler, Debra A. Fischer, and Steven S. Vogt. Radial velocities for 889 late-type stars. *The Astrophysical Journal Supplement Series*, 141(2):503, 2002.

[62] T. Okuno, M. Onishi, T. Kashiwada, S. Ishikawa, and M. Nishimura. Silica-based functional fibers with enhanced nonlinearity and their applications. *Selected Topics in Quantum Electronics, IEEE Journal of*, 5(5):1385 –1391, sep/oct 1999.

[63] Steve Osterman, Matthew Beasley, Cynthia Froning, Scott Diddams, Leo Hollberg, Vela Mbele, and Andrew Weiner. A proposed laser frequency comb-based wavelength reference for high-resolution specroscopy. In Daniel Coulter, editor, *Proc. of SPIE*, volume 6693, 2007.

[64] Luca Pasquini, Stefano Cristiani, Hans Dekker, Martin Haehnelt, Paolo Molaro, Francesco Pepe, Gerardo Avila, Bernard Delabre, Sandro D???Odorico, and Jochen Liske. Codex: Measuring the expansion of the universe (and beyond). *The Messenger*, 122(10), 2005.

[65] Saul Perlmutter, G Aldering, G Goldhaber, RA Knop, P Nugent, PG Castro, S Deustua, S Fabbro, A Goobar, DE Groom, et al. Measurements of and λ from 42 high-redshift supernovae. *The Astrophysical Journal*, 517(2):565, 1999.

[66] RA Probst, T Steinmetz, T Wilken, H Hundertmark, SP Stark, GKL Wong, P St J Russell, TW Hänsch, R Holzwarth, and Th Udem. Nonlinear amplification of side-modes in frequency combs. *Optics express*, 21(10):11670–11687, 2013.

[67] F. Quinlan, G. Ycas, S. Osterman, and S. A. Diddams. A 12.5 GHz-spaced optical frequency comb spanning > 400 nm for near-infrared astronomical spectrograph calibration. *Rev. Sci. Instrum.*, 81(6):063105, 2010.

[68] Andreas Quirrenbach, Pedro J. Amado, Walter Seifert, Miguel A. S??nchez Carrasco, Holger Mandel, Jose A. Caballero, Reinhard Mundt, Ignasi Ribas, Ansgar Reiners, Miguel Abril, Jesus Aceituno, Javier Alonso-Floriano, Matthias Ammler-von Eiff, Guillem Anglada-Escude, Regina Antona Jim??nez, Heiko Anwand-Heerwart, David Barrado y Navascu??s, Santiago Becerril, Victor Bejar, Daniel Benitez, Concepcion Cardenas, Antonio Claret, Josep Colome, Miriam Cort??s-Contreras, Stefan Czesla, Carlos del Burgo, Michaela Doellinger, R. Dorda, Stefan Dreizler, Carmen Feiz, Matilde Fernandez, David Galadi, Rafael Garrido, Jonay Gonz??lez Hern??ndez, Josep Guardia, Eike Guenther, Enrique de Guindos, Juan Guti??rrez-Soto, Hans J. Hagen, Artie Hatzes, Peter Hauschildt, Jens Helmling, Thomas Henning, Enrique Herrero, Armin Huber, Klaus Huber, Sandra Jeffers, Viki Joergens, Enrique de Juan, M. Kehr, Alexis Klutsch, Martin K??rster, S. Lalitha, Werner Laun, Ulrike Lemke, Rainer Lenzen, Jean-Louis Lizon, Mauro L??pez del Fresno, Mercedes L??pez-Morales, Javier L??pez-Santiago, Ulrich Mall, Eduardo Martin, Susana Mart??n-Ruiz, Eduard Mirabet, David Montes, Juan Carlos Morales, Rafael Morales Mu??oz, Andres Moya, Vianak Naranjo, Raquel Oreiro, David P??rez Medialdea, Michael Pluto, Ovidio Rabaza, Alejandro Ramon, Rafael Rebolo, Sabine Reffert, Petra Rhode, Hans-Walter Rix, Florian Rodler, Eloy Rodr??guez, Cristina Rodr??guez L??pez, Emilio Rodr??guez P??rez, A. Rodriguez Trinidad, Ralf-Reiner Rohloff, Ernesto S??nchez-Blanco, Jorge Sanz-Forcada, Sebastian Sch??fer, J??rg Schiller, Christof Schmidt, J??rgen Schmitt, Enrique Solano, Otmar Stahl, Clemens

Storz, Julian St??rmer, Juan Carlos Suarez, Ulrich Thiele, Rainer Ulbrich, Manuela Vidal-Dasilva, Karl Wagner, Johannes Winkler, Wenli Xu, Maria Rosa Zapatero Osorio, and Mathias Zechmeister. Carmenes. i: instrument and survey overview. volume 8446, pages 84460R–84460R–13, 2012.

[69] L. W. Ramsey, J. Barnes, S. L. Redman, H. R. A. Jones, A. Wolszczan, S. Bongiorno, L. Engel, and J. Jenkins. A Pathfinder instrument for precision radial velocities in the near-infrared. *Pub. Astr. Soc. Pacfic*, 120:887–894, aug 2008.

[70] Larry W. Ramsey, Suvrath Mahadevan, Stephen Redman, Chad Bender, Arpita Roy, Stephanie Zonak, Steinn Sigurdsson, and Alex Wolszczan. The Pathfinder testbed: exploring techniques for achieving precision radial velocities in the near infrared. *Proc. SPIE*, 7735:773571, 2010.

[71] Jinendra K. Ranka, Robert S. Windeler, and Andrew J. Stentz. Optical properties of high-delta air silica microstructure optical fibers. *Opt. Lett.*, 25(11):796–798, 2000.

[72] J.K. Ranka, R.S. Windeler, and A.J. Stentz. Efficient visible continuum generation in air-silica microstructure optical fibers with anomalous dispersion at 800 nm. In *Lasers and Electro-Optics, 1999. CLEO '99. Summaries of Papers Presented at the Conference on*, pages CPD8/1–CPD8/2, 1999.

[73] Stephen L Redman, Gabriel G Ycas, Ryan Terrien, Suvrath Mahadevan, Lawrence W Ramsey, Chad F Bender, Steven N Osterman, Scott A Diddams, Franklyn Quinlan, and James E Lawler. A high-resolution atlas of uranium-neon in the h band. *The Astrophysical Journal Supplement Series*, 199(1):2, 2012.

[74] Adam G. Riess, Alexei V. Filippenko, Peter Challis, Alejandro Clocchiatti, Alan Diercks, Peter M. Garnavich, Ron L. Gilliland, Craig J. Hogan, Saurabh Jha, Robert P. Kirshner, B. Leibundgut, M. M. Phillips, David Reiss, Brian P. Schmidt, Robert A. Schommer, R. Chris Smith, J. Spyromilio, Christopher Stubbs,

Nicholas B. Suntzeff, and John Tonry. Observational evidence from supernovae for an accelerating universe and a cosmological constant. *The Astronomical Journal*, 116(3):1009, 1998.

[75] Ralph A. Sawyer. Excitation processes in the hollow cathode discharge. *Phys. Rev.*, 36(1):44–50, July 1930.

[76] Albert Schliesser, Christoph Gohle, Thomas Udem, and Theodor W H??nsch. Complete characterization of a broadband high-finesse cavity using an optical frequency comb. *Opt. Express*, 14(13):5975–5983, 2006.

[77] D. A. Shaddock, M. B. Gray, and D. E. McClelland. Frequency locking a laser to an optical cavity by use of spatial mode interference. *Opt. Lett.*, 24(21):1499–1501, November 1999.

[78] Anthony Siegman. *Lasers*. University Science Books, Sausalito, CA, 1986.

[79] T. Sizer. Increase in laser repetition rate by spectral selection. *IEEE J. Quantum. Electron.*, 25:97–103, January 1989.

[80] Peter W Smith. Mode-locking of lasers. *Proceedings of the IEEE*, 58(9):1342–1357, 1970.

[81] Jeff Squier, Donald Harter, François Salin, and Gerard Mourou. 100-fs pulse generation and amplification in ti:al2o3. *Opt. Lett.*, 16(5):324–326, 1991.

[82] T. Steinmetz, T. Wilken, C. Araujo-Hauck, R. Holzwarth, T. Hänsch, and T. Udem. Fabry?-Pérot filter cavities for wide-spaced frequency combs with large spectral bandwidth. *Appl. Phys. B: Lasers Opt.*, 96(2):251–256, August 2009.

[83] Tilo Steinmetz, Tobias Wilken, Constanza Araujo-Hauck, Ronald Holzwarth, Theodor W. Hänsch, Luca Pasquini, Antonio Manescau, Sandro D'Odorico, Michael T. Murphy, Thomas Kentischer, Wolfgang

Schmidt, and Thomas Udem. Laser frequency combs for astronomical observations. *Science*, 321(5894):1335–1337, 2008.

[84] Y Sun, JL Zyskind, and AK Srivastava. Average inversion level, modeling, and physics of erbium-doped fiber amplifiers. *Selected Topics in Quantum Electronics, IEEE Journal of*, 3(4):991–1007, 1997.

[85] K Tamura, EP Ippen, HA Haus, and LE Nelson. 77-fs pulse generation from a stretched-pulse mode-locked all-fiber ring laser. *Optics letters*, 18(13):1080–1082, 1993.

[86] K. Tamura and M. Nakazawa. Pulse compression by nonlinear pulse evolution with reduced optical wave breaking in erbium-doped fiber amplifiers. *Opt. Lett.*, 21(1):68–70, January 1996.

[87] Florian Tauser, Alfred Leitenstorfer, and Wolfgang Zinth. Amplified femtosecond pulses from an er: fiber system: Nonlinear pulse shortening and selfreferencing detection of the carrier-envelope phase evolution. *Optics express*, 11(6):594–600, 2003.

[88] Michael J Thorpe, R Jason Jones, KD Moll, Jun Ye, and Ramin Lalezari. Precise measurements of optical cavity dispersion and mirror coating properties via femtosecond combs. *Opt. Express*, 13(3):882–888, 2005.

[89] Rick Trebino, Kenneth W DeLong, David N Fittinghoff, John N Sweetser, Marco A Krumbugel, Bruce A Richman, and Daniel J Kane. Measuring ultrashort laser pulses in the time-frequency domain using frequency-resolved optical gating. *Review of Scientific Instruments*, 68(9):3277–3295, 1997.

[90] Jeff A. Valenti, Debra Fischer, Geoffrey W. Marcy, John A. Johnson, Gregory W. Henry, Jason T. Wright, Andrew W. Howard, Matt Giguere, and Howard Isaacson. Two exoplanets discovered at keck observatory. *The Astrophysical Journal*, 702(2):989, 2009.

[91] Suzanne EA van Dijke. The role played by radial velocity in astronomy. *Leaflet of the Astronomical Society of the Pacific*, 4:322, 1944.

[92] Joseph Thomas Verdeyen. *Laser electronics*. Prentice Hall, Englewood Cliffs, NJ, 1989.

[93] JK Webb, JA King, MT Murphy, VV Flambaum, RF Carswell, and MB Bainbridge. Indications of a spatial variation of the fine structure constant. *Physical Review Letters*, 107(19):191101, 2011.

[94] John K. Webb, Victor V. Flambaum, Christopher W. Churchill, Michael J. Drinkwater, and John D. Barrow. Search for time variation of the fine structure constant. *Phys. Rev. Lett.*, 82(5):884–887, February 1999.

[95] Francois Wildi, Francesco Pepe, Bruno Chazelas, Gaspare Lo Curto, and Ch Lovis. A fabry-perot calibrator of the harps radial velocity spectrograph: performance report. In *Proc. SPIE*, volume 7735, page 77354X, 2010.

[96] Francois Wildi, Francesco Pepe, Bruno Chazelas, Gaspare Lo Curto, and Christophe Lovis. The performance of the new fabry-perot calibration system of the radial velocity spectrograph harps. volume 8151, pages 81511F–81511F–9, 2011.

[97] T. Wilken, T. W. Hansch, R. Holzwarth, P. Adel, and M. Mei. Low phase noise 250 mhz repetition rate fiber fs laser for frequency comb applications. In *Proc. Conf. Lasers and Electro-Optics*, page MR3. Optical Society of America, 2007.

[98] T. Wilken, C. Lovis, A. Manescau, T. Steinmetz, L. Pasquini, G. Lo Curto, T. W. Hänsch, R. Holzwarth, and Th. Udem. High-precision calibration of spectrographs. *Monthly Notices of the Royal Astronomical Society: Letters*, 405(1):L16–L20, 2010.

[99] Tobias Wilken, Gaspare Lo Curto, Rafael A Probst, Tilo Steinmetz, Antonio Manescau, Luca Pasquini, Jonay I González Hernández, Rafael Rebolo, Theodor W Hänsch, Thomas Udem, et al. A spectrograph for exoplanet observations calibrated at the centimetre-per-second level. *Nature*, 485(7400):611–614, 2012.

[100] Gabriel G. Ycas, Franklyn Quinlan, Scott A. Diddams, Steve Osterman, Suvrath Mahadevan, Stephen Redman, Ryan Terrien, Lawrence Ramsey, Chad F. Bender, Brandon Botzer, and Steinn Sigurdsson. Demonstration of on-sky calibration of astronomical spectra using a 25 ghz near-ir laser frequency comb. *Opt. Express*, 20(6):6631–6643, 2012.

APPENDIX A

FUSION SPLICE RECIPES

Solid-Core HNLF-SMF Splice

Parameter Group	Parameter	Value	Reference value for SMF-SMF Splice
Gapset			
	Cleaning Arc	150 ms	
	Gap	25 µm	
	Gap Position	R -30 µm [Towards HNLF]	
	Overlap	15 µm	
Prefuse			
	Power	20 bit	
	Time	180 ms	
	On	180 ms	
Arc 1			
	Power	5 bit	20 bit
	Time	30000 ms	2000 ms
Arc 2			
	Off		Off
Sweep			
	Direction	Auto	Off
	Power	8 bit	
	Time	21000 ms	
	Acceleration	40 %	
	Start	0 µm	
	Stop	550 µm	

Splicing Microstructured fiber to Single-mode Fiber

While splicing microstructured or photonic crystal fibers (PCFs) is possible, the unstable nature of the air-and-glass holey fibers makes it impossible to use many of the usual fusion splicing tricks. While a solid fiber with a small mode-field can usually be heated to adiabatically expand the size of the guided mode, significant heating of a PCF results in the collapse of the fiber and the destruction of the core all together, leaded to the coupling of the unguided light into cladding modes and out of the fiber. Here I will briefly summarize a successful splice of a 1060 nm PCF to a solid-core fiber, which was necessary after the PCF was broken after one of the ferrules fell from the optic table.

Because the PCF core size cannot be modified by heating, to achieve strong coupling between the PCF and another fiber it is extremely important to match both the mode-field diameter and also the numerical aperture. The 1060-NEG-1 PCF has a mode-field diameter of 2.2 μm and a NA of 0.37. A specialty high-numerical aperture fiber, such as those manufactured by Nufern, is required for a match. The matching fiber chosen is the Nufern "UHNA-3", which is single-mode from 960 – 1600 nm with a mode-field diameter of 2.6 μm at 1100 nm and a NA of 0.35. Not only is this fiber a very close match in terms of the guided mode parameters, but it is also designed to be easily spliced to a standard single-mode fiber by means of thermal core expansion.

Using this fiber and the following strategies a low (much less than 1 dB) loss splice was achieved between the UHNA and PCF fibers.

- Cleaning arc is disabled to prevent structure collapse of PCF.
- Gap is offset by 50 μm towards the solid fiber, again minimizing heating of the PCF.

- Alignment of fibers is done manually with photodiode and oscilloscope. After x-y coupling is maximized, fibers are gently rammed into one another along the z axis.
- Primary fusion arc is 15 bit for 200 ms (SMF values are 20 bit for 2000 ms)
- Re-Arcs at 15 bit, 200 ms are preformed until power shown on oscilloscope begins to decrease. These extra fusion arcs increase the strength of the splice.
- After the final re-arc, the automatic splice strength check performed by the fusion splicer ***must*** be prevented. This cannot be overridden, and the fiber must be quickly freed from the v-groove clamp before the strength check is conducted.